Discrete Mathematical Concepts in Micromagnetic Computations

Dissertation

zur Erlangung des Doktorgrades

des Fachbereichs Physik

der Universität Hamburg

vorgelegt von

Claas Willem Abert

aus Preetz

Hamburg

2013

Gutachter der Dissertation:	Prof. Dr. Michael Hinze
	PD Dr. Guido Meier
Gutachter der Disputation:	Prof. Dr. Michael Hinze
	PD Dr. Dieter Suess
Datum der Disputation:	3. September 2013
Vorsitzender des Prüfungsausschusses:	Prof. Dr. Hans-Peter Oepen
Vorsitzender des Promotionsausschusses:	Prof. Dr. Peter Hauschildt
Dekan der MIN Fakultät:	Prof. Dr. Heinrich Graener

Abstract

This work gives an overview over existing and novel numerical methods for the solution of the micromagnetic equations. A large part is dedicated to the computation of the demagnetization field. This subproblem accounts for the dipole–dipole interaction in magnetic materials. It is particularly interesting due to its nonlocal character, which results in a high computational complexity. A class of FFT-accelerated Fourier-space algorithms and a finite-element method with shell-transformation are described and compared to each other. Moreover, the numerical integration of the Landau-Lifshitz-Gilbert equation is investigated. The focus is put on a linear and implicit finite-element scheme. This scheme is extended such that it integrates not only the exchange field but also the demagnetization-field contribution implicitly. The open-source three-dimensional finite-element code magnum.fe is presented that implements the proposed methods. Finally, the domain-wall structure of tail-to-tail domain walls in nanorods is investigated with magnum.fe.

Zusammenfassung

Diese Arbeit gibt einen Überblick über existierende und neue numerische Methoden zur Lösung der mikromagnetischen Gleichungen. Ein großer Teil der Arbeit ist der Berechnung des Demagnetisierungsfeldes gewidmet. Dieses Teilproblem beschreibt die Dipol–Dipol Wechselwirkung in magnetischen Materialien. Durch den nichtlokalen Charakter hat das Demagnetisierungsproblem eine hohe algorithmische Komplexität. Ein Klasse von FFT-beschleunigten Fourierraum-Methoden und die Finite-Elemente-Methode mit Außenraumtransformation werden beschrieben und miteinander verglichen. Weiterhin wird die numerische Integration der Landau-Lifshitz-Gilbert Gleichung untersucht. Der Schwerpunkt liegt hierbei auf einem linearen, impliziten Verfahren. Dieses Verfahren wird derart erweitert, dass nicht nur das Austauschfeld, sondern auch der Demagnetisierungsfeld-Beitrag implizit integriert werden. Die quelloffene Finite-Elemente Software magnum.fe, die die eingeführten Methoden implementiert, wird vorgestellt. Abschließend wird die Domänenwandstruktur von tail-to-tail Domänenwänden in Nanostäbchen mit magnum.fe untersucht.

Contents

CHAPTER 1

Introduction

Magnetism plays an essential role in our day-to-day life not only through the earth's magnetic field that protects us from solar winds. A large number of technical applications exploit the properties of magnetic materials and fields. Famous applications include electrical generators and motors as well as magnetic hard-disk drives. In order to understand geomagnetic processes or to develop novel magnetic applications, a solid theoretical understanding of magnetism is required. Since magnetic ab-initio calculations are usually too involved for the description of macroscopic systems, various models have been established in order to approximately describe magnetism on different length scales. For the micron scale, the micromagnetic theory has proved to be a reliable model.

The micromagnetic theory was applied successfully to a great variety of problems such as the development of magnetic storage media. It is used to describe and improve classical hard-disk drives by optimization of the write head as well as the magnetic medium itself, see [1–3]. Moreover, the development of novel magnetic storage techniques like MRAM, see [4, 5], and the magnetic racetrack memory, see [6], benefit from the micromagnetic model. Beside its use in the development of storage media, the micromagnetic theory is also used for the investigation of hard magnetic materials, see [7]. More applications include the description of geophysical processes, see [8], or even the destruction of cancer cells, see [9].

The micromagnetic model describes magnetic processes in terms of a continuum theory governed by partial differential equations. Due to the lack of an analytical solution, many particular problems can only be solved approximately by discrete methods. Although not entirely new, this field of research is still very active. One reason is the rapid increase of computing power and memory in recent years. On the one hand this development allows the use of existing methods for a new class of more complex problems. On the other hand new classes of problems might also require new algorithms in order to be solved accurately. For example a faster processor allows the dynamical simulation of a longer time span, but the result is only meaningfull if the

time-integration scheme is stable over long times.

Another aspect is the rise of new hardware architectures. Due to the finite speed of electrical signals, the clock rate of modern processors hits the physical limits. Hence, in recent years not the clock rate but the number of parallel processing units is subject to increase. A highly parallel system architecture, however, calls for algorithms that perform well in parallel.

In this work an overview over existing discrete methods is given and novel methods are introduced. In Chapter 2 the theory of micromagnetism is introduced and motivated by first principle physics. Chapter 3 and 4 discuss discrete methods for the computation of the demagnetization field and the Landau-Lifshitz-Gilbert equation respectively. These chapters form the core of the work. The following Chapter 5 describes the finite-element micromagnetic code magnum.fe that was developed as part of this work. In Chapter 6 this code is used to perform actual computations on a realistic problem case. Chapter 7 concludes the work and gives an outlook to the ongoing work on this subject.

The mathematical notation throughout this work is written along the lines of physical publications. If not stated differently, all functions are assumed to be sufficiently smooth for the applied operations and all regions fulfill the requirements for the application of the integral theorems. Integrals and differential equations, if not defined on a certain region, are assumed to be defined on $\mathbb{R}^3$.

CHAPTER 2

Micromagnetism

Ferromagnetic materials from the viewpoint of theoretical physics are most accurately described by the theory of quantum mechanics. In this theory the ferromagnet is described by a N-body problem whose complexity grows exponentially with the number of involved bodies N [11]. Thus analytical calculations in this framework are restricted to very small systems.

Different models have been proposed in order to approximately describe ferromagnetic materials on a macroscopic scale. Depending on the simplifications introduced by a particular model it is able to describe the system accurately only under certain assumptions and on a certain length scale. Table 2.1 gives an overview of established models for the description of ferromagnets on different length scales.

For the description of ferromagnetism on the micron scale the theory of micromagnetism has proved to be a reliable tool. In contrast to domain theory it is able to resolve the inner structure of domain walls. On the other hand the micromagnetic equations can be solved numerically for relatively large system compared to atomistic approaches.

This chapter is organized as follows. In Sec. 2.1 the assumptions and simplifications of the micromagnetic model are discussed. Section 2.2 provides an overview over the different energy contributions of a ferromagnetic body. In Sec. 2.3 the Landau-Lifshitz-Gilbert equation is introduced, which describes the magnetization dynamics in micromagnetism. Section 2.4 and 2.5

Model	**Description**	**Length Scale**
Atomic level theory	Quantum mechanical ab initio calculations	$< 1\,\mathrm{nm}$
Micromagnetic theory	Continuous description of the magnetization	$1 - 1000\,\mathrm{nm}$
Domain theory	Description of domain structure	$1 - 1000\,\mu\mathrm{m}$
Phase theory	Description of ensembles of domains	$> 0.1\,\mathrm{mm}$

Table 2.1: Established models for the description of ferromagnetism on different length scales. The table is based on Fig. 1.5 in [10].

discuss extensions, limits and solutions of the micromagnetic equations.

2.1 Assumptions in Micromagnetism

Magnetic matter basically consists of magnetic dipoles called elementary magnets. These dipoles can be identified with spins and orbital angular momentum of charges on the atomic level. Macroscopic magnetic properties are consequently derived from the interaction and superposition of these dipoles.

In the special case of ferromagnetic materials, electrons with overlapping wave functions favor a parallel spin alignment due to the so-called exchange interaction, see Sec. 2.2.1. The alignment of elementary magnets $\boldsymbol{m}_i$ at places $\boldsymbol{r}_i$ can thus be assumed to be locally almost parallel

$$\boldsymbol{m}_i \approx \boldsymbol{m}_j \quad \text{for} \quad |\boldsymbol{r}_i - \boldsymbol{r}_j| < \lambda \tag{2.1.1}$$

where λ is a measure for the range of the exchange interaction, called the exchange length. Further a homogeneous density of elementary magnets is assumed. Taking into account these assumptions the discrete distribution of magnetic moments $\boldsymbol{m}_i$ can be well approximated by a continuous vector density $\boldsymbol{M}(\boldsymbol{r})$ such that

$$\int_\Omega \boldsymbol{M}(\boldsymbol{r})\,\mathrm{d}\boldsymbol{r} \approx \sum_i \mathbb{1}_\Omega(\boldsymbol{r}_i)\boldsymbol{m}_i \tag{2.1.2}$$

holds approximately for volumes Ω of the size λ^3 and bigger. It is important to understand that the existence and the range of the exchange interaction is crucial for a good approximation in Eqn. 2.1.2. The vector field $\boldsymbol{M}$ is called magnetization. Due to the homogeneous density of elementary magnets it has a constant norm

$$\boldsymbol{M}(\boldsymbol{r}) = M_\mathrm{s} \cdot \boldsymbol{m}(\boldsymbol{r}) \quad \text{with} \quad |\boldsymbol{m}(\boldsymbol{r})| = 1. \tag{2.1.3}$$

where M_s is called the saturation magnetization. In the following the unit vector field $\boldsymbol{m}$ which should not be confused with the moments $\boldsymbol{m}_i$ will often be used instead of $\boldsymbol{M}$.

The continuous magnetization field is a common parameter in classical electrodynamics [12]. Micromagnetism extends the classical field theory by non classical effects such as the exchange interaction. These effects are expressed in the framework of a continuum theory, see Sec. 2.2. Moreover, micromagnetism describes the dynamics of the magnetization field by the Landau-Lifshitz-Gilbert equation, see Sec. 2.3. Due to this combination of classical field theory and quantum mechanics, micromagnetism is often referred to as semi-classical continuum theory.

2.2 Energetics of a Ferromagnet

The total energy of a ferromagnet with respect to the magnetization is influenced by a multitude of physical effects. While some of these effects have a classical description, like the demagnetization energy and the Zeeman energy, others have a quantum mechanical origin and have to be adapted to the continuum theory of micromagnetism, e.g. the exchange energy and the anisotropy energy. By finding local minima of the energy functional, stable magnetization configurations can be obtained. However, the total energy does also play an important role for the dynamics of a ferromagnet as will be seen in Sec. 2.3.

2.2.1 Exchange Energy

The characteristic feature of ferromagnetic materials is the existence of spontaneous magnetization. From classical electrodynamics it is known that neighboring spins energetically favor an antiparallel alignment [12]. Consequently macroscopic magnetic bodies are expected to avoid a uniform magnetization, which in fact is the case for paramagnetic and diamagnetic materials.

However, the elementary magnets in ferromagnetic materials are subject to the so-called exchange interaction. This quantummechanical effect leads to an energetically favored parallel alignment of neighboring spins and thus to macroscopic uniform magnetization configurations.

The exchange energy is derived from the Coulomb energy of two indistinguishable particles with overlapping wave functions. A two-particle system of fermions features an antisymmetric overall wave function. For a singlet spin configuration this leads to a symmetric orbital wavefunction, whereas a triplet spin configuration leads to an antisymmetric orbital wave function. The expectation value of the two-particle distance is larger for antisymmetric orbital wave functions. Hence the triplet spin configuration leads to a lowered Coulomb energy and is thus energetically favored. In the classical picture the triplet configuration corresponds to a parallel alignment of spins. A detailed discussion of the exchange interaction can be found in any textbook on quantummechanics, e.g. [13].

Here we will use the classical Heisenberg Hamiltonian for two neighboring spins as starting point to derive a micromagnetic expression for the exchange energy

$$E_{i,j} = -J\, \boldsymbol{S}_i \cdot \boldsymbol{S}_j \tag{2.2.1}$$

where J is the so-called exchange integral and $\boldsymbol{S}_i$ and $\boldsymbol{S}_j$ are two neighboring classical spins. With the magnitude of the spins $S = |\boldsymbol{S}_i| = |\boldsymbol{S}_j|$ und the unit vectors $\boldsymbol{n}_i = \boldsymbol{S}_i/S$ and $\boldsymbol{n}_j = \boldsymbol{S}_j/S$

this can be written as

$$E_{i,j} = -J\,S^2\,\boldsymbol{n}_i \cdot \boldsymbol{n}_j \tag{2.2.2}$$

$$= -J\,S^2\,[1 - \frac{1}{2}(\boldsymbol{n}_i - \boldsymbol{n}_j)^2] \tag{2.2.3}$$

The exchange energy of a magnetic body is calculated by summing up

$$E = \sum_{i,j} -J_{ij}\,S^2\,[1 - \frac{1}{2}(\boldsymbol{n}_i - \boldsymbol{n}_j)^2] \tag{2.2.4}$$

where J_{ij} is the exchange integral for spins i and j. That means $J_{ij} \neq 0$ only for exchange coupled, usually neighboring, spins. In the theory of micromagnetism this expression has to be adapted to the continuous magnetization field $\boldsymbol{m}$. The scalar product in Eqn. 2.2.2 is analogously given by

$$\boldsymbol{m}(\boldsymbol{r}) \cdot \boldsymbol{m}(\boldsymbol{r} + \Delta\boldsymbol{r}) = 1 - \frac{1}{2}[\boldsymbol{m}(\boldsymbol{r}) - \boldsymbol{m}(\boldsymbol{r} + \Delta\boldsymbol{r})]^2 \tag{2.2.5}$$

where $\Delta\boldsymbol{r}$ is chosen as distance vector between two exchange coupled magnetic moments. Expanding $\boldsymbol{m}(\boldsymbol{r} + \Delta\boldsymbol{r})$ in $\Delta\boldsymbol{r}$ up to first order and inserting into Eqn. 2.2.5 yields

$$\boldsymbol{m}(\boldsymbol{r}) \cdot \boldsymbol{m}(\boldsymbol{r} + \Delta\boldsymbol{r}) \approx 1 - \frac{1}{2}\sum_i (\Delta\boldsymbol{r} \cdot \boldsymbol{\nabla} m_i)^2. \tag{2.2.6}$$

The energy for a magnetic body is obtained by summing up contributions from different distance vectors $\Delta\boldsymbol{r}_i$ depending on the crystal structure and integration over the magnetic body

$$E = \int_\Omega \sum_i A_i\,\boldsymbol{m}(\boldsymbol{r}) \cdot \boldsymbol{m}(\boldsymbol{r} + \Delta\boldsymbol{r}_i)\,\mathrm{d}\boldsymbol{r} \tag{2.2.7}$$

where A_i are called exchange constants and include the exchange integral and the magnitude of the spins involved. Inserting Eqn. 2.2.6 yields the general expression

$$E = C + \int_\Omega \sum_{i,j,k} A_{jk} \frac{\partial m_i}{\partial x_j} \frac{\partial m_i}{\partial x_k}\,\mathrm{d}\boldsymbol{r} \tag{2.2.8}$$

for the exchange energy. The constant C results from the integration of the constant term of Eqn. 2.2.6 and can be omitted without changing the physics of the system. Here A_{jk} is a matrix of exchange constants. By rotation of the coordinate system this matrix can be diagonalized [14] which yields

$$E = \int_\Omega \sum_{i,j} A_j \left(\frac{\partial m_i}{\partial x_j}\right)^2 \mathrm{d}\boldsymbol{r}. \tag{2.2.9}$$

In the case of cubic and isotropic materials the exchange constant does not depend on the spatial dimension und thus Eqn. 2.2.9 further reduces to

$$E = A \int_\Omega \sum_i (\boldsymbol{\nabla} m_i)^2\,\mathrm{d}\boldsymbol{r} = A \int_\Omega (\boldsymbol{\nabla}\boldsymbol{m})^2\,\mathrm{d}\boldsymbol{r}. \tag{2.2.10}$$

This expression turns out to accurately describe most materials and is usually used in micromagnetics. The exchange constant A is determined experimentally.

Note that this result was derived from the classical Heisenberg model that assumes localized spins. In metallic ferromagnets the spins are not localized and the Heisenberg model does not apply. However, Eqn. 2.2.10 still describes the exchange interaction phenomenologically up to first order [10].

2.2.2 Demagnetization Energy

The demagnetization energy, also called magnetostatic energy or stray-field energy, is the energy of the magnetization in the magnetic field created by the magnetization itself. This means that this energy contribution accounts for the dipole–dipole interaction of the elementary magnets.

The demagnetization energy can be derived from classical electromagnetics. Maxwell's equations for electrostatics, assuming a vanishing current $\boldsymbol{J}$, are given by

$$\nabla \cdot \boldsymbol{B} = 0 \tag{2.2.11}$$

$$\nabla \times \boldsymbol{H} = 0 \tag{2.2.12}$$

where the magnetic flux $\boldsymbol{B}$ is connected to the magnetic field $\boldsymbol{H}$ via the magnetization $\boldsymbol{M}$

$$\boldsymbol{B} = \mu_0(\boldsymbol{H} + \boldsymbol{M}). \tag{2.2.13}$$

Equation 2.2.12 is equivalent to the magnetic field $\boldsymbol{H}$ being the gradient of a scalar potential u. Hence the demagnetization-field is the solution to the system

$$\Delta u = \nabla \cdot \boldsymbol{M} \tag{2.2.14}$$

$$\boldsymbol{H} = -\nabla u. \tag{2.2.15}$$

The boundary condition to this system is given in an asymptotical fashion by

$$u(\boldsymbol{r}) = \mathcal{O}(1/|\boldsymbol{r}|) \text{ for } |\boldsymbol{r}| \to \infty. \tag{2.2.16}$$

This condition states that the potential drops to zero at infinity. It is often referred to as open boundary condition. Equation 2.2.14 is Poisson's equation and can be solved with the well known Green's function of the Laplacian, which naturally satisfies the boundary condition 2.2.16, see [12]

$$u(\boldsymbol{r}) = -\frac{1}{4\pi} \int \frac{\nabla' \cdot \boldsymbol{M}(\boldsymbol{r}')}{|\boldsymbol{r} - \boldsymbol{r}'|} \, \mathrm{d}\boldsymbol{r}' \tag{2.2.17}$$

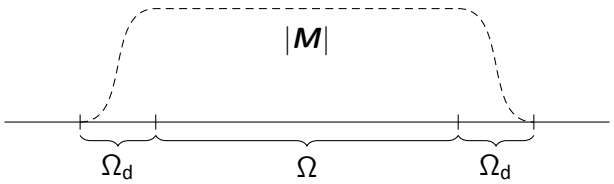

Figure 2.1: Sketch of the limiting procedure used for the derivation of the boundary term in the integral solution of the scalar potential. The discontinuity of the magnetization across the sample boundary $\partial\Omega$ is smoothed out in a region Ω_d surrounding the sample.

where the integration is carried out over the whole space. In the case of an ideal magnetic body the magnetization is only defined on a finite region Ω

$$|\boldsymbol{M}(\boldsymbol{r})| = \begin{cases} M_\mathrm{s} & \text{if } \boldsymbol{r} \in \Omega \\ 0 & \text{else} \end{cases} \tag{2.2.18}$$

which leads to a discontinuity of $\boldsymbol{M}$ on the boundary $\partial\Omega$. In this case the solution of Eqn. 2.2.17 can be obtained by a limiting process. Consider a finite region Ω_d that surrounds the magnetic body Ω. Further we assume a smooth decay of the magnetization within Ω_d, see Fig. 2.1. With the magnetization and its divergence vanishing in the outside region $\mathbb{R}^3\backslash\Omega \cup \Omega_\mathrm{d}$ Eqn. 2.2.17 can be written as

$$u(\boldsymbol{r}) = -\frac{1}{4\pi}\left[\int_\Omega \frac{\boldsymbol{\nabla}'\cdot\boldsymbol{M}(\boldsymbol{r}')}{|\boldsymbol{r}-\boldsymbol{r}'|}\,\mathrm{d}\boldsymbol{r}' + \int_{\Omega_\mathrm{d}} \frac{\boldsymbol{\nabla}'\cdot\boldsymbol{M}(\boldsymbol{r}')}{|\boldsymbol{r}-\boldsymbol{r}'|}\,\mathrm{d}\boldsymbol{r}'\right]. \tag{2.2.19}$$

Applying Green's theorem to the integral over Ω_d yields

$$\int_{\Omega_\mathrm{d}} \frac{\boldsymbol{\nabla}'\cdot\boldsymbol{M}(\boldsymbol{r}')}{|\boldsymbol{r}-\boldsymbol{r}'|}\,\mathrm{d}\boldsymbol{r}' = \int_{\partial\Omega_\mathrm{d}} \frac{\boldsymbol{M}(\boldsymbol{r}')\cdot\boldsymbol{n}}{|\boldsymbol{r}-\boldsymbol{r}'|}\,\mathrm{d}\boldsymbol{s}' - \int_{\Omega_\mathrm{d}} \boldsymbol{M}(\boldsymbol{r}')\cdot\boldsymbol{\nabla}'\frac{1}{|\boldsymbol{r}-\boldsymbol{r}'|}\,\mathrm{d}\boldsymbol{r}' \tag{2.2.20}$$

where $\mathrm{d}\boldsymbol{s}'$ is the area measure to $\boldsymbol{r}'$ and $\boldsymbol{n}$ is the unit outward normal. In the limit of a rapidly decaying magnetization $\boldsymbol{M}$ the region Ω_d can become infinitely small without changing the result of Eqn. 2.2.20. In this case the right-hand side of Eqn. 2.2.20 reduces to the boundary integral since the volume integral has a finite integrand and is carried out over an infinitely small volume. The boundary $\partial\Omega_\mathrm{d}$ consists of an inner and an outer boundary. The integral over the outer boundary vanishes, because of a vanishing magnetization $\boldsymbol{M}$. The inner boundary coincides with the boundary of the magnetic body $\partial\Omega$ except for the orientation. Thus the boundary integral can be replaced by an integral over $\partial\Omega$ with opposite sign. Inserting into Eqn. 2.2.19 results in

$$u(\boldsymbol{r}) = -\frac{1}{4\pi}\left[\int_\Omega \frac{\boldsymbol{\nabla}'\cdot\boldsymbol{M}(\boldsymbol{r}')}{|\boldsymbol{r}-\boldsymbol{r}'|}\,\mathrm{d}\boldsymbol{r}' - \int_{\partial\Omega} \frac{\boldsymbol{M}(\boldsymbol{r}')\cdot\boldsymbol{n}}{|\boldsymbol{r}-\boldsymbol{r}'|}\,\mathrm{d}\boldsymbol{s}'\right]. \tag{2.2.21}$$

The expressions $\rho = -\boldsymbol{\nabla}\boldsymbol{M}$ and $\sigma = \boldsymbol{M}\cdot\boldsymbol{n}$ are often referred to as magnetic volume charges and magnetic surfaces charges respectivly. An alternative expression to Eqn. 2.2.21 can be

obtained by applying Green's theorem

$$u(\boldsymbol{r}) = \frac{1}{4\pi} \int_\Omega \boldsymbol{M}(\boldsymbol{r}') \cdot \boldsymbol{\nabla}' \frac{1}{|\boldsymbol{r} - \boldsymbol{r}'|} \, \mathrm{d}\boldsymbol{r}'. \tag{2.2.22}$$

The demagnetization field $\boldsymbol{H}_{\text{demag}}$ is calculated as negative gradient of the potential u with respect to $\boldsymbol{r}$

$$\boldsymbol{H}_{\text{demag}}(\boldsymbol{r}) = -\boldsymbol{\nabla} u(\boldsymbol{r}) = \int_\Omega \widetilde{\boldsymbol{N}}(\boldsymbol{r} - \boldsymbol{r}') \boldsymbol{M}(\boldsymbol{r}') \, \mathrm{d}\boldsymbol{r}' \tag{2.2.23}$$

with the so-called demagnetization tensor $\widetilde{\boldsymbol{N}}$ given by

$$\widetilde{\boldsymbol{N}}(\boldsymbol{r} - \boldsymbol{r}') = -\frac{1}{4\pi} \boldsymbol{\nabla} \boldsymbol{\nabla}' \frac{1}{|\boldsymbol{r} - \boldsymbol{r}'|}. \tag{2.2.24}$$

According to classical electrodynamics the energy is given by

$$E = -\frac{\mu_0}{2} \int_\Omega \boldsymbol{M} \cdot \boldsymbol{H}_{\text{demag}} \, \mathrm{d}\boldsymbol{r} \tag{2.2.25}$$

$$= -\frac{\mu_0}{2} \iint_\Omega \boldsymbol{M}(\boldsymbol{r}) \widetilde{\boldsymbol{N}}(\boldsymbol{r} - \boldsymbol{r}') \boldsymbol{M}(\boldsymbol{r}') \, \mathrm{d}\boldsymbol{r} \, \mathrm{d}\boldsymbol{r}' \tag{2.2.26}$$

where the factor $1/2$ accounts for the fact that the field is generated by the magnetization itself. Due to the integration over $\boldsymbol{r}$ and $\boldsymbol{r}'$ every dipole–dipole interaction between $\boldsymbol{M}(\boldsymbol{r})$ and $\boldsymbol{M}(\boldsymbol{r}')$ contributes twice to the result, which is corrected by this prefactor.

2.2.3 Anisotropy Energy

Depending on the crystal structure of a ferromagnetic material, it energetically favors the alignment of the magnetization parallel to certain axes. This energy contribution results from spin-orbit interactions [10] and is referred to as anisotropy energy. The energetically favored axes are called easy axes. These axes are undirected which means that a local minimum of the energy at $\boldsymbol{m}_{\text{min}}$ implies a local minimum at $-\boldsymbol{m}_{\text{min}}$ with

$$E(\boldsymbol{m}_{\text{min}}) = E(-\boldsymbol{m}_{\text{min}}) \tag{2.2.27}$$

Depending on the lattice structure, a material may have one or more of these easy axes. In the simplest case a material has a single easy axis. This uniaxial anisotropy energy is given by

$$E = -\int_\Omega [K_{\text{u1}} (\boldsymbol{m} \cdot \boldsymbol{e}_{\text{u}})^2 + K_{\text{u2}} (\boldsymbol{m} \cdot \boldsymbol{e}_{\text{u}})^4] \, \mathrm{d}\boldsymbol{r} \tag{2.2.28}$$

where $\boldsymbol{e}_{\text{u}}$ is a unit vector pointing in the direction of the easy axis and K_{u1} and K_{u2} are called anisotropy constants. This phenomenological expression is the result of a Taylor expansion up to fourth order. Only even powers are considered in order to fullfill the symmetry condition 2.2.27. Uniaxial anisotropy occurs in materials with a hexagonal or tetragonal crystal structure, e.g. cobalt.

Materials with a cube-symmetric lattice structure naturally feature three easy axes $\boldsymbol{e}_i$ which are pairwise orthogonal

$$\boldsymbol{e}_i \cdot \boldsymbol{e}_j = \delta_{ij}. \tag{2.2.29}$$

The energy of such a cubic anisotropy is the result of an expansion in the magnetization components along the easy axes

$$E = \int_\Omega [K_{c1}(m_1^2 m_2^2 + m_2^2 m_3^2 + m_3^2 m_1^2) + K_{c2} m_1^2 m_2^2 m_3^2] \, \mathrm{d}\boldsymbol{r} \tag{2.2.30}$$

where $m_i = \boldsymbol{e}_i \cdot \boldsymbol{m}$ is the magnetization component in direction of the anisotropy axis $\boldsymbol{e}_i$. Again terms which violate the symmetry condition 2.2.27 are neglected. Moreover, only contributions which are constant under permutation of magnetization components m_i are considered in order to comply with the cubic symmetry. Cubic anisotropy occurs in materials such as iron which has a body-centered cubic structure or nickel which has a face-centered cubic structure.

Although the expressions for the anisotropy energy in Eqn. 2.2.28 and 2.2.30 have a pure phenomenological origin, they are able to describe anisotropy effects with a high accuracy. In practical applications the energy expressions are often reduced to the lowest order term.

2.2.4 Zeeman Energy

The Zeeman energy of a ferromagnetic body is the energy of the magnetization in an external field $\boldsymbol{H}_{\text{zeeman}}$ given by

$$E = -\mu_0 \int_\Omega \boldsymbol{M} \cdot \boldsymbol{H}_{\text{zeeman}} \, \mathrm{d}\boldsymbol{r}. \tag{2.2.31}$$

2.3 Landau-Lifshitz-Gilbert Equation

The central equation in micromagnetism for the description of magnetization dynamics is the Landau-Lifshitz-Gilbert equation, which was originally proposed in [15]. In this work from 1935 by Landau and Lifshitz the motion of the magnetization is described by a precessional term and a damping term. While the precessional term is physically derived in this work, the damping term is purely phenomenological. In 1955 Gilbert derived an equivalent expression for the Landau-Lifshitz-Gilbert equation from a Lagrangian formulation, where the damping is treated more strictly, see [16] and [17].

In the following a classical Lagrangian method as well as a quantum mechanical approach are presented briefly to derive the Landau-Lifshitz-Gilbert equation. Both approaches give insight to different aspects of the micromagnetic model and are thus of interest for the application of this theory.

2.3.1 Lagrange Approach

With an appropriate Lagrange functional the Landau-Lifshitz-Gilbert equation can be obtained by the Lagrangian formalism. Since the magnetization $\boldsymbol{M}$ is assumed to be normalized, see Eqn. 2.1.3, its motion may locally be well described by the rotation of a rigid body. The angular velocity of a rigid body in terms of the Euler angles reads

$$\boldsymbol{\Omega} = \begin{pmatrix} \dot{\phi}\sin(\theta)\sin(\psi) + \dot{\theta}\cos(\psi) \\ \dot{\phi}\sin(\theta)\cos(\psi) + \dot{\theta}\sin(\psi) \\ \dot{\phi}\cos(\theta) + \dot{\psi} \end{pmatrix} \tag{2.3.1}$$

where the shorthand notation $\dot{f} = \partial_t f$ is used. Note that the angular velocity $\boldsymbol{\Omega}$ as well as the angles θ, ϕ and ψ have to depend on the location $\boldsymbol{r}$ in order to describe the magnetization field $\boldsymbol{m}(\boldsymbol{r})$. Without loss of generality the rotation axes can be chosen such that the r_3-axis points into the direction of the magnetization in every point and thus

$$\boldsymbol{m} = \begin{pmatrix} 0 \\ 0 \\ 1 \end{pmatrix}. \tag{2.3.2}$$

In the rigid-body picture the magnetization is described by a rotationally symmetric stick. Since the angle ψ describes the rotation of the stick around its symmetry axis it may be set to $\psi = 0$ without loss of generality [18]. Thus Eqn. 2.3.1 reduces to

$$\boldsymbol{\Omega} = \begin{pmatrix} \dot{\theta} \\ \dot{\phi}\sin(\theta) \\ \dot{\phi}\cos(\theta) + \dot{\psi} \end{pmatrix}. \tag{2.3.3}$$

The Lagrangian of a dynamical system in general is given by

$$\mathcal{L} = T(\boldsymbol{q}, \dot{\boldsymbol{q}}) - V(\boldsymbol{q}) \tag{2.3.4}$$

where T is the kinetic energy and V is the potential energy of the system and $\boldsymbol{q}$ and $\dot{\boldsymbol{q}}$ are the generalized coordinates and their time derivatives respectively. In micromagnetics the potential energy is given by the energy contributions discussed in Sec. 2.2. The kinetic energy however has no classical explanation since the magnetization does not have inertia in the classical sense. In [16] Gilbert proposed the Lagrangian

$$\mathcal{L} = -\frac{M_s}{\gamma}\dot{\phi}\cos(\theta) - U(\theta, \phi). \tag{2.3.5}$$

As shown by Wegrowe et al. in [19] this expression is equivalent to

$$\mathcal{L} = \frac{1}{2}I[\dot{\phi}\cos(\theta) + \dot{\psi}]^2 - U(\theta, \phi) \tag{2.3.6}$$

$$= \frac{1}{2}I\Omega_3^2 - U(\theta, \phi) \tag{2.3.7}$$

which describes a classical rotation energy with I being the moment of inertia. However, in this energy only the rotation around the symmetry axis of the magnetization is considered. From a classical point of view it is not clear why Ω_1 and Ω_2 may be neglected. In [19] this choice of $\mathcal{L}$ is discussed in detail.

In the following we will stick with the Lagrangian 2.3.5 as proposed by Gilbert. According to the Lagrangian formulation, the equation of motion in terms of the generalized coordinates $\boldsymbol{q} = (\theta, \phi)$ is given by

$$\frac{\mathrm{d}}{\mathrm{d}t}\frac{\delta \mathcal{L}}{\delta \dot{q_i}} - \frac{\delta \mathcal{L}}{\delta q_i} + \frac{\delta D}{\delta \dot{q_i}} = 0 \tag{2.3.8}$$

where $\delta/\delta f$ denotes a functional derivative and D is an additional dissipative Rayleigh function that accounts for energy losses of the system. Inserting Eqn. 2.3.5 into Eqn. 2.3.8 yields

$$\dot{\phi}\sin(\theta) = \frac{\gamma}{M_\mathrm{s}}\left[\frac{\delta U}{\delta \theta} + \frac{\delta D}{\delta \dot{\theta}}\right] \tag{2.3.9}$$

$$\dot{\theta} = -\frac{\gamma}{M_\mathrm{s}\sin(\theta)}\left[\frac{\delta U}{\delta \phi} + \frac{\delta D}{\delta \dot{\phi}}\right]. \tag{2.3.10}$$

These equations of motion describe the dynamics of the magnetization by the Euler angles $\phi(\boldsymbol{r})$ and $\theta(\boldsymbol{r})$. In order to obtain a description in cartesian coordinates, the time derivative of the magnetization in cartesian coordinates is considered

$$\partial_t \boldsymbol{m} = \boldsymbol{\Omega} \times \boldsymbol{m} = \begin{pmatrix} \dot{\phi}\sin(\theta) \\ -\dot{\theta} \\ 0 \end{pmatrix}. \tag{2.3.11}$$

Furthermore, since the magnetization is a unit vector field $|\boldsymbol{m}| = 1$, variations of the Euler angles ϕ and θ are given by

$$\delta m_1 = \sin(\theta)\delta\phi \tag{2.3.12}$$

$$\delta m_2 = \delta\theta. \tag{2.3.13}$$

Hence Eqn. 2.3.9 and 2.3.10 can be written as

$$\partial_t m_1 = \frac{\gamma}{M_\mathrm{s}}\left[\frac{\delta U}{\delta m_2} + \frac{\delta D}{\delta \dot{m_2}}\right] \tag{2.3.14}$$

$$\partial_t m_2 = -\frac{\gamma}{M_\mathrm{s}}\left[\frac{\delta U}{\delta m_1} + \frac{\delta D}{\delta \dot{m_1}}\right] \tag{2.3.15}$$

or equivalently

$$\partial_t \boldsymbol{m} = -\frac{\gamma}{M_\mathrm{s}}\boldsymbol{m} \times \left(\frac{\delta U}{\delta \boldsymbol{m}} + \frac{\delta D}{\delta \dot{\boldsymbol{m}}}\right). \tag{2.3.16}$$

Choosing the reasonable dissipative function $D = \alpha^*(\partial_t \boldsymbol{m})^2$ with $\alpha^* \geq 0$ results in the Landau-Lifshitz-Gilbert equation

$$\partial_t \boldsymbol{m} = -\gamma(\boldsymbol{m} \times \boldsymbol{H}_\mathrm{eff}) + \alpha(\boldsymbol{m} \times \partial_t \boldsymbol{m}) \tag{2.3.17}$$

where $\boldsymbol{H}_{\text{eff}}$ is the so-called effective field given by

$$\boldsymbol{H}_{\text{eff}} = -\frac{1}{\mu_0 M_s}\frac{\delta U}{\delta \boldsymbol{m}}. \tag{2.3.18}$$

and $\alpha \geq 0$ is a damping constant.

2.3.2 Quantum Mechanical Approach

In Sec. 2.3.1 it is shown that the Landau-Lifshitz-Gilbert equation can be obtained by application of the classical Lagrange formalism. However, this method is based on a particular choice of the Lagrangian, which is not completely justifiable by classical theory.

In this section a quantum mechanical approach is discussed to derive the Landau-Lifshitz-Gilbert equation. As described in Sec. 2.1 the continuous magnetization field approximates a discrete distribution of spins. In quantum mechanics the components of the spin are described by the spin operators $\widehat{S}_i$. In the Heisenberg picture the time development of the spin operators are given by

$$\frac{\mathrm{d}\widehat{S}_j}{\mathrm{d}t} = \frac{1}{i\hbar}\left[\widehat{S}_j, \widehat{H}\right]. \tag{2.3.19}$$

The contributions to the Hamiltonian in the context of micromagnetics will depend on the spin. Thus it is reasonable to expand the Hamiltonian in the spin operators

$$\begin{aligned}\left[\widehat{S}_j, \widehat{H}\right] &= \sum_k \frac{\partial \widehat{H}}{\partial \widehat{S}_k}\left[\widehat{S}_k, \widehat{S}_j\right] + \mathcal{O}(\hbar^2) \\ &= i\hbar \sum_{k,l} \frac{\partial \widehat{H}}{\partial \widehat{S}_k}\epsilon_{jkl}\widehat{S}_l + \mathcal{O}(\hbar^2).\end{aligned} \tag{2.3.20}$$

Inserting into Eqn. 2.3.19 and using the vector notation $\widehat{\boldsymbol{S}} = (\widehat{S}_1, \widehat{S}_2, \widehat{S}_3)$ yields

$$\frac{\mathrm{d}\widehat{\boldsymbol{S}}}{\mathrm{d}t} = -\widehat{\boldsymbol{S}} \times \frac{\partial \widehat{H}}{\partial \widehat{\boldsymbol{S}}} + \mathcal{O}(\hbar). \tag{2.3.21}$$

In the classical limit the spin operators may be replaced by the continuous magnetization vector $\boldsymbol{M} = M_s \boldsymbol{m}$. Further the second term can be neglected since $\hbar \to 0$. Identifying $\partial \widehat{H}/\partial \widehat{\boldsymbol{S}}$ with the effective field $\boldsymbol{H}_{\text{eff}}$ in Eqn. 2.3.18 leads to

$$\partial_t \boldsymbol{m} = -\gamma'(\boldsymbol{m} \times \boldsymbol{H}_{\text{eff}}). \tag{2.3.22}$$

This equation describes the precession of the magnetization around the effective field without any loss of energy. According to the original work of Landau and Lifshitz [15] a phenomenological damping term is added in order to account for these losses. This damping term is constructed such that it is perpendicular to the precessional term. Further it should conserve the magnetization norm leading to

$$\partial_t \boldsymbol{m} = -\gamma'(\boldsymbol{m} \times \boldsymbol{H}_{\text{eff}}) - \alpha' \boldsymbol{m} \times (\boldsymbol{m} \times \boldsymbol{H}_{\text{eff}}). \tag{2.3.23}$$

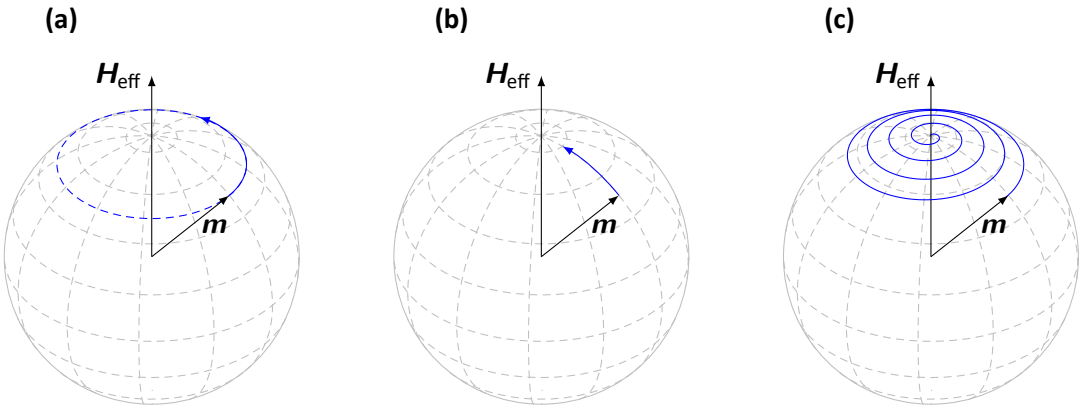

Figure 2.2: Time evolution of a single magnetic moment as described by the Landau-Lifshitz-Gilbert equation. The motion can be divided into a precessional and a damping part. **(a)** Precessional motion around the effective field. **(b)** Damped motion. The magnetization relaxes towards the effective field. **(c)** Resulting motion including precession and damping.

This is the explicit form of the Landau-Lifshitz-Gilbert equation. It can be shown that this form is equivalent to the implicit form in Eqn. 2.3.17. This is done by inserting Eqn. 2.3.17 for $\partial_t \boldsymbol{m}$ on the right-hand side of Eqn. 2.3.17 and using the vector identity $\boldsymbol{a} \times (\boldsymbol{b} \times \boldsymbol{c}) = (\boldsymbol{a} \cdot \boldsymbol{c})\boldsymbol{b} - (\boldsymbol{a} \cdot \boldsymbol{b})\boldsymbol{c}$. The coefficients of the different versions of the Landau-Lifshitz-Gilbert equation satisfy the relations

$$\gamma' = \gamma/(1+\alpha^2) \tag{2.3.24}$$

$$\alpha' = \alpha\gamma/(1+\alpha^2). \tag{2.3.25}$$

A full quantum mechanical description of a spin subject to exchange interaction, anisotropy and Zeeman field is given in [20] where the Landau-Lifshitz-Gilbert equation is also obtained in a limit case.

2.3.3 Effective Field

The Landau-Lifshitz-Gilbert equation describes the motion of the magnetization in an effective field defined by Eqn. 2.3.18. This motion can be described as the sum of a precessional term and a damping term. Figure 2.2 illustrates these two terms for the explicit formulation of the Landau-Lifshitz-Gilbert equation 2.3.23.

In the case of the Zeeman energy and the demagnetization energy, the effective field is an actual field in the classical sense. The Zeeman field is directly given by $\boldsymbol{H}_{\text{zeeman}}$, the demagnetization field is computed via Eqn. 2.2.23.

However, the exchange field as well as the anisotropy field have to be calculated via the vari-

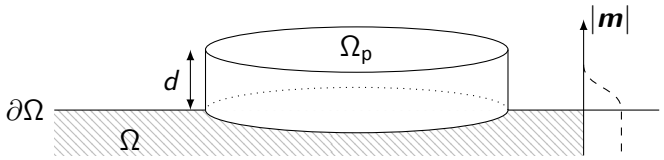

Figure 2.3: A so-called Gaussian pillbox Ω_p on the outer boundary of the sample Ω. The discontinuity of the magnetization $\boldsymbol{m}$ across the sample boundary $\partial\Omega$ is smoothed out within the pillbox, as sketched on the right-hand side. Properties of the discontinuous system are obtained by considering the limit $d \to 0$.

ational derivative in Eqn. 2.3.18. The exchange energy density is given by the integrand of Eqn. 2.2.10. Applying the chain rule of variational calculus yields

$$\boldsymbol{H}_\mathrm{ex}(\boldsymbol{r}) = -\frac{A}{\mu_0 M_\mathrm{s}} \frac{\delta}{\delta \boldsymbol{m}} (\boldsymbol{\nabla m})^2 \tag{2.3.26}$$

$$= \frac{2A}{\mu_0 M_\mathrm{s}} \Delta \boldsymbol{m} \tag{2.3.27}$$

Analogously the effective fields for uniaxial and cubic anisotropy are obtained by computing the variational derivative of Eqn. 2.2.28 and 2.2.30 respectively

$$\boldsymbol{H}_\mathrm{u}(\boldsymbol{r}) = \frac{2K_\mathrm{u1}}{\mu_0 M_\mathrm{s}} \boldsymbol{e}_\mathrm{u}(\boldsymbol{e}_\mathrm{u} \cdot \boldsymbol{m}) + \frac{4K_\mathrm{u2}}{\mu_0 M_\mathrm{s}} \boldsymbol{e}_\mathrm{u}(\boldsymbol{e}_\mathrm{u} \cdot \boldsymbol{m})^3 \tag{2.3.28}$$

$$\boldsymbol{H}_\mathrm{c}(\boldsymbol{r}) = -\frac{2K_\mathrm{c1}}{\mu_0 M_\mathrm{s}} \begin{pmatrix} m_1 m_2^2 + m_1 m_3^2 \\ m_2 m_3^2 + m_2 m_1^2 \\ m_3 m_1^2 + m_3 m_2^2 \end{pmatrix} - \frac{2K_\mathrm{c2}}{\mu_0 M_\mathrm{s}} \begin{pmatrix} m_1 m_2^2 m_3^2 \\ m_1^2 m_2 m_3^2 \\ m_1^2 m_2^2 m_3 \end{pmatrix}. \tag{2.3.29}$$

2.3.4 Boundary Conditions

Due to the first derivate in time the Landau-Lifshitz-Gilbert equation is an initial value problem. In order to find a solution $\boldsymbol{m}(\boldsymbol{r}, t)$ for $t > t_0$ the initial magnetization $\boldsymbol{m}(\boldsymbol{r}, t_0)$ has to be known.

Depending on the effective field, additional boundary conditions are required in order to find a unique solution of the Landau-Lifshitz-Gilbert equation. In fact, even with given boundary conditions the uniqueness of solutions to the Landau-Lifshitz-Gilbert equation could only be shown for special cases, see [21–23]. From the effective field contribution discussed in Sec. 2.3.3, the exchange field is the only one that adds the need of boundary conditions due to its second order in space.

If this so-called exchange boundary condition is applied on the boundary of an ideal magnetic body, i.e. a boundary where the magnetization rapidly drops to zero, it is uniquely defined. Consider the Landau-Lifshitz-Gilbert equation without damping and with the exchange field as effective field.

$$\partial_t \boldsymbol{m} = -\gamma \boldsymbol{m} \times \Delta \boldsymbol{m}. \tag{2.3.30}$$

Since at the boundary of an ideal magnetic body the Laplacian of the magnetization $\Delta \boldsymbol{m}$ is not defined, a limiting procedure is used to obtain the boundary condition. Like in Sec. 2.2.2 the magnetization is considered to decay continuously in a finite interval d. Equation 2.3.30 is integrated over a so-called Gaussian pillbox as sketched in Fig. 2.3. Application of Green's theorem yields

$$\int_{\Omega_\mathrm{p}} \partial_t m_i \,\mathrm{d}\boldsymbol{r} = \int_{\Omega_\mathrm{p}} \epsilon_{ijk} m_j \Delta m_k \,\mathrm{d}\boldsymbol{r} \tag{2.3.31}$$

$$= \int_{\partial\Omega_\mathrm{p}} \epsilon_{ijk} m_j \frac{\partial m_k}{\partial \boldsymbol{n}} \,\mathrm{d}\boldsymbol{r} - \int_{\Omega_\mathrm{p}} \epsilon_{ijk} \boldsymbol{\nabla} m_j \cdot \boldsymbol{\nabla} m_k \,\mathrm{d}\boldsymbol{r}. \tag{2.3.32}$$

The second integral on the right-hand side of Eqn. 2.3.32 vanishes due to the skew-symmetric Levi-Civita tensor ϵ. The boundary of the pillbox $\partial\Omega_\mathrm{p}$ coincides with the boundary of the magnetic body Ω on one side except for the orientation. The other side of the pillbox is outside the magnetic body where $|\boldsymbol{m}| = 0$. Hence Eqn. 2.3.32 reads

$$\int_{\Omega_\mathrm{p}} \partial_t m \,\mathrm{d}\boldsymbol{r} = -\int_{\partial\Omega} \boldsymbol{m} \times \frac{\partial \boldsymbol{m}}{\partial \boldsymbol{n}} \,\mathrm{d}\boldsymbol{r} \tag{2.3.33}$$

In the limit $d \to 0$ the volume integral on the left-hand-side of Eqn. 2.3.31 vanishes. Since the faces of the pill box can be chosen arbitrarily the boundary condition

$$\boldsymbol{m} \times \frac{\partial \boldsymbol{m}}{\partial \boldsymbol{n}} = 0 \tag{2.3.34}$$

must hold in every boundary point. Further since $|\boldsymbol{m}| = 1$ the normal derivative of the magnetization is perpendicular to the magnetization in every point $\partial\boldsymbol{m}/\partial\boldsymbol{n} \perp \boldsymbol{m}$ and thus

$$\frac{\partial \boldsymbol{m}}{\partial \boldsymbol{n}} = 0. \tag{2.3.35}$$

This is the so-called exchange boundary condition, which is the right choice if the boundary of the computational domain Ω coincides with the boundary of an ideal magnet as shown above. Equation 2.3.35 was originally derived by Rado and Weertman in [24]. Before, it was shown by Brown that the same boundary condition has to hold in energetic equilibrium [25]. Depending on further contributions to the effective field, such as surface anisotropy, this boundary condition changes accordingly, see [10].

2.3.5 Properties of the Landau-Lifshitz-Gilbert Equation

Preservation of Modulus

As mentioned in Sec. 2.1 the magnetization $\boldsymbol{m}$ is assumed to be normalized everywhere. This feature is preserved by the Landau-Lifshitz-Gilbert equation. Consider the time derivative of the squared magnetization

$$\partial_t |\boldsymbol{m}|^2 = \partial_t (\boldsymbol{m} \cdot \boldsymbol{m}) = 2\partial_t \boldsymbol{m} \cdot \boldsymbol{m}. \tag{2.3.36}$$

Inserting Eqn. 2.3.17 immediately yields $\partial_t |\boldsymbol{m}|^2 = 0$ and thus also $\partial_t |\boldsymbol{m}| = 0$.

Lyapunov Structure

If the energy functional of a magnetic system does not explicitly depend on the time, i.e. if the external field is constant in time, the time derivative of the energy density may be written as

$$\partial_t U = \frac{\delta U}{\delta \boldsymbol{m}} \cdot \partial_t \boldsymbol{m} \tag{2.3.37}$$

$$= -\mu_0 M_\mathrm{s} \boldsymbol{H}_\mathrm{eff} \cdot \partial_t \boldsymbol{m}. \tag{2.3.38}$$

Replacing $\partial_t \boldsymbol{m}$ with Eqn. 2.3.23 and spatial integration yields

$$\partial_t E = \mu_0 M_\mathrm{s} \int_\Omega \boldsymbol{H}_\mathrm{eff}[\gamma' \boldsymbol{m} \times \boldsymbol{H}_\mathrm{eff} + \alpha' \cdot \boldsymbol{m} \times (\boldsymbol{m} \times \boldsymbol{H}_\mathrm{eff})] \,\mathrm{d}\boldsymbol{r} \tag{2.3.39}$$

$$= -\mu_0 M_\mathrm{s} \alpha' \int_\Omega |\boldsymbol{m} \times \boldsymbol{H}|^2 \,\mathrm{d}\boldsymbol{r} \tag{2.3.40}$$

$$\leq 0. \tag{2.3.41}$$

This means that the energy of a magnetic system is always a non increasing function in time. The Landau-Lifshitz-Gilbert equation is said to have Lyapunov structure [26, 27].

Hamiltonian Structure

In the special case of no damping $\alpha = 0$ the right-hand side of Eqn. 2.3.40 vanishes

$$\partial_t E = 0. \tag{2.3.42}$$

In this case the energy of the system ist preserved and the Landau-Lifshitz-Gilbert equation has Hamiltonian structure.

2.4 Limits and Extensions of the Micromagnetic Model

As discussed in Sec. 2.1 the micromagnetic model introduces a set of simplifications to the quantum mechanical description of magnetism. While justified for a broad range of applications, these simplifications may be inappropriate in some cases. The successfull application of micromagnetism to physical problems requires a solid understanding of the origin of this model. It is crucial to consider its underlying assumptions and simplifications in order to predict the validity of simulation results for specific physical problems. Without claiming to be complete, this section discusses a number of limits and extension to the basic micromagnetic model as introduced in the preceding sections.

Bloch Points

The central assumption in micromagnetics is the homogeneous saturation magnetization M_s. This assumption is justified by the fact that ferromagnetic materials are subject to exchange coupling which leads to locally almost perfectly aligned magnetic moments.

However, certain magnetic processes involve the creation of magnetic singularities called Bloch points. At these Bloch points the magnetization changes rapidly in space, which is inconsistent with the basic assumption of a homogeneous M_s in micromagnetics. Despite this fact it was shown in [28] that micromagnetic simulations involving the creation of Bloch points are able to describe the corresponding processes in accordance with experiments, although the energy density at the Bloch point is underestimated.

Temperature

Another example for the violation of the micromagnetic assumption of a locally homogeneous magnetization is given by thermal effects. Thermal effects are most naturally reflected by local perturbation of magnetic moments. Perturbation of a single magnetic moment, however, obviously breaks the homogeneity of the magnetization. In the framework of classical micromagnetics a possible approach for consideration of finite temperature is the reduction of the saturation magnetization according to a mean-field approximation, see [29]. Another approach is to add a fluctuating field to the effective field, which converts the Landau-Lifshitz-Gilbert equation into a stochastic differential equation, see [30]. Both of these techniques do not account for local changes in the saturation magnetization and as a result both methods fail to describe the magnetization dynamics correctly when approaching the Curie temperature. This deficiency is overcome by the Landau-Lifshitz-Bloch equation, which extends the Landau-Lifshitz-Gilbert equation not only by a fluctuating field, but also by a term that allows the change of the magnetization modulus [31].

Spin Polarized Current

Other successfull extensions to the micromagnetic model include the description of spin polarized currents and its interactions with the magnetization configuration [32]. A famous application for this interaction is the magnetic racetrack memory proposed by Parkin et al. in [6].

Interfaces

The micromagnetic model was designed to describe the energetics and dynamics in a homogeneous material. Thus the description of interfaces between different materials gives rise to

another limit of the model. The magnetic coupling at these interfaces is often not entirely clear and can be subject to quantum mechanical effects that are not covered by the micromagnetic model. These effects include the Ruderman-Kittel-Kasuya-Yosida interaction (RKKY) [33] and the Dzyaloshinskii-Moriya Interaction (DMI) [34]. Work has been done on the integration of these effects into micromagnetic theory and computations, see [35–37]. A common simplification for the description of thin multilayer materials however is the assumption of a bulk material with efficient material constants. These efficient material constants are determined by experiments.

2.5 Solving the Micromagnetic Equations

The Landau-Lifshitz-Gilbert equation with effective field contributions as introduced in the preceding sections is a non-linear partial differential equation in space and time. Apart from some simplified edge cases the arising system of equations cannot be solved analytically. This work is dedicated to the numerical solution of the micromagnetic equations. In the following chapters the discrete solution of the different subproblems is discussed in detail. An overview over existing methods is given and novel methods are introduced. Finally the open-source finite-element micromagnetic simulation code magnum.fe is presented.

CHAPTER 3

Demagnetization Field

The effective field contributions introduced in Sec. 2.3.3 can be classified by their spatial range with respect to the magnetization. The Zeeman field and the anisotropy field are local contributions. While the Zeeman field does not depend on the magnetization at all, the anisotropy field at a certain point $\boldsymbol{r}$ only depends on the magnetization $\boldsymbol{m}(\boldsymbol{r})$ at that point. The exchange field depends on the Laplacian of the magnetization. In order to compute the exchange field at position $\boldsymbol{r}$ the magnetization has to be considered at least in a small area around $\boldsymbol{r}$ so its Laplacian can be computed. The demagnetization field is the only long-range contribution with respect to the magnetization. At every point $\boldsymbol{r}$ the demagnetization field $\boldsymbol{H}_{\text{demag}}(\boldsymbol{r})$ depends on the magnetization at every point in the magnetic region.

This long-range property leads to a high computational complexity of the discrete demagnetization-field calculation, which makes it an interesting topic for performance optimization. While the local and short-range fields are computed with at most $\mathcal{O}(N)$, a naive demagnetization-field algorithm scales with $\mathcal{O}(N^2)$ where N is the total number of simulation cells. Several methods have been proposed to reduce this complexity. These methods can be divided into the group of integral methods and the group of variational methods. While the integral methods rely on the integral expressions in Eqn. 2.2.22 and 2.2.23, the variational methods solve the Poisson equation 2.2.14 directly.

Integral methods include Fourier-transform methods on regular grids [38–40] as well as on irregular grids [41], fast-multipole methods [42, 43], nonuniform grid methods [44], and the recently developed tensor-grid methods [45–48]. Variational methods include variations of the finite-element method and boundary-element method [49, 50]. In the following the Fourier-space methods as well as the finite-element methods are discussed in detail. Note that the demagnetization field $\boldsymbol{H}_{\text{demag}}$ is abbreviated as $\boldsymbol{H}$ throughout this chapter.

3.1 Fourier-Space Methods

Consider an arbitrary partitioning of the magnetic body Ω into simulation cells Ω_i

$$\Omega = \bigcup_i \Omega_i \quad \text{with} \quad \Omega_i \cap \Omega_j = \emptyset \quad \text{if} \quad i \neq j. \tag{3.1.1}$$

In the presented discretization scheme the magnetization is assumed to be constant in every simulation cell Ω_i

$$\boldsymbol{m}(\boldsymbol{r}) = \boldsymbol{m}_i \quad \forall \quad \boldsymbol{r} \in \Omega_i. \tag{3.1.2}$$

Thus the magnetization is represented by $3N$ real values, where N is the number of simulation cells. According to Eqn. 2.2.23 the demagnetization field is the result of a three-dimensional convolution. With the discretization 3.1.1 and 3.1.2 it is given by

$$\boldsymbol{H}(\boldsymbol{r}) = \int_\Omega \widetilde{\boldsymbol{N}}(\boldsymbol{r} - \boldsymbol{r}')\boldsymbol{M}(\boldsymbol{r}')\,\mathrm{d}\boldsymbol{r}' \tag{3.1.3}$$

$$= M_\mathrm{s} \sum_j \left[\int_{\Omega_j} \widetilde{\boldsymbol{N}}(\boldsymbol{r} - \boldsymbol{r}')\,\mathrm{d}\boldsymbol{r}' \right] \boldsymbol{m}_j. \tag{3.1.4}$$

The demagnetization field is usually computed using the same discretization as the magnetization. In order to retrieve a single representative value of the demagnetization field per simulation cell, the average value of the field $\boldsymbol{H}_i$ over each cell Ω_i is computed

$$\boldsymbol{H}_i = M_\mathrm{s} \sum_j \left[\frac{1}{V_i} \int_{\Omega_i} \int_{\Omega_j} \widetilde{\boldsymbol{N}}(\boldsymbol{r} - \boldsymbol{r}')\,\mathrm{d}\boldsymbol{r}\,\mathrm{d}\boldsymbol{r}' \right] \boldsymbol{m}_j \tag{3.1.5}$$

$$= \sum_j \boldsymbol{A}_{ij} \boldsymbol{m}_j \tag{3.1.6}$$

where V_i is the volume of the simulation cell i. The demagnetization-field operator $\boldsymbol{A}$ is a dense $3N \times 3N$ matrix that only depends on the spatial discretization of the problem. This expression can readily be used for the discrete computation of the demagnetization field. However, this method scales with $\mathcal{O}(N^2)$ for both storage requirements and computational complexity and is thus not suited for large-scale problems.

By choosing a periodic spatial discretization the convolution structure of the problem can be exploited on the discrete level. Using a periodic discretization, every simulation cell $\Omega_{\boldsymbol{i}}$ has the same shape as a reference cell Ω_ref

$$\mathbb{1}_{\Omega_i}(\boldsymbol{r}) = \mathbb{1}_{\Omega_\mathrm{ref}}(\boldsymbol{r} - \boldsymbol{r}_{\boldsymbol{i}}). \tag{3.1.7}$$

where $\boldsymbol{i}$ is a multiindex adressing the simulation cell $\Omega_{\boldsymbol{i}}$ and the spatial offset of $\Omega_{\boldsymbol{i}}$ to the reference cell Ω_ref is given by $\boldsymbol{r}_{\boldsymbol{i}}$, see Fig. 3.1. Furthermore the offset from an arbitrary simulation cell $\Omega_{\boldsymbol{i}}$ to another simulation cell $\Omega_{\boldsymbol{j}}$ is the multiple of a cell offset $\Delta\boldsymbol{r}$ in every spatial dimension

$$\boldsymbol{r}_{\boldsymbol{i}} - \boldsymbol{r}_{\boldsymbol{j}} = \sum_k (i_k - j_k)\Delta\boldsymbol{r}_k. \tag{3.1.8}$$

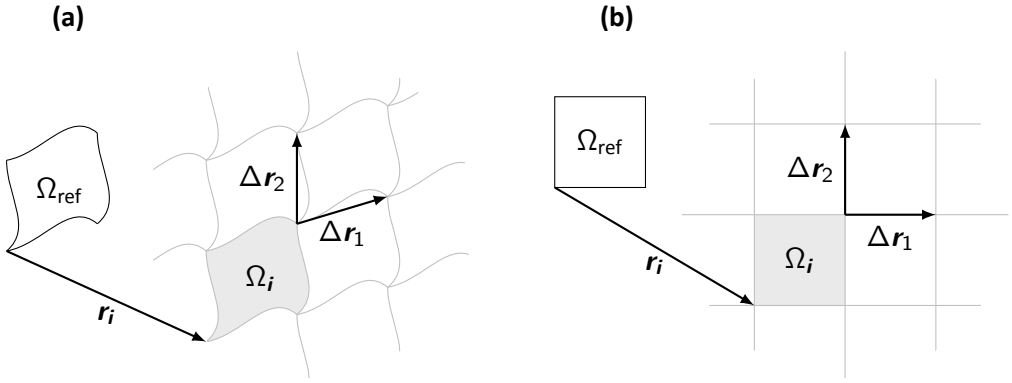

Figure 3.1: Examples for periodic meshes in two dimensions as required by Fourier-space methods. **(a)** A curved reference cell with periodicity along non-orthogonal axes. **(b)** The common rectangular/cubic mesh is a special case of a general periodical mesh.

With Eqn. 3.1.7 and 3.1.8 the integrals in Eqn. 3.1.6 can be converted into integrals over the reference cell Ω_{ref}

$$\boldsymbol{H}_{\boldsymbol{i}} = M_{\text{s}} \sum_{\boldsymbol{j}} \left[\frac{1}{V_{\boldsymbol{i}}} \iint_{\Omega_{\text{ref}}} \widetilde{\boldsymbol{N}} \left(\sum_k (i_k - j_k) \Delta \boldsymbol{r}_k + \boldsymbol{r} - \boldsymbol{r}' \right) \mathrm{d}\boldsymbol{r}\, \mathrm{d}\boldsymbol{r}' \right] \boldsymbol{m}_{\boldsymbol{j}}. \tag{3.1.9}$$

This expression has the form of a three-dimensional discrete convolution

$$\boldsymbol{H}_{\boldsymbol{i}} = M_{\text{s}} \sum_{\boldsymbol{j}} \widetilde{\boldsymbol{N}}_{\boldsymbol{i}-\boldsymbol{j}} \boldsymbol{m}_{\boldsymbol{j}} \tag{3.1.10}$$

$$\widetilde{\boldsymbol{N}}_{\boldsymbol{i}-\boldsymbol{j}} = \frac{1}{V_{\boldsymbol{i}}} \iint_{\Omega_{\text{ref}}} \widetilde{\boldsymbol{N}} \left(\sum_k (i_k - j_k) \Delta \boldsymbol{r}_k + \boldsymbol{r} - \boldsymbol{r}' \right) \mathrm{d}\boldsymbol{r}\, \mathrm{d}\boldsymbol{r}' \tag{3.1.11}$$

since it only depends on the difference of the multiindices $\boldsymbol{i}$ and $\boldsymbol{j}$. Here $\widetilde{\boldsymbol{N}}_{\boldsymbol{i}-\boldsymbol{j}}$ denotes the discrete demagnetization tensor. Note that $\widetilde{\boldsymbol{N}}_{\boldsymbol{i}-\boldsymbol{j}}$ has entries for every possible cell distance which amounts to $\prod_k (2N_k - 1) \approx 2^d N$, where N_k denotes the number of cells in spatial dimension k and d denotes the number of dimensions. This reduces the storage requirements from $\mathcal{O}(N^2)$ for the demagnetization operator $\boldsymbol{A}$ to $\mathcal{O}(N)$ of the demagnetization tensor $\widetilde{\boldsymbol{N}}_{\boldsymbol{i}-\boldsymbol{j}}$. However, the naive implementation of the convolution in Eqn. 3.1.10 still has a computational complexity of $\mathcal{O}(N^2)$.

3.1.1 Convolution Theorem

This complexity can be reduced by application of the convolution theorem. The discrete convolution theorem states that the convolution can be expressed as a cell-wise multiplication in Fourier space

$$\mathcal{F}(f * g) = \mathcal{F}(f)\mathcal{F}(g) \tag{3.1.12}$$

where $\mathcal{F}$ denotes the discrete Fourier transform and $f * g$ is the discrete convolution given by

$$(f * g)_i = \sum_j f_j \; g_{i-j}. \tag{3.1.13}$$

The formulae in Eqn. 3.1.12 and 3.1.13 are defined for one-dimensional sequences f and g. However, the convolution in Eqn. 3.1.10 is multidimensional in two ways. First the convolution is defined between a tensor $\widetilde{\boldsymbol{N}}$ and a vector $\boldsymbol{m}$. Due to the linearity of the convolution, the tensor–vector multiplication can be exchanged with the convolution operation which yields

$$H_{k,\boldsymbol{i}} = M_\mathrm{s} \sum_l \sum_{\boldsymbol{j}} N_{kl,\boldsymbol{i}-\boldsymbol{j}} \; m_{l,\boldsymbol{j}}. \tag{3.1.14}$$

Furthermore the convolution is defined on a three-dimensional grid that is addressed by the multiindices $\boldsymbol{i}$ and $\boldsymbol{j}$. Writing these indices as triples of scalars $\boldsymbol{i} = (i_1, i_2, i_3)$ yields

$$H_{k,i_1,i_2,i_3} = M_\mathrm{s} \sum_{l,j_1,j_2,j_3} N_{kl,i_1-j_1,i_2-j_2,i_3-j_3} \; m_{l,j_1,j_2,j_3}. \tag{3.1.15}$$

By processing each index j_x separately this expression can be written as nested sums of one-dimensional convolutions. Starting with the index j_3 yields an outer sum over one-dimensional convolutions

$$\begin{aligned} H_{k,i_1,i_2,i_3} &= M_\mathrm{s} \sum_{l,j_1,j_2} \sum_{j_3} N_{kl,i_1-j_1,i_2-j_2,i_3-j_3} \; m_{l,j_1,j_2,j_3} && (3.1.16)\\ &= M_\mathrm{s} \sum_{l,j_1,j_2} N_{kl,i_1-j_1,i_2,-j_2} * m_{l,j_1,j_2} && (3.1.17) \end{aligned}$$

where the convolution operator $*$ acts on the free indices $i_3 - j_3$ and j_3 respectively. Consider the corresponding Fourier-transform operator $\mathcal{F}_x$ that applies the Fourier transform of an object a_{i_1,i_2,i_3} in i_x-direction for all possible tuples of the remaining indices. With this operator the convolution in Eqn. 3.1.17 can be written as

$$\begin{aligned} H_{k,i_1,i_2,i_3} &= M_\mathrm{s} \sum_l \mathcal{F}_3^{-1} \left[\sum_{j_1,j_2} \mathcal{F}_3(N_{kl})_{i_1-j_1,i_2-j_2} \; \mathcal{F}_3(m_l)_{j_1,j_2} \right]_{i_3} && (3.1.18)\\ &= M_\mathrm{s} \sum_l \mathcal{F}_3^{-1} \left[\sum_{j_1} \mathcal{F}_3(N_{kl})_{i_1-j_1} * \mathcal{F}_3(m_l)_{j_1} \right]_{i_3} && (3.1.19)\\ &\vdots \\ &= M_\mathrm{s} \sum_l \boldsymbol{\mathcal{F}}^{-1} \left[\boldsymbol{\mathcal{F}}(N_{kl}) \; \boldsymbol{\mathcal{F}}(m_l) \right]_{i_1,i_2,i_3} && (3.1.20) \end{aligned}$$

where $\boldsymbol{\mathcal{F}} = \mathcal{F}_1\mathcal{F}_2\mathcal{F}_3$ is the three-dimensional Fourier transform. The exchange of Fourier transform and summation as used in Eqn. 3.1.18 is possible due to the linearity of the Fourier transform. This algorithm is often referred to as row-column algorithm [51].

As mentioned above the convolution reduces to a cell-wise muliplication in Fourier space leading to a computational complexity of $\mathcal{O}(N)$. This complexity however does not account for the additional computational costs due to the Fourier transform. The fast Fourier transform algorithm (FFT) by Cooley and Tukey [52] has a complexity of $\mathcal{O}(N \log N)$ which superseeds the complexity of the multiplication and thus gives a measure for the overall complexity of the convolution computation.

3.1.2 Discrete Demagnetization Tensor

The presented convolution method for the computation of the demagnetization field is applicable for arbitrary discretizations as long as they are periodic in the sense described in Eqn. 3.1.7 and 3.1.8. However, the computation of the discrete demagnetization tensor $\widetilde{\boldsymbol{N}}_{\boldsymbol{i}-\boldsymbol{j}}$ for complicated reference cells as shown in Fig. 3.1a might be unfeasible.

For cuboid cells as shown in Fig. 3.1b the discrete tensor $\widetilde{\boldsymbol{N}}_{\boldsymbol{i}-\boldsymbol{j}}$ given by Eqn. 3.1.11 was computed analytically by Newell et al. [53]. According to Newell the diagonal element $N_{1,1}$ of the tensor is given by

$$N_{1,1}(\boldsymbol{r}, \Delta\boldsymbol{r}) = \frac{1}{4\pi\Delta r_1 \Delta r_2 \Delta r_3} \sum_{\boldsymbol{i},\boldsymbol{j}\in\{0,1\}} (-1)^{\sum_x i_x + j_x} \\ f[r_1 + (i_1 - j_1)\Delta r_1, r_2 + (i_2 - j_2)\Delta r_2, r_3 + (i_3 - j_3)\Delta r_3] \quad (3.1.21)$$

where the function f is defined by

$$\begin{aligned} f(r_1, r_2, r_3) = {} & \frac{|r_2|}{2}(r_3^2 - r_1^2)\sinh^{-1}\left(\frac{|r_2|}{\sqrt{r_1^2 + r_3^2}}\right) \\ & + \frac{|r_3|}{2}(r_2^2 - r_1^2)\sinh^{-1}\left(\frac{|r_3|}{\sqrt{r_1^2 + r_2^2}}\right) \\ & - |r_1 r_2 r_3|\tan^{-1}\left(\frac{|r_2 r_3|}{r_1\sqrt{r_1^2 + r_2^2 + r_3^2}}\right) \\ & + \frac{1}{6}(2r_1^2 - r_2^2 - r_3^2)\sqrt{r_1^2 + r_2^2 + r_3^2}. \end{aligned} \quad (3.1.22)$$

The elements $N_{2,2}$ and $N_{3,3}$ are obtained by circular permutation of the coordinates

$$N_{2,2}(\boldsymbol{r}, \Delta\boldsymbol{r}) = N_{1,1}[(r_2, r_3, r_1), (\Delta r_2, \Delta r_3, \Delta r_1)] \quad (3.1.23)$$

$$N_{3,3}(\boldsymbol{r}, \Delta\boldsymbol{r}) = N_{1,1}[(r_3, r_1, r_2), (\Delta r_3, \Delta r_1, \Delta r_2)]. \quad (3.1.24)$$

The off-diagonal element $N_{1,2}$ is given by

$$N_{1,2}(\boldsymbol{r}, \Delta\boldsymbol{r}) = \frac{1}{4\pi\Delta r_1 \Delta r_2 \Delta r_3} \sum_{\boldsymbol{i},\boldsymbol{j}\in\{0,1\}} (-1)^{\sum_x i_x + j_x} \\ g[r_1 + (i_1 - j_1)\Delta r_1, r_2 + (i_2 - j_2)\Delta r_2, r_3 + (i_3 - j_3)\Delta r_3] \quad (3.1.25)$$

where the function g is defined by

$$\begin{aligned} g(r_1, r_2, r_3) = {} & (r_1 r_2 r_3) \sinh^{-1}\left(\frac{r_3}{\sqrt{r_1^2 + r_2^2}}\right) \\ & + \frac{r_2}{6}(3r_3^2 - r_2^2) \sinh^{-1}\left(\frac{r_1}{\sqrt{r_2^2 + r_3^2}}\right) \\ & + \frac{r_1}{6}(3r_3^2 - r_1^2) \sinh^{-1}\left(\frac{r_2}{\sqrt{r_1^2 + r_3^2}}\right) \\ & - \frac{r_3^3}{6} \tan^{-1}\left(\frac{r_1 r_2}{r_3\sqrt{r_1^2 + r_2^2 + r_3^2}}\right) - \frac{r_3 r_2^2}{2} \tan^{-1}\left(\frac{r_1 r_3}{r_2\sqrt{r_1^2 + r_2^2 + r_3^2}}\right) \\ & - \frac{r_3 r_1^2}{2} \tan^{-1}\left(\frac{r_2 r_3}{r_1\sqrt{r_1^2 + r_2^2 + r_3^2}}\right) - \frac{r_1 r_2 \sqrt{r_1^2 + r_2^2 + r_3^2}}{3}. \end{aligned} \tag{3.1.26}$$

Again other off-diagonal elements are obtained by permutation of coordinates

$$N_{1,3}(\boldsymbol{r}, \Delta\boldsymbol{r}) = N_{1,2}[(r_1, r_3, r_2), (\Delta r_1, \Delta r_3, \Delta r_2)] \tag{3.1.27}$$

$$N_{2,3}(\boldsymbol{r}, \Delta\boldsymbol{r}) = N_{1,2}[(r_2, r_3, r_1), (\Delta r_2, \Delta r_3, \Delta r_1)]. \tag{3.1.28}$$

Like the continuous tensor $\widetilde{\boldsymbol{N}}(\boldsymbol{r} - \boldsymbol{r}')$ the discrete tensor $\widetilde{\boldsymbol{N}}_{\boldsymbol{i}-\boldsymbol{j}}$ is symmetric

$$N_{ij} = N_{ji}. \tag{3.1.29}$$

Thus the above definitions of $N_{1,2}$, $N_{1,3}$ and $N_{2,3}$ can be used to obtain the remaining off-diagonal elements.

Instead of this analytical expression, Eqn. 3.1.11 can also be integrated numerically in order to retrieve the entries of the discrete demagnetization tensor. As shown by Lebecki et al. in [54] and Krüger et al. in [55] numerical integration leads to more accurate results in some cases, especially for large cell distances $\boldsymbol{r}$.

3.1.3 Scalar Potential

In the preceding sections the demagnetization field is directly computed as the result of a convolution. An alternative approach is the computation of the field as gradient of the scalar potential u. With Eqn. 2.2.22 the demagnetization field is given by

$$\boldsymbol{H}(\boldsymbol{r}) = -\boldsymbol{\nabla} u \tag{3.1.30}$$

$$= -M_s \boldsymbol{\nabla} \int_\Omega \boldsymbol{S}(\boldsymbol{r} - \boldsymbol{r}') \cdot \boldsymbol{m}(\boldsymbol{r}')\, \mathrm{d}\boldsymbol{r}' \tag{3.1.31}$$

$$\boldsymbol{S}(\boldsymbol{r} - \boldsymbol{r}') = \frac{1}{4\pi} \boldsymbol{\nabla}' \frac{1}{|\boldsymbol{r} - \boldsymbol{r}'|} \tag{3.1.32}$$

Assuming again a discretized magnetization as in Eqn. 3.1.2 that is constant per cell Ω_i yields

$$u(\boldsymbol{r}) = M_\mathrm{s} \sum_j \left[\int_{\Omega_j} \boldsymbol{S}(\boldsymbol{r} - \boldsymbol{r}')\, \mathrm{d}\boldsymbol{r}' \right] \cdot \boldsymbol{m}_j \tag{3.1.33}$$

for the scalar potential at an arbitrary point $\boldsymbol{r}$. For a periodic spatial discretization that fulfills Eqn. 3.1.7 and 3.1.8 this expression can be turned into a discrete convolution

$$u_{\boldsymbol{i}} = M_\mathrm{s} \sum_j \boldsymbol{S}_{\boldsymbol{i}-\boldsymbol{j}} \cdot \boldsymbol{m}_j \tag{3.1.34}$$

$$\boldsymbol{S}_{\boldsymbol{i}-\boldsymbol{j}} = \int_{\Omega_j} \boldsymbol{S}(\boldsymbol{r}_{\boldsymbol{i}} - \boldsymbol{r}')\, \mathrm{d}\boldsymbol{r}' \tag{3.1.35}$$

$$= \int_{\Omega_\mathrm{ref}} \boldsymbol{S} \left(\sum_k (i_k - j_k) \Delta \boldsymbol{r}_k - \boldsymbol{r}' \right) \mathrm{d}\boldsymbol{r}' \tag{3.1.36}$$

where $\boldsymbol{S}_{\boldsymbol{i}-\boldsymbol{j}}$ does only depend on the difference of the multiindices $\boldsymbol{i}$ and $\boldsymbol{j}$. For cuboid simulation cells this integral can be calculated analytically. First the volume integral is converted into a surface integral with the divergence theorem

$$\boldsymbol{S}_{\boldsymbol{i}-\boldsymbol{j}} = \frac{1}{4\pi} \int_{\Omega_j} \boldsymbol{\nabla} \frac{1}{|\boldsymbol{r}_{\boldsymbol{i}} - \boldsymbol{r}'|}\, \mathrm{d}\boldsymbol{r}' \tag{3.1.37}$$

$$= \frac{1}{4\pi} \int_{\partial\Omega_j} \frac{\boldsymbol{n}'}{|\boldsymbol{r}_{\boldsymbol{i}} - \boldsymbol{r}'|}\, \mathrm{d}\boldsymbol{s}'. \tag{3.1.38}$$

Consider the r_3-component of the vector field $\boldsymbol{S}$. For cuboid regions $\Omega_{\boldsymbol{i}}$, which are aligned with the three principal axes, only the planes perpendicular to the r_3-direction contribute to the surface integral

$$S_3(\boldsymbol{r}, \Delta\boldsymbol{r}) = \sum_\pm \pm \frac{1}{4\pi} \int_{-\Delta r_1/2}^{\Delta r_1/2} \int_{-\Delta r_2/2}^{\Delta r_2/2} \frac{\mathrm{d}r_1' \mathrm{d}r_2'}{\sqrt{(r_1 - r_1')^2 + (r_2 - r_2')^2 + (r_3 \mp \Delta r_3/2)^2}} \tag{3.1.39}$$

where $\boldsymbol{r}$ denotes the distance to the center of the cuboid and $\Delta\boldsymbol{r}$ denotes the dimensions of the cuboid. The indefinite surface integral can be evaluated as

$$\begin{aligned} F(r_1, r_2, r_3) &= \frac{1}{4\pi} \iint \frac{\mathrm{d}r_1 \mathrm{d}r_2}{\sqrt{r_1^2 + r_2^2 + r_3^2}} \\ &= \frac{1}{4\pi} \Bigg\{ - r_3 \arctan \left(\frac{r_1 r_2}{r_3 \sqrt{r_1^2 + r_2^2 + r_3^2}} \right) \\ &+ r_2 \ln \left(r_1 + \sqrt{r_1^2 + r_2^2 + r_3^2} \right) \\ &+ r_1 \ln \left(r_2 + \sqrt{r_1^2 + r_2^2 + r_3^2} \right) \Bigg\}. \end{aligned} \tag{3.1.40}$$

Assembling the definite integrals in Eqn. 3.1.39 yields

$$S_3(\boldsymbol{r}, \Delta\boldsymbol{r}) = \sum_{i,j,k \in \{-1,1\}} -ijk F\left(r_1 + i\tfrac{\Delta r_1}{2}, r_2 + j\tfrac{\Delta r_2}{2}, r_3 + k\tfrac{\Delta r_3}{2}\right). \tag{3.1.41}$$

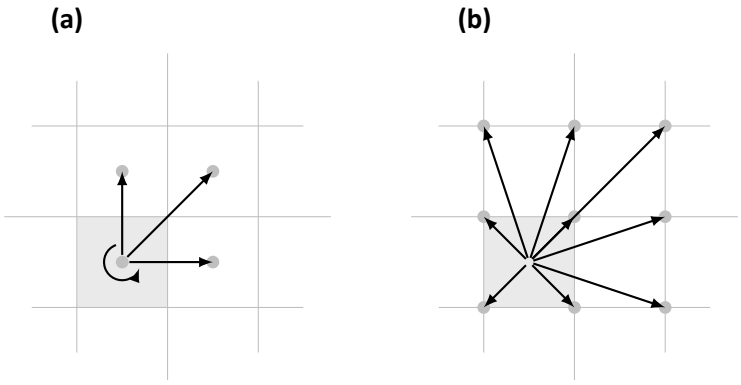

Figure 3.2: Evaluation of the scalar potential generated by a source cell. The source cell is colored gray. **(a)** Evaluation at cell centers. **(b)** Evaluation at cell vertices.

The remaining components of the vector field $\boldsymbol{S}$ are obtained by cyclic permutation

$$S_1(\boldsymbol{r}, \Delta\boldsymbol{r}) = \sum_{i,j,k} -ijkF(r_2 + i\tfrac{\Delta r_2}{2}, r_3 + j\tfrac{\Delta r_3}{2}, r_1 + k\tfrac{\Delta r_1}{2}) \tag{3.1.42}$$

$$S_2(\boldsymbol{r}, \Delta\boldsymbol{r}) = \sum_{i,j,k} -ijkF(r_3 + i\tfrac{\Delta r_3}{2}, r_1 + j\tfrac{\Delta r_1}{2}, r_2 + k\tfrac{\Delta r_2}{2}). \tag{3.1.43}$$

By application of the convolution theorem the potential u is thus computed by

$$u_{\boldsymbol{i}} = \sum_k \mathcal{F}^{-1}[\mathcal{F}(S_k)\mathcal{F}(m_k)]_{\boldsymbol{i}}. \tag{3.1.44}$$

In contrast to the direct calculation of the demagnetization field, the potential is not averaged over a cell, but computed at distinct points. These sampling points have the same periodicity as the spatial discretization. However, their relative position in a cell can be chosen by adding an offset to the computation of $\boldsymbol{S}$.

In order to obtain the actual demagnetization field, the gradient of the potential has to be computed. On a cuboid grid the approximation of the gradient is naturally given by finite differences. A possible choice for the sample points of the potential are the cell centers, see Fig. 3.2a. However, in order to compute the gradient per cell in a symmetric fashion, the potential difference from the neighboring cells has to be evaluated. For the r_1-component this reads

$$H_{1,\boldsymbol{i}} \approx \frac{u_{i_1+1,i_2,i_3} - u_{i_1-1,i_2,i_3}}{2\Delta r_1}. \tag{3.1.45}$$

For boundary elements the value for at least one of the neighboring cells might not be available. In particular it is not possible to retrieve the finite-difference approximation if the region is discretized by a single cell in one dimension.

This problem can be avoided by choosing the sample points at the vertices of the cuboid mesh, see Fig. 3.2b. With this choice the averaged demagnetization field can be computed up to first

order by the averaged finite-differences of the cell vertices

$$H_{1,\boldsymbol{i}} \approx \sum_{\Delta_2,\Delta_3\in\{-1/2,1/2\}} \frac{u_{i_1+1/2,i_2+\Delta_2,i_3+\Delta_3} - u_{i_1-1/2,i_2+\Delta_2,i_3+\Delta_3}}{\Delta r_1}. \tag{3.1.46}$$

The method described by Eqn. 3.1.44 and 3.1.46 was introduced in [40] and is referred to as scalar-potential method for the demagnetization-field computation.

3.1.4 Performance Considerations

Both the direct computation of the demagnetization field, in the following referred to as demagnetization-tensor method, and the scalar-potential method have an asymptotic computational complexity of $\mathcal{O}(N \log N)$. However, a close look at the operation counts shows that the scalar-potential method has certain advantages over the demagnetization-tensor method.

For the latter the Fourier transform has to be applied to the components of the demagnetization-tensor and the magnetization. Then a tensor-field–vector-field multiplication and an inverse Fourier transform on the components of the resulting field is carried out. Due to the symmetry of the demagnetization tensor, its Fourier transform is calculated by six FFT computations. Since this tensor does only depend on the choice of the spatial discretization it has to be computed only once for the solution of a time dependent problem. The following computations have to be carried out in every timestep:

- three 3D FFTs to transform the magnetization field
- one tensor-field–vector-field multiplication in Fourier space
- three inverse 3D FFTs to transform the resulting demagnetization field

The setup of the scalar potential method requires the Fourier transform of the field $\boldsymbol{S}$. For every timestep the following operations are required:

- three 3D FFTs to transform the magnetization field
- one vector-field–vector-field multiplication in Fourier space
- one inverse 3D FFT to transform the resulting potential
- one finite-difference computation of the demagnetization-field

Note that the scalar-potential method requires only four FFTs in total per timestep whereas the demagnetization-tensor method requires six. Since the FFT is the operation with the highest complexity it is expected that the overall computation time for a single timestep can be reduced to approximately 2/3 by the scalar-potential method. Furthermore the tensor-field–vector-field multiplication is reduced to a vector-field–vector-field multiplication. Also note that the memory required to store the demagnetization-tensor field $\widetilde{\boldsymbol{N}}$ is two times the memory required to store the vector-field $\boldsymbol{S}$.

The downside of the scalar-potential method is the additional gradient computation. This adds another $\mathcal{O}(N)$ operation to the procedure, which is not significant due to the leading $\mathcal{O}(N \log N)$ complexity of the FFT. However, it introduces another approximation error.

3.2 Finite-Element Methods

An alternative formulation of the Poisson problem 2.2.14 is given by

$$\boldsymbol{\nabla} \cdot (\boldsymbol{\nabla} u - M_\mathrm{s} \boldsymbol{m}) = 0. \tag{3.2.1}$$

Opposed to the original Poisson problem this expression is defined in the whole space even if the magnetization $\boldsymbol{M}$ is discontinuous which is the case at the boundary of an ideal magnet. In this case the discontinuity is compensated by the field $\boldsymbol{H} = -\boldsymbol{\nabla} u$.

Consider the following formulation arising from multiplication of Eqn. 3.2.1 with a so-called test function v and integration over a region Ω

$$\int_\Omega \boldsymbol{\nabla} \cdot (\boldsymbol{\nabla} u - M_\mathrm{s} \boldsymbol{m}) v \, \mathrm{d}\boldsymbol{r} = 0. \tag{3.2.2}$$

Integration by parts yields

$$\int_\Omega \boldsymbol{\nabla} u \cdot \boldsymbol{\nabla} v \, \mathrm{d}\boldsymbol{r} = M_\mathrm{s} \int_\Omega \boldsymbol{m} \cdot \boldsymbol{\nabla} v \, \mathrm{d}\boldsymbol{r} + \int_{\partial\Omega} \boldsymbol{n} \cdot (\boldsymbol{\nabla} u - M_\mathrm{s} \boldsymbol{m}) v \, \mathrm{d}\boldsymbol{s}. \tag{3.2.3}$$

Restriction of the test functions v to the Sobolev space H_0^1 defined by

$$H_0^1 = \{ v \in H^1(\Omega) : v = 0 \text{ on } \partial\Omega \}. \tag{3.2.4}$$

leads to a vanishing boundary term in Eqn. 3.2.3. Demanding Eqn. 3.2.3 for all $v \in H_0^1$ thus yields

$$\int_\Omega \boldsymbol{\nabla} u \cdot \boldsymbol{\nabla} v \, \mathrm{d}\boldsymbol{r} = M_\mathrm{s} \int_\Omega \boldsymbol{m} \cdot \boldsymbol{\nabla} v \, \mathrm{d}\boldsymbol{r} \; \forall \; v \in H_0^1. \tag{3.2.5}$$

This expression can be written as

$$a(u, v) = L(v) \; \forall \; v \in H_0^1 \tag{3.2.6}$$

with the bilinear form $a(u, v)$ and the linear form $L(v)$ defined by

$$a(u, v) = \int_\Omega \boldsymbol{\nabla} u \cdot \boldsymbol{\nabla} v \, \mathrm{d}\boldsymbol{r} \tag{3.2.7}$$

$$L(v) = M_\mathrm{s} \int_\Omega \boldsymbol{m} \cdot \boldsymbol{\nabla} v \, \mathrm{d}\boldsymbol{r}. \tag{3.2.8}$$

According to the Lax-Milgram theorem this problem has a unique solution u when restricting the solution to H_0^1, since the bilinear form $a(u, v)$ is coercive [56]. If the original problem 3.2.1 with Dirichlet boundary condition $u = 0$ on $\partial\Omega$ has a classical solution, this solution coincides

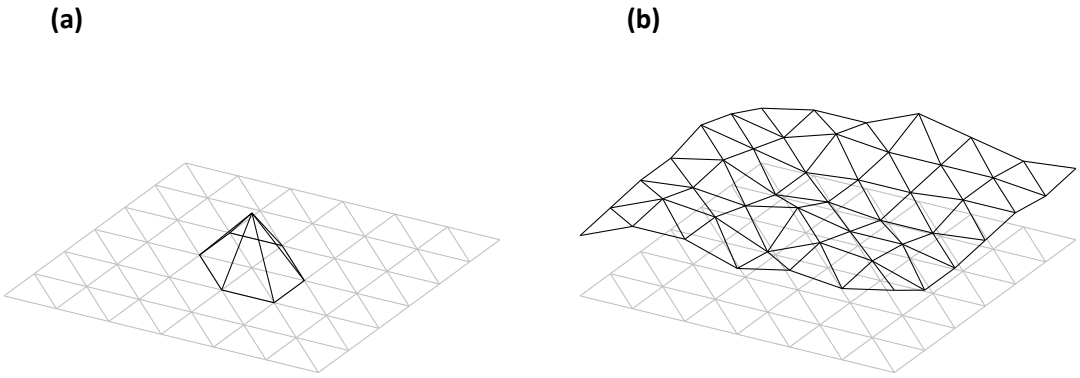

Figure 3.3: Discrete function space of first order Lagrange functions in two dimensions. **(a)** A single basis function, often referred to as hat function. **(b)** Example function from the span of the hat-function basis.

with the solution of Eqn. 3.2.5 as can be shown by integration by parts. However, in general the requirements on the solution of Eqn. 3.2.5 are weaker than on the solution of the original problem 3.2.1. The original solution has to be twice differentiable whereas the solution of Eqn. 3.2.5 has to be only once weakly differentiable. Thus Eqn. 3.2.5 is called a weak formulation of the problem and the solution u is called a weak solution.

In order to solve Eqn. 3.2.1 with inhomogeneous boundary conditions, we have to seek for the solution in the function space H^1. In particular it can be shown that there exists a unique $u \in H^1$ to the problem

$$a(u, v) = L(v) \; \forall \; v \in H_0^1 \tag{3.2.9}$$

$$u - u_0 \in H_0^1 \tag{3.2.10}$$

where $u_0 \in H^1$ is an arbitrary function that satisfies the Dirichlet boundary condition.

The finite-element method is also capable of solving the Poisson equation for given Neuman boundary conditions. The Poisson equation with Neuman boundary conditions determines the solution only up to a constant. Hence the solution is usually restricted to a function space $V = \{v \in H^1(\Omega); \int_\Omega v \, \mathrm{d}\boldsymbol{r} = 0\}$. Since the function space for the test and trial functions is a subspace of H^1, the boundary integral in Eqn. 3.2.3 does not vanish. The Neuman boundary conditions are thus naturally included in the weak formulation. It can be shown that the resulting bilinear form is coercive on V and thus a unique solution can be found according to the theorem of Lax Milgram [56].

3.2.1 Discretization

The weak formulation 3.2.5 can be discretized by choice of a suitable finite dimensional function space $V_h \subset H^1$. This function space is usually constructed using a polyhedral mesh. The cells of this mesh along with the construction rules of the function space are called finite elements. Following Ciarlet [57] a finite element is defined by the triple $T, \mathcal{V}, \mathcal{L}$, where

T is the domain of a cell;
$\mathcal{V}$ is a finite dimensional function space on the domain T;
$\mathcal{L}$ is the set of degrees of freedom $\mathcal{L} = \{l_1, l_2, \dots, l_n\}$, which is a basis for the dual space $\mathcal{V}'$.

Additionally a mapping from the local degrees of freedom per cell to the global degrees of freedom is defined. This mapping couples the cells and ensures that the global discrete function space satisfies the continuity requirements of V_h. For actual computations the degrees of freedom l_i are usually used to construct a basis of $\mathcal{V}$ by

$$l_i(\phi_j) = \delta_{ij} \tag{3.2.11}$$

where ϕ_j denote the basis functions.

The simplest choice of a finite element is the so-called Lagrange element of first order. The domain T is usually given as a triangle in two dimensions and a tetrahedron in three dimensions and the function space $\mathcal{V}(T)$ is that of first order polynomials $\mathcal{P}_1$. The degrees of freedom represented by the functionals l_i are given as point evaluations on the vertices of the mesh

$$l_i(v) = v(\boldsymbol{r}_i) \tag{3.2.12}$$

where $\boldsymbol{r}_i$ denotes the ith vertex of the cell. This results in a straightforward local-to-global mapping since neighboring cells share certain vertices. The corresponding basis functions ϕ_i are according to Eqn. 3.2.11 given by $\phi_i(\boldsymbol{r}_j) = \delta_{ij}$ with $\boldsymbol{r}_j$ being the jth vertex of the mesh. Figure 3.3 shows the basis functions of the Lagrange element of first order for a two-dimensional triangulation. As reference to their shape in two dimensions, which is shown in Fig. 3.3a, the first-order Lagrange basis functions are often referred to as hat functions.

The first-order Lagrange elements are generalized to higher-order elements by piecewise polynomial, globally continuous functions. In this case the mesh nodes are complemented by auxiliary nodes in order to construct a suitable dual basis. The support of the basis functions of any order is given by the corresponding cell domains. The number of nodes per cell, however, is increased for higher order. This leads to a loss a sparsity of the system matrices, which is the main drawback of higher-order methods.

The general definition of a finite element by Ciarlet allows for a great variety of finite elements that differ mainly in polynomial order and continuity properties, see [57]. However, this work mainly focuses on the standard Lagrange elements.

Using the finite dimensional function space V_h, each function u_h is described by a tuple of coefficients u_i

$$u_h = \sum_i u_i \phi_i \tag{3.2.13}$$

where ϕ_i are the global basis functions. The discrete weak form 3.2.5 reads

$$\int_\Omega \nabla u_h \cdot \nabla v_h \, \mathrm{d}\boldsymbol{r} = M_\mathrm{s} \int_\Omega \boldsymbol{m} \cdot \nabla v_h \, \mathrm{d}\boldsymbol{r} \; \forall \; v_h \in V_h \tag{3.2.14}$$

with $u_h \in V_h$. Due to the linearity in v_h it is sufficient to test Eqn. 3.2.14 with the basis functions ϕ_i. Inserting Eqn. 3.2.13 and exchanging summation with integration yields

$$\sum_i u_i \int_\Omega \nabla \phi_i \cdot \nabla \phi_j \, \mathrm{d}\boldsymbol{r} = M_\mathrm{s} \int_\Omega \boldsymbol{m} \cdot \nabla \phi_j \, \mathrm{d}\boldsymbol{r}. \tag{3.2.15}$$

This system can be written as a matrix–vector multiplication

$$\sum_i A_{ij} u_i = b_j \tag{3.2.16}$$

with the matrix A and the vector b given by

$$A_{ij} = \int_\Omega \nabla \phi_i \cdot \nabla \phi_j \, \mathrm{d}\boldsymbol{r} \tag{3.2.17}$$

$$b_j = M_\mathrm{s} \int_\Omega \boldsymbol{m} \cdot \nabla \phi_j \, \mathrm{d}\boldsymbol{r}. \tag{3.2.18}$$

The matrix A is symmetric positive definite and thus the system 3.2.16 has a unique solution. Furthermore the discrete solution u_h satisfies certain optimality conditions and error bounds depending on the spatial discretization can be computed. For a detailed analytical treatment of this method the reader is referred to standard finite-element literature [56, 58].

The matrix entries A_{ij} are zero for non-overlapping basis functions ϕ_i and ϕ_j. Depending on the used finite element and the mesh, a large number of matrix entries is zero. In case of the first-order Lagrange functions A_{ij} is nonzero for neighboring vertices i and j. Thus the matrix A is sparse and has an asymptotic storage requirement of $\mathcal{O}(N)$. The sparsity of the system matrix is an important feature of the finite-element method.

However, solving the problem 3.2.16 usually requires the inverse of A to be computed, which results in a dense matrix. This procedure can be avoided by application of iterative methods for the solution of linear systems [59]. These methods usually require a matrix–vector multiplication per iteration, which can be computed with $\mathcal{O}(N)$ for the given sparse matrices.

3.2.2 Open-Boundary Problem

In order to solve dynamic micromagnetic problems, the demagnetization field has to be computed only within the magnetic sample. The finite-element method is well suited for the solution of the Poisson equation arising from the demagnetization-field problem. However, the

boundary conditions have to be known for this method. For the demagnetization-field problem the boundary conditions are given at infinity by Eqn. 2.2.16. Several methods have been proposed to compute the demagnetization field on a finite mesh with the finite-element method. In the following the simple truncation method and the popular boundary-element coupling method are briefly discussed. In Sec. 3.2.3 the so-called shell-transformation method is discussed in detail.

Truncation

A simple approach for the solution of the open-boundary problem is the truncation method. The mesh of the magnetic sample is extended by a large but finite exterior region. The Dirichlet condition is applied to the surface of the exterior region.

This method adds a large overhead due to the additional elements, but the exterior space is still not described accurately, since the boundary condition is applied at finite distance to the sample.

Hybrid FEM-BEM Method

A popular method for the solution of the demagnetization-field problem in the framework of the finite-element method is a hybrid method proposed by Fredkin and Koehler involving the boundary-element method. In the following the main idea of this method is sketched. For a detailed description the reader is referred to the original publication [49].

Beside the open boundary condition 2.2.16 the following jump conditions at the sample boundary of an ideal magnet can be derived for the demagnetization problem

$$u^{\text{in}} - u^{\text{out}} = 0 \tag{3.2.19}$$

$$(\boldsymbol{\nabla} u^{\text{in}} - \boldsymbol{\nabla} u^{\text{out}}) \cdot \boldsymbol{n} = \boldsymbol{m} \cdot \boldsymbol{n} \tag{3.2.20}$$

where u^{in} denotes the value of the potential in the sample whereas u^{out} denotes the corresponding value outside. Consider the following splitting of the potential u

$$u = u_1 + u_2. \tag{3.2.21}$$

Let u_1 be the solution to the following system

$$\Delta u_1 = -\boldsymbol{\nabla} \cdot \boldsymbol{m} \tag{3.2.22}$$

$$\frac{\partial u_1}{\partial \boldsymbol{n}} = \boldsymbol{n} \cdot \boldsymbol{m} \text{ on } \partial\Omega \tag{3.2.23}$$

in the sample and zero outside. This solution satisfies the continuity condition 3.2.20, but violates condition 3.2.19. Thus u_2 has to fix Eqn. 3.2.19 while preserving Eqn. 3.2.20

$$u_2^{\text{in}} - u_2^{\text{out}} = u_1^{\text{in}} \tag{3.2.24}$$

$$\frac{\partial u_2^{\text{in}}}{\partial \boldsymbol{n}} - \frac{\partial u_2^{\text{out}}}{\partial \boldsymbol{n}} = 0 \tag{3.2.25}$$

From potential theory it is known that these requirements are met by a double layer potential given by

$$u_2 = \int_{\partial\Omega} u_1 \frac{\partial}{\partial \boldsymbol{n}} \frac{1}{|\boldsymbol{r} - \boldsymbol{r}'|} \, \mathrm{d}\boldsymbol{r}. \tag{3.2.26}$$

This expression can be evaluated in order to compute u_2 in the whole sample. However, the computational complexity of this step amounts to $\mathcal{O}(N^2)$. Hence this expression is usually only used to compute the values of u_2 on the boundary $\partial\Omega$ with the boundary-element method. The values of u_2 within the sample are computed with the finite-element method, where Dirichlet boundary conditions are taken from the boundary-element calculation.

An alternative coupling approach was presented by García-Cervera and Roma in [60]. For this approach a homogeneous and an inhomogenous Dirichlet problem have to be solved with the finite-element method and the boundary-element method is used to retrieve a single-layer potential.

For both coupling approaches the boundary-element method provides a linear system of size $M \times M$, where M is the number of boundary nodes. In contrast to the matrices arising from the finite-element discretization, the boundary-element matrices are dense. A common approach to handle systems with a large number of boundary nodes is the use of hierachical matrices for the compression of the dense systems [61].

3.2.3 Shell-Transformation Method

In the preceding section two methods for the solution of the open-boundary problem with the finite-element method were briefly discussed. The truncation method replaces the infinitely large exterior region with a finite region whereas the boundary-element coupling delivers boundary conditions at the sample boundary for finite-element computations. In this work a so-called shell-transformation method was applied for the demagnetization-field computation [50, 62, 63]. This method outperforms the truncation method by considering the whole exterior space, but it leads to a single sparse and linear problem in contrast to the boundary-element coupling.

Consider a region Ω_{sphere} that is spherical and includes the magnetic region Ω_{sample}. This region is surrounded by a spherical shell Ω_{shell}, see Fig. 3.4. The finite spherical shell Ω_{shell} is mapped

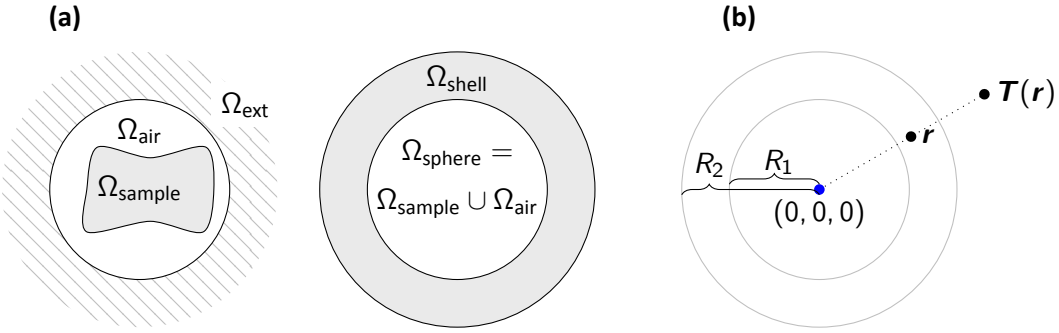

Figure 3.4: Spherical shell transformation method in two dimensions. **(a)** Definitions of involved regions. **(b)** Sketch of transformation.

onto the infinite exterior region $\Omega_{\text{ext}} \in \mathbb{R}^3 \backslash \Omega_{\text{sphere}}$ via a bijective transformation $\boldsymbol{T}(\boldsymbol{r})$

$$\boldsymbol{T} : \Omega_{\text{shell}} \to \Omega_{\text{ext}}. \tag{3.2.27}$$

Integration over $\Omega_{\text{ext}} = \boldsymbol{T}(\Omega_{\text{shell}})$ can be replaced by integration over Ω_{shell} via substitution

$$\int_{\Omega_{\text{ext}}} f[\boldsymbol{T}^{-1}(\boldsymbol{r}')] \, \mathrm{d}\boldsymbol{r}' = \int_{\Omega_{\text{shell}}} f(\boldsymbol{r}) \, |\det[D\boldsymbol{T}(\boldsymbol{r})]| \, \mathrm{d}\boldsymbol{r}. \tag{3.2.28}$$

The function $f_{\text{t}}(\boldsymbol{r}') = f[\boldsymbol{T}^{-1}(\boldsymbol{r}')]$ is a 'stretched' version of $f(\boldsymbol{r})$ which is defined on Ω_{ext}. This method can be used to turn the weak formulation 3.2.5 on the finite region Ω to an effective weak formulation on the whole space $\mathbb{R}^3$ by 'stretching' the test and trial functions. However, the integrand of the left-hand side of Eqn. 3.2.5 does not depend on the test and trial functions, but on their gradients. By using Eqn. 3.2.28 the gradients in the integrand still apply to the untransformed variables $\boldsymbol{r}$ rather than to the transformed variables $\boldsymbol{r}' = \boldsymbol{T}(\boldsymbol{r})$. The gradient $\boldsymbol{\nabla}$ with respect to $\boldsymbol{r}$ is connected to the gradient $\boldsymbol{\nabla}'$ with respect to $\boldsymbol{r}'$ by

$$\boldsymbol{\nabla} g = \begin{pmatrix} \frac{\partial g}{\partial r_1} \\ \frac{\partial g}{\partial r_2} \\ \frac{\partial g}{\partial r_3} \end{pmatrix} = \begin{pmatrix} \frac{\partial r_1'}{\partial r_1} & \frac{\partial r_2'}{\partial r_1} & \frac{\partial r_3'}{\partial r_1} \\ \frac{\partial r_1'}{\partial r_2} & \frac{\partial r_2'}{\partial r_2} & \frac{\partial r_3'}{\partial r_2} \\ \frac{\partial r_1'}{\partial r_3} & \frac{\partial r_2'}{\partial r_3} & \frac{\partial r_3'}{\partial r_3} \end{pmatrix} \begin{pmatrix} \frac{\partial g}{\partial r_1'} \\ \frac{\partial g}{\partial r_2'} \\ \frac{\partial g}{\partial r_3'} \end{pmatrix} = \boldsymbol{J} \, \boldsymbol{\nabla}' g \tag{3.2.29}$$

and hence

$$[\boldsymbol{\nabla}' g](\boldsymbol{r}') = [\boldsymbol{J}^{-1} \boldsymbol{\nabla} g](\boldsymbol{r}') \tag{3.2.30}$$

with $\boldsymbol{J} = D\boldsymbol{T}(\boldsymbol{r})$ being the Jacobian of the transformation. Thus the shell-transformed weak formulation reads

$$\int_{\Omega_{\text{sphere}}} \nabla u \cdot \nabla v \, \mathrm{d}\boldsymbol{r} + \int_{\Omega_{\text{shell}}} (\nabla u)^T \boldsymbol{g} \, \nabla v \, \mathrm{d}\boldsymbol{r} = M_{\text{s}} \int_{\Omega_{\text{sample}}} \boldsymbol{m} \cdot \nabla v \, \mathrm{d}\boldsymbol{r} \; \forall \; v \in V \tag{3.2.31}$$

with the metric tensor $\boldsymbol{g}$ given by

$$\boldsymbol{g} = (\boldsymbol{J}^{-1})^T \, |\det \boldsymbol{J}| \, \boldsymbol{J}^{-1}. \tag{3.2.32}$$

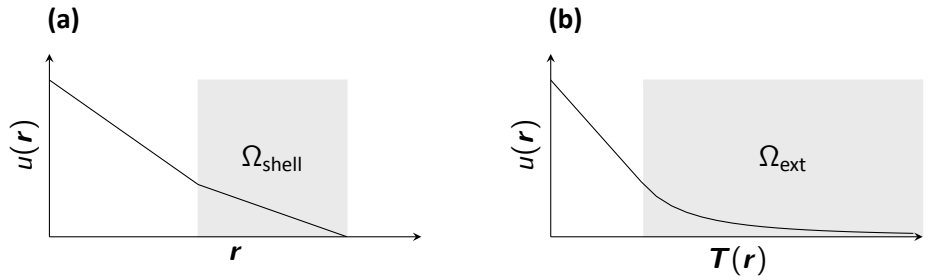

Figure 3.5: Distorsion of test and trial functions due to the transformation. **(a)** Linear decay of the potential u in the untransformed shell. **(b)** The same function mapped onto the exterior region by a suitable transformation.

Since the integral over the shell Ω_{shell} represents the integration over the exterior region Ω_{ext} the open-boundary conditions can be applied as regular Dirichlet boundary conditions $u(\boldsymbol{r}) = 0$ at the outer boundary of the shell $\partial\Omega$.

The metric tensor $\boldsymbol{g}$ is symmetric positive definite, hence the symmetric bilinear form on the left-hand side of Eqn. 3.2.31 is also positive definite. Thus by the right choice of the subspace $V \subset H_0^1$, problem Eqn. 3.2.31 has a unique solution.

Choice of Transformation

A reasonable choice for the transformation on a spherical shell is the radial mapping

$$\boldsymbol{T}(\boldsymbol{r}) = t(|\boldsymbol{r}|)\frac{\boldsymbol{r}}{|\boldsymbol{r}|} \tag{3.2.33}$$

The scalar function $t(r) \in \mathcal{C}^\infty(\Omega_{\text{shell}})$ is strictly increasing and fulfills

$$t(R_1) = R_1 \tag{3.2.34}$$

$$t(r) \to \infty \text{ for } r \to R_2. \tag{3.2.35}$$

Thus the transformation $\boldsymbol{T}(\boldsymbol{r})$ is bijective and fulfills Eqn. 3.2.27 as required. Obviously there are many possible choices for $t(r)$ that meet these requirements. A suitable transformation distorts the basis functions used for discretization in a way that the decay of the potential u may be approximated accurately, see Fig. 3.5. From Eqn. 2.2.22 it is known that the potential u decays with $u \propto 1/|\boldsymbol{r}|^2$ in the far-field approximation.

Consider the radial part of an affine basis function

$$\phi(r) = a + br \tag{3.2.36}$$

in the untransformed space. In order to obtain a function decaying with $1/r'^2$ in the transformed space, the scalar function $t(r)$ has to fulfill

$$r = a' + b'\frac{1}{[t(r)]^2} \tag{3.2.37}$$

and thus

$$t(r) = \sqrt{\frac{b'}{r - a'}} \tag{3.2.38}$$

Furthermore the function t has to fulfill Eqn. 3.2.34 and 3.2.35, which leads to

$$t(R_1) = \sqrt{\frac{b'}{R_1 - a'}} = R_1 \tag{3.2.39}$$

$$1/t(R_2) = \sqrt{\frac{R_2 - a'}{b'}} = 0. \tag{3.2.40}$$

This immediately results in

$$t(r) = R_1 \sqrt{\frac{R_2 - R_1}{R_2 - r}} \tag{3.2.41}$$

as suitable mapping for linear basis functions. The metric tensor $\boldsymbol{g}$ of the transformation $\boldsymbol{T}(\boldsymbol{r})$ is computed by inserting Eqn. 3.2.41 into Eqn. 3.2.33 and 3.2.32 which yields

$$g_{ii}(\boldsymbol{r}) = \frac{R_1\sqrt{R_2 - R_1}(4R_2^2 r_i^2 - 8R_2 r_i^2|\boldsymbol{r}| + 3|\boldsymbol{r}|^2 r_i^2 + |\boldsymbol{r}|^4)}{2|\boldsymbol{r}|^4(R_2 - |\boldsymbol{r}|)^{3/2}} \tag{3.2.42}$$

$$g_{ij}(\boldsymbol{r}) = \frac{R_1\sqrt{R_2 - R_1} r_i r_j(4R_2^2 - 8R_2|\boldsymbol{r}| + 3|\boldsymbol{r}|^2)}{2|\boldsymbol{r}|^4(R_2 - |\boldsymbol{r}|)^{3/2}} \text{ for } i \neq j \tag{3.2.43}$$

With this expression the demagnetization-field can be computed by discretization of the weak formulation 3.2.31. The discretization is applied as described in Sec. 3.2.1. In contrast to the basic Poisson problem, the computation of the system-matrix entries involves integration over the metric tensor $\boldsymbol{g}$. In order to compute these integrals, the metric tensor $\boldsymbol{g}$ is interpolated onto a high-order polynomial space. This process is equivalent to the numerical integration with Gaussian quadrature.

In order to obtain a smooth transition from the untransformed to the transformed region, the Jacobian $\boldsymbol{J}$ is required to equal the identity matrix $\mathbb{1}$ on the inner boundary of the shell $\partial\Omega_{\text{sphere}}$. This is exactly the case for $R_1/R_2 = 2/3$. Hence the shell is always constructed according to this ratio and the accuracy of the transformation method is entirely controlled by the resolution of the mesh within the shell.

Higher Order Functions

The quality of the discrete solution can be significantly improved by the use of higher-order polynomials as test and trials functions. For test and trial function of order higher than one the transformation

$$t(r) = R_1 \frac{R_2 - R_1}{R_2 - r}. \tag{3.2.44}$$

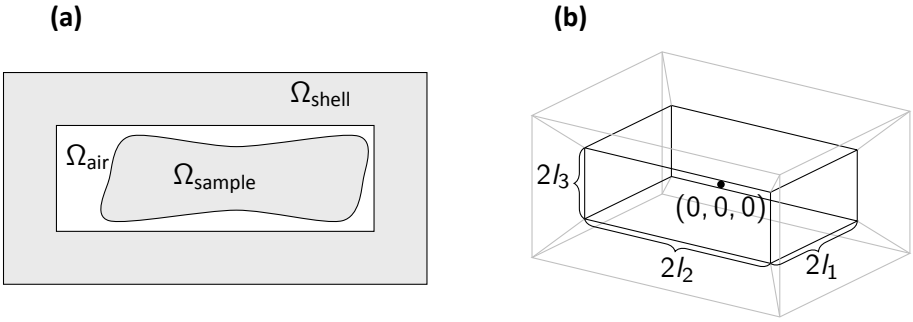

Figure 3.6: Cuboid shell transformation method. **(a)** The involved regions in two dimensions. **(b)** Cuboid shell patches in three dimensions. The coordinate origin $(0, 0, 0)$ is located at the center of the cuboid. The length vector $\boldsymbol{l}$ is defined by the edges of Ω_{air}.

instead of Eqn. 3.2.41 is used. With this transformation, second and third order polynomial functions transform like

$$a + br + cr^2 \to a' + b'\frac{1}{r'} + c'\frac{1}{r'^2} \tag{3.2.45}$$

$$a + br + cr^2 + dr^3 \to a' + b'\frac{1}{r'} + c'\frac{1}{r'^2} + d'\frac{1}{r'^3}. \tag{3.2.46}$$

The additional terms $1/r'$ and $1/r'^3$ facilitate a much better approximation of the decaying scalar potential u. The resulting metric tensor $\boldsymbol{g}$ for the spherical shell transformation is given by

$$g_{ii}(\boldsymbol{r}) = \frac{R_1(R_2 - R_1)(R_2^2 r_i^2 - 2R_2 r_i^2|\boldsymbol{r}| + |\boldsymbol{r}|^4)}{|\boldsymbol{r}|^4(R_2 - |\boldsymbol{r}|)^2} \tag{3.2.47}$$

$$g_{ij}(\boldsymbol{r}) = \frac{R_1 R_2(R_2 - R_1) r_i r_j (R_2 - 2|\boldsymbol{r}|)}{|\boldsymbol{r}|^4(R_2 - |\boldsymbol{r}|)^2} \text{ for } i \neq j \tag{3.2.48}$$

Cuboid Shell Transformation

The spherical shell transformation is a natural choice for spherical samples. For non-spherical samples this method might still be a good choice if the untransformed non-magnetic region Ω_{air} as defined in Fig. 3.4a is small compared to the sample region. However, for certain geometries, such as magnetic thin films, the region Ω_{air} is much larger than the magnetic sample Ω_{sample}. This leads to a large overhead in the discrete problem, because Ω_{air} has to be meshed as well as Ω_{sample}.

In [50] the use of a cuboid shell is proposed. Figure 3.6a shows the regions for this cuboid shell transformation. When using a spherical shell, the inner radius of the shell is the only parameter available to minimize the region Ω_{air}. In contrast, the cuboid shell offers the three side-lengths as parameters, see Fig. 3.6b. Furthermore the relative rotation of the sample to the shell may

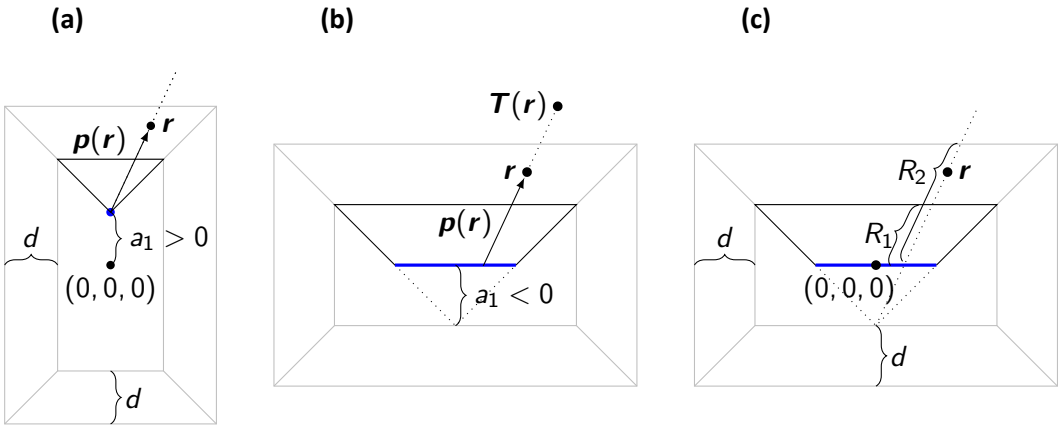

Figure 3.7: Sketch of the cuboid transformation method in two dimensions. The transformation of the upper shell patch is visualized. **(a)** Transformation for positive a_1. In this case the origin of the transformation is fixed at a single point. **(b)** Transformation for negative a_1. In this case the origin of the transformation is moving on the middle plane of the magnetic region. This construction ensures continuity across patch borders since the transformation of the narrow patch and the wide patch share the same origin on the border. **(c)** In contrast to the spherical shell transformation the parameters R_1 and R_2 vary with $\boldsymbol{r}$.

be adjusted to minimize Ω_{air}. Hence the cuboid shell-transformation method offers a greater flexibility regarding sample shapes.

The scalar mappings from Eqn. 3.2.41 and 3.2.44 can be reused for the cuboid shell tansformation. However, the origin of the transformation as well as the parameters R_1 and R_2 have to be adapted depending on the position $\boldsymbol{r}$ within the shell. The shell is divided into six cuboid shell patches of equal thickness as shown in Fig. 3.6b. The transformation $\boldsymbol{T}(\boldsymbol{r})$ is constructed per shell patch with the same requirements as the spherical version. Points on the inner boundary of the shell have to be mapped onto itself while points on the outer boundary of the shell are mapped to infinity. An additional requirement is the continuity of the transformation $\boldsymbol{T}(\boldsymbol{r})$ across patch borders.

The construction of origin and direction of the transformation depending on the position $\boldsymbol{r}$ within the shell is depicted in Fig. 3.7. In general the transformation origin $\boldsymbol{O}$ is a function of $\boldsymbol{r}$ in order to obtain continuity across shell-patch borders. In contrast to the mapping described in [50], the transformation in this work is designed such that the origin $\boldsymbol{O}(\boldsymbol{r})$ always resides within the magnetic sample. Consider the following auxiliary constants for the transformation

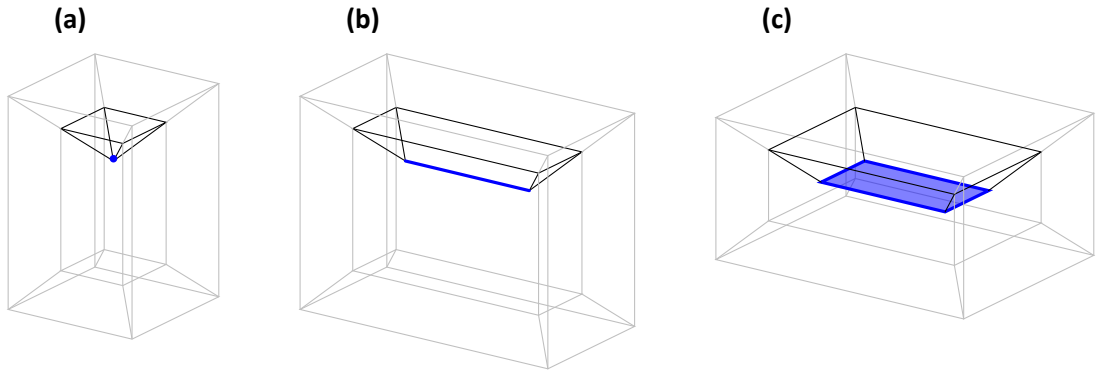

Figure 3.8: Transformation origins in three dimensions. The blue area marks the set of possible origins for a specific shell patch. **(a)** Special case of square shaped patch where $a_1 = a_2 > 0$. The transformation origin is fixed for the whole patch. **(b)** Rectangular patch shape with $a_1 > 0$. The transformation origin moves on a line. **(c)** Rectangular path shape with $a_1 < 0$ and $a_2 < 0$. The transformation origin moves on the middle plane of the magnetic region.

of the shell patch in the positive r_3-half-space

$$a_1 = l_3 - l_1 \tag{3.2.49}$$

$$a_2 = l_3 - l_2. \tag{3.2.50}$$

The third component of the transformation origin O_3 is given by

$$O_3 = \max(a_1, a_2, 0). \tag{3.2.51}$$

This component does obviously not depend of the position $\boldsymbol{r}$. The choice of O_3 in two dimensions is depicted in Fig. 3.7. Figure 3.7a sketches the transformation for a positive a_1, whereas Fig. 3.7b and 3.7c refer to a negative a_1. The possible positions for the origins $\boldsymbol{O}(\boldsymbol{r})$ are marked as blue points and lines. A three-dimensional visualization of $\boldsymbol{O}(\boldsymbol{r})$ is shown in Fig. 3.8. The remaining components of $\boldsymbol{O}(\boldsymbol{r})$ are obtained by application of the intercept theorem

$$\boldsymbol{O}(\boldsymbol{r}) = \left(r_1 \frac{O_3 - a_1}{r_3 - a_1}, r_2 \frac{O_3 - a_2}{r_3 - a_2}, O_3 \right)^T. \tag{3.2.52}$$

With the distance vector $\boldsymbol{p}(\boldsymbol{r}) = \boldsymbol{r} - \boldsymbol{O}(\boldsymbol{r})$, the parameters R_1 and R_2 as depicted in Fig. 3.7b are given by

$$R_1(\boldsymbol{r}) = |\boldsymbol{p}(\boldsymbol{r})| \, \frac{l_3 - O_3}{r_3 - O_3} \tag{3.2.53}$$

$$R_2(\boldsymbol{r}) = |\boldsymbol{p}(\boldsymbol{r})| \, \frac{(l_3 + d) - O_3}{r_3 - O_3}. \tag{3.2.54}$$

Similar to the spherical method, the actual transformation of the shell patch in the positive r_3-half-space $\boldsymbol{T}_{3+}$ is defined in terms of a scalar mapping $t(\boldsymbol{r})$

$$\boldsymbol{T}_{3+}(\boldsymbol{r}) = \boldsymbol{O}(\boldsymbol{r}) + t(\boldsymbol{r}) \frac{\boldsymbol{p}(\boldsymbol{r})}{|\boldsymbol{p}(\boldsymbol{r})|}. \tag{3.2.55}$$

The scalar mapping is chosen similar to Eqn. 3.2.41 and 3.2.44

$$t(\boldsymbol{r}) = R_1(\boldsymbol{r}) \left[\frac{R_2(\boldsymbol{r}) - R_1(\boldsymbol{r})}{R_2(\boldsymbol{r}) - |\boldsymbol{p}(\boldsymbol{r})|} \right]^n \tag{3.2.56}$$

where n is set to $1/2$ for linear basis functions and to 1 otherwise. In the following sections the analytical expressions for the metric tensor for linear as well as higher order basis functions are presented.

Similar to the spherical shell-transformation method, the thickness of the shell d is chosen such that the Jacobian $\boldsymbol{J}$ is the identity on the inner boundary of the shell. This is exactly the case for $d = \min(l_1, l_2, l_3)$.

Metric Tensor for Linear Basis Functions

According to Eqn. 3.2.32 the metric tensor $\boldsymbol{g}$ is determined by the Jacobian determinant $|\det \boldsymbol{J}|$ and the inverse Jacobian matrix $\boldsymbol{J}^{-1}$ of the transformation $\boldsymbol{T}(\boldsymbol{r})$. For improved readability consider the following auxiliary constants

$$A = \sqrt{(r_3 - O_3)^2 + \left(r_1 - \frac{r_1(-O_1 + O_3)}{-O_1 + r_3} \right)^2 + \left(r_2 - \frac{r_2(-O_2 + O_3)}{-O_2 + r_3} \right)^2} \tag{3.2.57}$$

$$B = \sqrt{\frac{A(d + l_3 - r_3)}{r_3 - O_3}} \tag{3.2.58}$$

$$C = \sqrt{\frac{dA}{r_3 - O_3}} \tag{3.2.59}$$

$$D = -(-2B + 3C)(-l_3 + r_3)(-l_3 + O_3) \tag{3.2.60}$$

$$E = -2Bl_3 + Cl_3 + 2Br_3 - CO_3. \tag{3.2.61}$$

Setting $n = 1/2$ in Eqn. 3.2.56 and inserting into Eqn. 3.2.55 yields the following expressions for $|\det \boldsymbol{J}_{3+}|$ and $\boldsymbol{J}_{3+}^{-1}$ for $\boldsymbol{T}_{3+}$

$$|\det \boldsymbol{J}_{3+}|(\boldsymbol{r}) = \frac{C(l_3 - O_3)(-Bl_1 + (-B + C)(-l_3 + O_3))(-Bl_2 + (-B + C)(-l_3 + O_3))}{2B^3(d + l_3 - r_3)(l_1 - l_3 + r_3)(l_2 - l_3 + r_3)} \tag{3.2.62}$$

$$
\begin{aligned}
J_{3+,11}(\boldsymbol{r}) =& \frac{B(-l_1 + l_3 - r_3)}{-Bl_1 + (-B + C)(-l_3 + O_3)} \\
J_{3+,12}(\boldsymbol{r}) =& 0 \\
J_{3+,13}(\boldsymbol{r}) =& 0 \\
J_{3+,21}(\boldsymbol{r}) =& 0 \\
J_{3+,22}(\boldsymbol{r}) =& \frac{B(-l_2 + l_3 - r_3)}{-Bl_2 + (-B + C)(-l_3 + O_3)} \\
J_{3+,23}(\boldsymbol{r}) =& 0 \\
J_{3+,31}(\boldsymbol{r}) =& -\frac{dr_1(-l_1 + l_3 - r_3)B^3(D + l_1E + 2d(-Bl_1 + (-B + C)(-l_3 + O_3)))}{(d + l_3 - r_3)(l_1 - l_3 + r_3)^2(l_3 - O_3)C^3(-Bl_1 + (-B + C)(-l_3 + O_3))} \\
J_{3+,32}(\boldsymbol{r}) =& -\frac{dr_2(-l_2 + l_3 - r_3)B^3(D + l_2E + 2d(-Bl_2 + (-B + C)(-l_3 + O_3)))}{(d + l_3 - r_3)(l_2 - l_3 + r_3)^2(l_3 - O_3)C^3(-Bl_2 + (-B + C)(-l_3 + O_3))} \\
J_{3+,33}(\boldsymbol{r}) =& \frac{2dB^3}{(l_3 - O_3)C^3}.
\end{aligned} \tag{3.2.63}
$$

These expressions apply for the shell patch lying in the positive r_3-half-space. Due to symmetry the transformation for the patch in the negative r_3-half-space is obtained by point mirroring the position $\boldsymbol{r}$ in the origin

$$
\boldsymbol{g}_3 = \begin{cases} \boldsymbol{g}_{3+}(\boldsymbol{r}) & \text{if } r_3 > 0 \\ \boldsymbol{g}_{3+}(-\boldsymbol{r}) & \text{if } r_3 < 0 \end{cases} \tag{3.2.64}
$$

where $\boldsymbol{g}_{3+}$ is defined by

$$
\boldsymbol{g}_{3+} = (\boldsymbol{J}_{3+}^{-1})^T |\det \boldsymbol{J}_{3+}| \boldsymbol{J}_{3+}^{-1}. \tag{3.2.65}
$$

The transformations for the remaining shell patches are obtained by cyclic permutation of the coordinates

$$
\boldsymbol{g}_1[\boldsymbol{r}] = \boldsymbol{g}_3[(r_2, r_3, r_1)^T]\Big|_{\boldsymbol{l}=(l_2,l_3,l_1)^T, \boldsymbol{O}=(O_2,O_3,O_1)^T} \tag{3.2.66}
$$

$$
\boldsymbol{g}_2[\boldsymbol{r}] = \boldsymbol{g}_3[(r_3, r_1, r_2)^T]\Big|_{\boldsymbol{l}=(l_3,l_1,l_2)^T, \boldsymbol{O}=(O_3,O_1,O_2)^T}. \tag{3.2.67}
$$

Note that not only the coordinates of the position $\boldsymbol{r}$ are permuted, but also the coordinates of the side-length vector $\boldsymbol{l}$ and the origin $\boldsymbol{O}$.

Metric Tensor for Higher Order Basis Functions

Setting $n = 1$ in Eqn. 3.2.56 and inserting into Eqn. 3.2.55 yields the following for the transformation $\boldsymbol{T}_{3+}(\boldsymbol{r})$ for higher order basis functions

$$
\begin{aligned}
&|\det \boldsymbol{J}_{3+}|(\boldsymbol{r}) = \\
&\qquad \frac{d(l_3 - O_3)(dl_1 + (l_3 - r_3)(l_1 - l_3 + O_3))(dl_2 + (l_3 - r_3)(l_2 - l_3 + O_3))}{(d + l_3 - r_3)^4(l_1 - l_3 + r_3)(l_2 - l_3 + r_3)}
\end{aligned} \tag{3.2.68}
$$

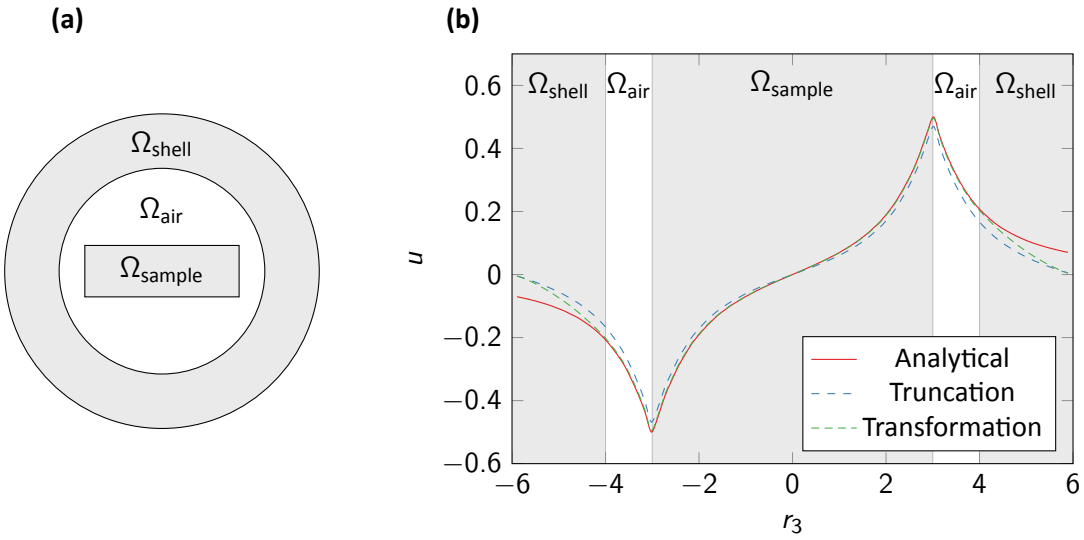

Figure 3.9: Scalar potential calculation of a homogeneously magnetized cuboid with the spherical shell transformation method. **(a)** Sketch of the setup in two dimensions. The cuboid sample with edge lengths $(2, 2, 6)$ is surrounded by a sphere with radius $R_1 = 4$. **(b)** Results of the potential computation on the r_3 axis $u[(0, 0, r_3)^T]$. The results of a truncation approach and the spherical transformation are compared to the analytical potential. The different regions are marked with background colors.

$$
\begin{aligned}
J^{-1}_{3+,11}(\boldsymbol{r}) &= \frac{(d + l_3 - r_3)(l_1 - l_3 + r_3)}{dl_1 + (l_3 - r_3)(l_1 - l_3 + O_3)} \\
J^{-1}_{3+,12}(\boldsymbol{r}) &= 0 \\
J^{-1}_{3+,13}(\boldsymbol{r}) &= 0 \\
J^{-1}_{3+,21}(\boldsymbol{r}) &= 0 \\
J^{-1}_{3+,22}(\boldsymbol{r}) &= \frac{(d + l_3 - r_3)(l_2 - l_3 + r_3)}{dl_2 + (l_3 - r_3)(l_2 - l_3 + O_3)} \\
J^{-1}_{3+,23}(\boldsymbol{r}) &= 0 \\
J^{-1}_{3+,31}(\boldsymbol{r}) &= r_1(d + l_3 - r_3)\left(\frac{d + l_3 - r_3}{d(l_1 - l_3 + r_3)(l_3 - O_3)} - \frac{1}{dl_1 + (l_3 - r_3)(l_1 - l_3 + O_3)}\right) \\
J^{-1}_{3+,32}(\boldsymbol{r}) &= r_2(d + l_3 - r_3)\left(\frac{d + l_3 - r_3}{d(l_2 - l_3 + r_3)(l_3 - O_3)} - \frac{1}{dl_2 + (l_3 - r_3)(l_2 - l_3 + O_3)}\right) \\
J^{-1}_{3+,33}(\boldsymbol{r}) &= \frac{(d + l_3 - r_3)^2}{d(l_3 - O_3)}
\end{aligned}
\tag{3.2.69}
$$

Similar to the transformation for linear basis functions, the metric tensor $\boldsymbol{g}$ for a particular shell patch is obtained by Eqns. 3.2.64–3.2.67.

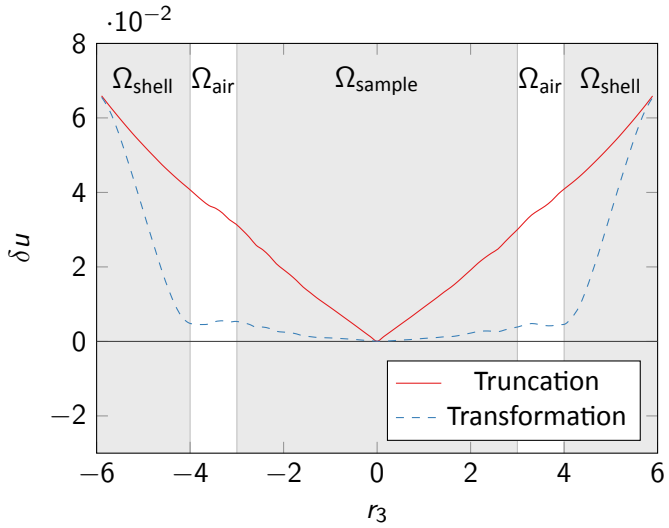

Figure 3.10: Relative error δu of the potential computation for a homogeneously magnetized cuboid, see also Fig. 3.9. The result of the truncation approach is compared to the result of the transformation method. The different regions are marked with background colors.

3.2.4 Validation and Numerical Experiments

As a first validation of the transformation methods presented in the preceding section, the scalar potential u is computed for a homogeneously magnetized cuboid. This problem is well suited as a functional test, since the analytical solution for u is known, see Sec. 3.1.3. Furthermore both the approximation of the cuboid sample geometry with tetrahedra as well as the approximation of the constant magnetization with piecewise polynomial functions is exact. Figure 3.9a shows the configuration in two dimensions. The side lengths of the cuboid are chosen as $\boldsymbol{L} = (2, 2, 6)^T$ and the radii of the spherical shell are chosen as $R_1 = 4$ and $R_2 = 6$. The homogeneous magnetization within the sample is set to $\boldsymbol{M} = (0, 0, 1)$. The computation of the potential u is done with the spherical shell-transformation method described in Sec. 3.2.3 with linear basis functions. For comparison a simple truncation approach on the same mesh is implemented, where the metric tensor in Eqn. 3.2.31 is replaced by the identity.

The computed potential on the r_3-axis $u[(0, 0, r_3)^T]$ is plotted in Fig. 3.9b along with the analytical solution. For both methods Dirichlet conditions $u = 0$ are applied on the outer shell boundary, which is reflected in the potential values at $z = \{-6, 6\}$. In contrast to the truncation method, the transformation method features a steeper ascend of the potential in the shell region Ω_{shell}, such that the deviation of the computed potential in the untransformed area $\Omega_{\text{air}} \cup \Omega_{\text{sample}}$ is smaller than the deviation of the truncation method. Figure 3.10 shows the error to the analytical computation in the the different regions. While the error of the truncation method linearly varies with the distance to the center of the sample, the error of the transfor-

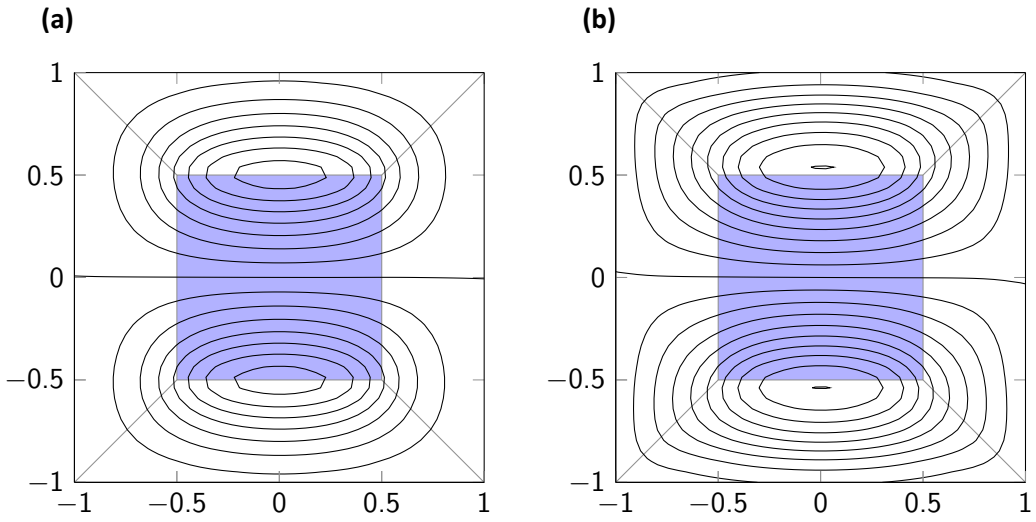

Figure 3.11: Equipotential lines of the computed scalar potential u of a homogeneously magnetized cube at the middle plane. **(a)** Result computed with a truncation approach. The shape of the contour lines is close to that of a magnetic dipole. **(b)** Result computed with the cuboid shell-transformation method. The contour lines show a clear distorsion due to the transformation. Furthermore the density of contour lines is higher compared to the truncation method.

mation method almost drops to zero on the boundary between the regions Ω_{shell} and Ω_{air}. This is the expected result, since the transformation method simulates the complete exterior space.

This fact is also reflected by the equipotential lines of the potential u. Figure 3.11 shows the equipotential lines for the cuboid shell transformation applied on a uniformly magnetized unit cube with $\boldsymbol{M} = (0, 0, 1)^T$. Compared to the truncation method, the potential lines of the transformation method show a higher density in the shell region Ω_{shell}. The spatial distorsion of the shell region, that is effectively applied by the transformation method by mapping the cuboid shell region on the complete exterior space, leads to distorted potential lines in Fig. 3.11b.

As explained in Sec. 3.2.3, the cuboid shell transformation superseeds the spherical shell transformation in terms of flexibility. Hence the rest of this work is dedicated to the cuboid shell transformation only. However, the presented findings of the cuboid method usually also apply to the spherical method. Figure 3.12a shows the energy of a uniformly magnetized unit cube, calculated with different polynomial degree of test and trial functions along with the analytical solution. The demagnetization energy is computed according to Eqn. 2.2.25, the analytical solution for a uniformly magnetized unit cube is given by $E_{\text{uni}} = 1/6\mu_0 M_s^2$. The methods are compared with respect to the number of nonzero matrix entries of the linear systems resulting from the discretization of Eqn. 3.2.31. This is considered a good measure for comparsion since both the storage requirements and the computational complexity of matrix–vector multiplica-

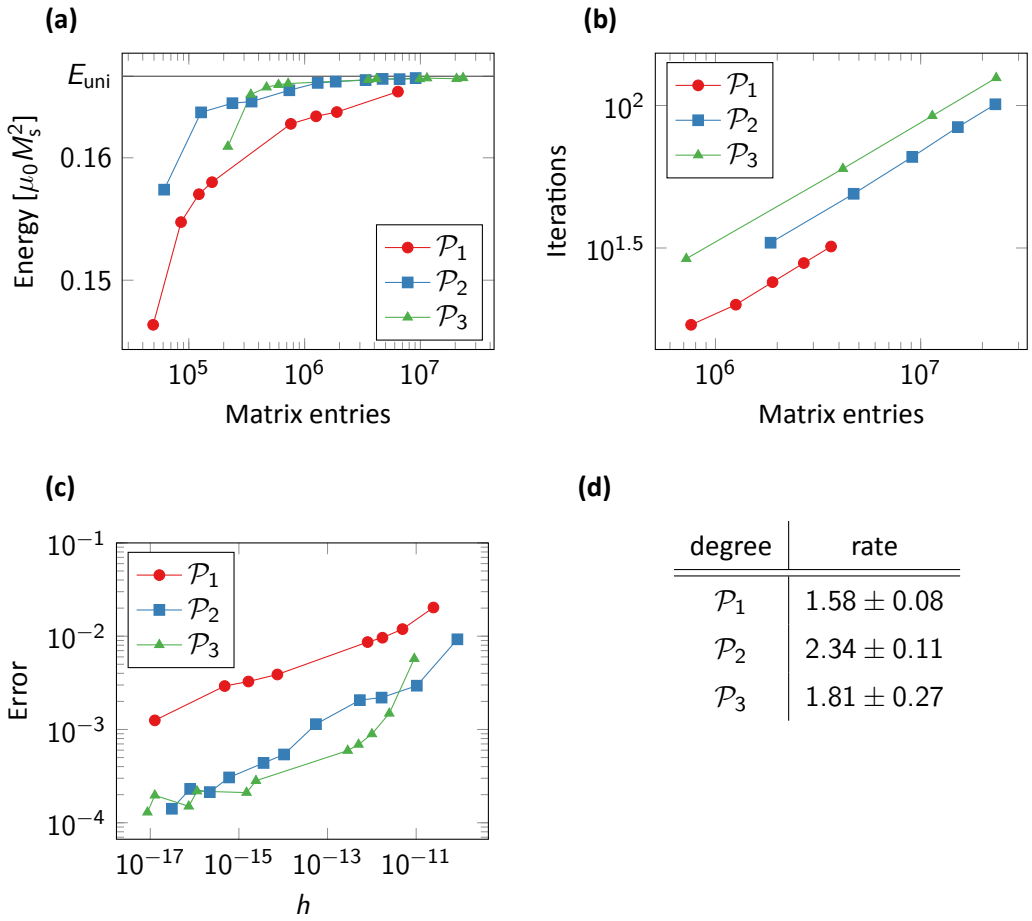

(d)

degree	rate
$\mathcal{P}_1$	1.58 ± 0.08
$\mathcal{P}_2$	2.34 ± 0.11
$\mathcal{P}_3$	1.81 ± 0.27

Figure 3.12: Numerical experiments with the cuboid shell-transformation method. **(a)** Energy calculations for a homogeneously magnetized cube with different polynomial degree. Matrix entries denotes the number of nonzero entries of the sparse system matrix. The analytical solution is denoted by E_{uni}. **(b)** Number of iterations of the conjugate-gradient solver for different polynomial degree. **(c)** Relative error of the energy δE for a uniformly magnetized cube. The mesh size h accounts for the auxiliary nodes introduced by higher-order methods. **(d)** Experimental convergence rates for different polynomial degree, computed from the results of plot (c). Modified from [64].

tions scale linearly with the number of matrix entries. Since the linear systems are solved with iterative solvers, the matrix–vector multiplication gives a good measure for the complexity of the solution of the system. The plot shows that the transformation method gains accuracy with higher polynomial order. Particularly the method of first order performs poorly compared to the higher-order methods. The reason is the additional $1/r'$ term that is present only in the higher-order methods as shown in Sec. 3.2.3. This term enables a much better approximation of the decaying potential u.

This qualitative difference between the first-order method and the higher-order methods is also found in the convergence behaviour, shown in Fig. 3.12c and Tab. 3.12d. The second and third-order method have a convergence rate of approximately 2 while the first-order method converges only with a rate of approximately 1.6. Furthermore the plot shows, that the error of the first-order method is an order of magnitude higher than for the higher-order methods for the same mesh size h. Note that the auxiliary mesh-nodes for the higher-order methods are taken into account for the computation of h.

The linear system arising from the weak formulation 3.2.31 is symmetric positive definite. Hence it is solved with the conjugate gradient method [59] as iterative solver. An algebraic multigrid preconditioner is used, which leads to a small number of iterations. Figure 3.12b shows the number of iterations for the methods of different polynomial degree. Linear fits yield a $N^{0.4}$ dependence of the iterations on the number of matrix entries N. A single iteration basically consists of a matrix–vector multiplication that has a computational complexity of $\mathcal{O}(N)$. This leads to an overall asymptotic complexity of $\mathcal{O}(N^{1.4})$.

Crouzeix-Raviart Elements

In [65] and [66] it is stated that the computation of the demagnetization potential u with conforming piecewise polynomial functions leads to unstable behaviour in the context of energy minimization. The authors propose the use of Crouzeix-Raviart elements for the discretization of u to stabilize the solution. Figure 3.13 shows the results for the demagnetization-potential calculation with Crouzeix-Raviart elements compared to the computation with standard Lagrange elements. Obviously the application of the transformation method with Crouzeix-Raviart elements leads to errors on the boundary of the sample. Using a simple truncation approach yields smoother results, however this method suffers from the bad approximation of the exterior space. For the dynamical computations carried out in this work, the conforming method did not yield any instabilities, see Sec. 4.3.4. Thus the conforming method is used throughout this work.

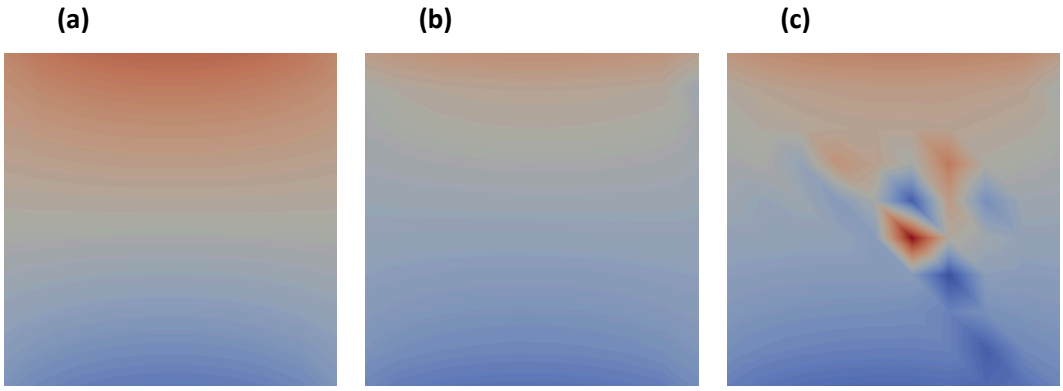

Figure 3.13: Demagnetization potential u of a homogeneously magnetized unit cube at one side, computed with different elements and methods. Red color marks positive values and blue color marks negative values. **(a)** Transformation method using conforming Lagrange elements of second order. **(b)** Truncation method using Crouzeix-Raviart elements of first order. **(c)** Transformation method using Crouzeix-Raviart elements of first order.

3.3 Comparison

This section is dedicated to the comparison of the demagnetization-field methods introduced in the preceding sections. The presented numerical experiments and the comparsion of the results for the presented methods are taken from [67]. Here, only the contributions of the author are described. For further details and the additional comparison to the tensor-grid methods developed by Lukas Exl, the reader is referred to this publication.

The relative errors in energy and field are computed for different geometries and magnetization configurations. Each computation is carried out with the previously described methods, namely with the demagnetization-tensor method (DM) introduced in Sec. 3.1, the scalar-potential method (SP) introduced in Sec. 3.1.3 and the finite-element method (FE) introduced in Sec. 3.2. If the analytical solution to a problem is not known, a reference solution is computed with the demagnetization-tensor method. The reference solution is computed on a refined mesh with quadruple resolution in every spatial dimension.

The methods are compared with regard to the total energy and the field. The relative field error is computed as

$$\delta \boldsymbol{H} = \sqrt{\frac{1}{N} \sum_i \left| \boldsymbol{H}^i_{\text{analytical}} - \boldsymbol{H}^i_{\text{numerical}} \right|^2} \tag{3.3.1}$$

where N denotes the total number of cells and $\boldsymbol{H}^i$ is the field value of cell i. Additionally the angular deviation of the computed field to the analytical field is given as average $\delta \boldsymbol{H}_{\text{ang}}$ and as maximum $\delta \boldsymbol{H}_{\text{angmax}}$. The field values for the finite-element solution are computed via projec-

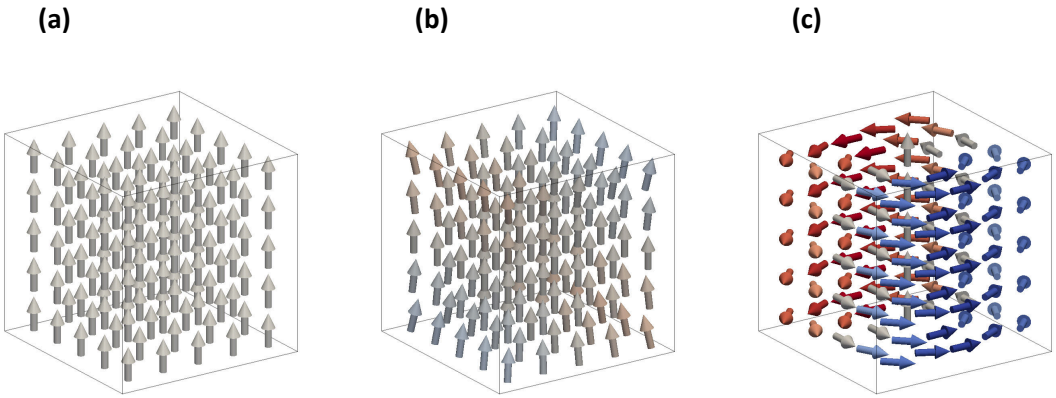

Figure 3.14: Magnetization configurations in a cube used for numerical experiments. **(a)** Homogeneous magnetization **(b)** Flower state **(c)** Vortex state. From [67].

Method	N	δE	$\delta \boldsymbol{H}$	$\delta \boldsymbol{H}_{\text{ang}}$ [°]	$\delta \boldsymbol{H}_{\text{angmax}}$ [°]
DM	$40 \times 40 \times 40$	$2.9 \cdot 10^{-9}$	0	0	0
SP	$40 \times 40 \times 40$	$1.1 \cdot 10^{-3}$	$1.1 \cdot 10^{-3}$	$2.3 \cdot 10^{-5}$	5.0
FE	$7.2 \cdot 10^{4}$	$8.6 \cdot 10^{-4}$	$2.2 \cdot 10^{-3}$	$3.2 \cdot 10^{-5}$	5.2

Table 3.1: Results of demagnetization-field computations for a uniformly magnetized unit cube. Modified from [67].

tion of the gradient

$$\int_{\Omega} \boldsymbol{H}_{\text{demag}} \cdot \boldsymbol{v} \, \mathrm{d}\boldsymbol{r} = -\int_{\Omega} \nabla u \cdot \boldsymbol{v} \, \mathrm{d}\boldsymbol{r} \; \forall \; \boldsymbol{v} \in V. \tag{3.3.2}$$

The solution of this projection is transferred to the regular cuboid grid used by the Fourier-space methods via a simple oversampling method.

Unit Cube Geometry

The demagnetization field for three different magnetization configurations in a unit cube is compared. The different configurations are depicted in Fig. 3.14. The first test is the uniformly magnetized unit cube that was already used in Sec. 3.2.4 for the validation of the finite-element algorithm. The configuration is depicted in Fig. 3.14a. The computational results are presented in Tab. 3.1 and Fig. 3.15a. The demagnetization-tensor method plays a special role for this test problem, since its discretization scheme assumes uniformly magnetized cuboid cells. Thus the energy and the field computed with the demagnetization-tensor method are exact even when discretizing with a single cell. Both the finite-element method and the scalar-potential method approach the energy from below, however, the latter converges faster. Deviations in the field computation are of the same order of magnitude.

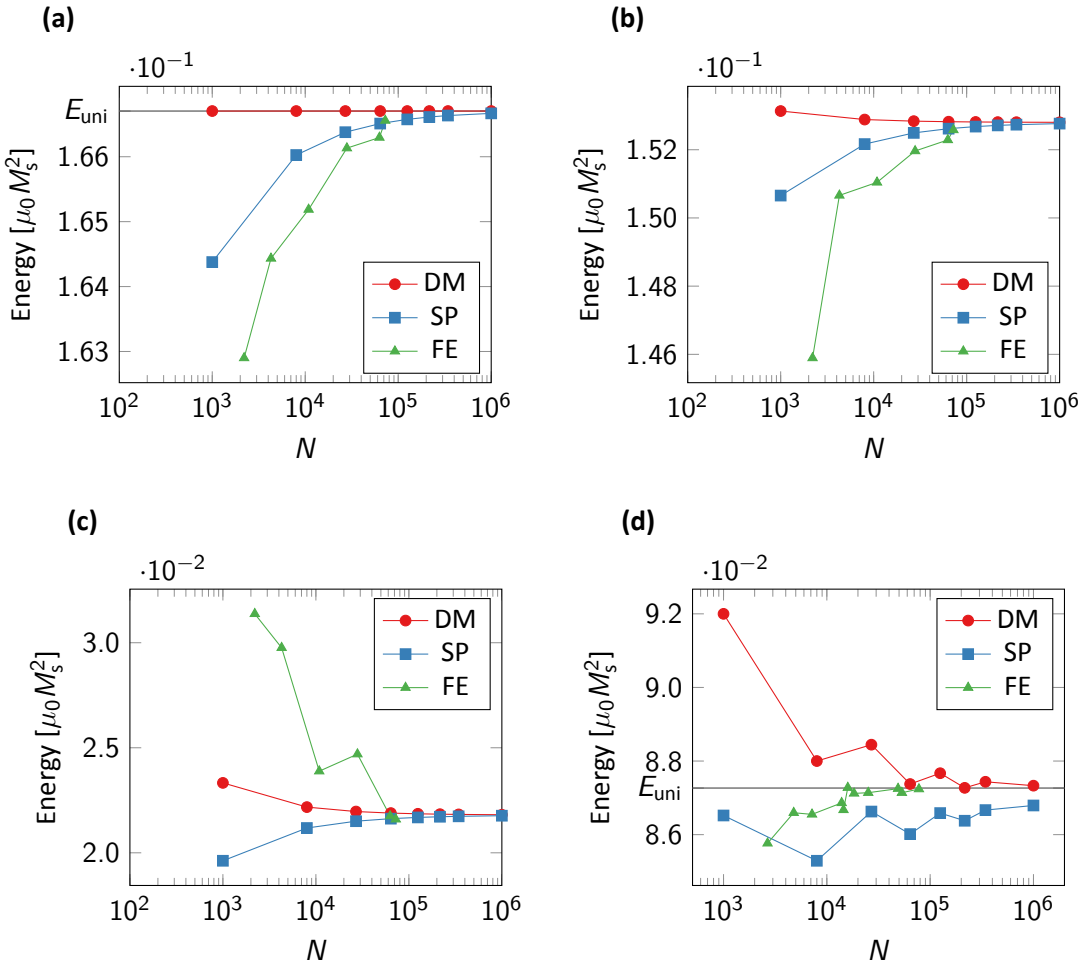

Figure 3.15: Energy calculations for different geometries and magnetization configurations. The energy for each configuration is computed with the demagnetization-tensor method (DM), the scalar-potential method (SP) and the finite-element method with shell transformation (FE). For the Fourier-space methods N denotes the number of simulation cells, for the finite-element method N denotes the number of degrees of freedom. **(a)** Uniformly magnetized unit cube. The analytical solution is denoted by E_{uni}. **(b)** Flower state in unit cube **(c)** Vortex state in unit cube **(d)** Uniformly magnetized sphere. The analytical solution is denoted by E_{uni}. Modified from [67].

Method	N	δE	$\delta \boldsymbol{H}$	$\delta \boldsymbol{H}_{\text{ang}}$ [°]	$\delta \boldsymbol{H}_{\text{angmax}}$ [°]
DM	$40 \times 40 \times 40$	$1.30 \cdot 10^{-4}$	$1.6 \cdot 10^{-5}$	$1.1 \cdot 10^{-9}$	$4.0 \cdot 10^{-2}$
SP	$40 \times 40 \times 40$	$1.20 \cdot 10^{-3}$	$1.8 \cdot 10^{-3}$	$5.0 \cdot 10^{-5}$	$7.2 \cdot 10^{+0}$
FE	$7.2 \cdot 10^{4}$	$1.47 \cdot 10^{-3}$	$2.5 \cdot 10^{-3}$	$6.1 \cdot 10^{-5}$	$6.8 \cdot 10^{+0}$

Table 3.2: Results of demagnetization-field computations for a flower state in a unit cube. Modified from [67].

Method	N	δE	$\delta \boldsymbol{H}$	$\delta \boldsymbol{H}_{\text{ang}}$ [°]	$\delta \boldsymbol{H}_{\text{angmax}}$ [°]
DM	$40 \times 40 \times 40$	$4.08 \cdot 10^{-3}$	$9.2 \cdot 10^{-4}$	$2.9 \cdot 10^{-4}$	$1.1 \cdot 10^{+1}$
SP	$40 \times 40 \times 40$	$8.08 \cdot 10^{-3}$	$2.3 \cdot 10^{-3}$	$2.1 \cdot 10^{-5}$	$3.4 \cdot 10^{+0}$
FE	$7.2 \cdot 10^{4}$	$9.44 \cdot 10^{-3}$	$2.1 \cdot 10^{-2}$	$6.1 \cdot 10^{-2}$	$1.8 \cdot 10^{+2}$

Table 3.3: Results of demagnetization-field computations for a vortex state in a unit cube. Modified from [67].

The second test problem is a so-called flower state, which is depicted in Fig. 3.14b. This magnetization configuration is a local minimum of the energy landscape of small cubic particles. The normalized version of the parametrization

$$\boldsymbol{m}(\boldsymbol{r}) = \begin{pmatrix} \frac{1}{a} r_1 r_3 \\ \frac{1}{c} r_2 r_3 + \frac{1}{b^3} r_2^3 r_3^3 \\ 1 \end{pmatrix} \tag{3.3.3}$$

is used for the numerical experiments with the center of the cube located at $(0, 0, 0)$. The parameters are chosen as $a = c = 1$ and $b = 2$. Results for the flower state are summarized in Tab. 3.2 and Fig. 3.15b. The results of the scalar-potential method and the finite-element method are similar to those of the uniformly magnetized cube. The demagnetization-tensor method shows the fastest convergence.

The third magnetization configuration defined on a unit cube is the so-called magnetic vortex, depicted in Fig. 3.14c. Like the flower state, the vortex state is a local energetical minimum for cubic particles of a certain size. The following parametrization is used for the numerical experiments

$$\boldsymbol{m}(\boldsymbol{r}) = \begin{pmatrix} -\frac{r_2}{r_{12}} \sqrt{1 - \exp\left(-4 \frac{r_{12}^2}{R_c^2}\right)} \\ \frac{r_1}{r_{12}} \sqrt{1 - \exp\left(-4 \frac{r_{12}^2}{R_c^2}\right)} \\ \exp\left(-2 \frac{r_{12}^2}{R_c^2}\right) \end{pmatrix} \tag{3.3.4}$$

with $r_{12} = \sqrt{r_1^2 + r_2^2}$ where the radius of the vortex core R_c is set to 0.14 for the numeical experiments. The results are shown in Tab. 3.3 and Fig. 3.15c. Again, the demagnetization-

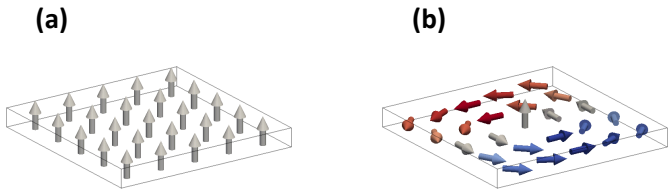

Figure 3.16: Magnetization configurations in a thin film used for numerical experiments. **(a)** Homogeneous magnetization **(b)** Vortex state. From [67].

Method	N	δE	$\delta \boldsymbol{H}$	$\delta \boldsymbol{H}_{\text{ang}}$ [°]	$\delta \boldsymbol{H}_{\text{angmax}}$ [°]
DM	$80 \times 80 \times 8$	$2.94 \cdot 10^{-6}$	0	0	0
SP	$80 \times 80 \times 8$	$1.02 \cdot 10^{-3}$	$1.7 \cdot 10^{-3}$	$2.6 \cdot 10^{-5}$	4.5
FE	$4.9 \cdot 10^{4}$	$1.05 \cdot 10^{-2}$	$5.5 \cdot 10^{-3}$	$1.9 \cdot 10^{-5}$	5.0

Table 3.4: Results of demagnetization-field computations for a homogeneous magnetization in a thin square. Modified from [67].

tensor method performs best, followed by the scalar-potential method and the finite-element method.

Thin Square Geometry

Since a broad number of applications of micromagnetism involve ferromagnetic thin films, a thin square of size $(1, 1, 0.1)$ is investigated. A homogeneous magnetization configuration as well as a vortex configuration are computed, see Fig. 3.16. The results are summarized in Tab. 3.4 and 3.5.

The most notable difference to the computations for the cubic geometry is the error of the finite-element method that is an order of magnitude higher than the error of the Fourier-space methods. The flat geometry has a high surface-to-volume ratio which leads to a large number of shell elements. Thus the computation is dominated by the simulation of the exterior space, which leads to larger errors within the sample when keeping the total number of elements constant.

Method	N	δE	$\delta \boldsymbol{H}$	$\delta \boldsymbol{H}_{\text{ang}}$ [°]	$\delta \boldsymbol{H}_{\text{angmax}}$ [°]
DM	$80 \times 80 \times 8$	$6.37 \cdot 10^{-4}$	$2.3 \cdot 10^{-4}$	$2.8 \cdot 10^{-6}$	$6.8 \cdot 10^{-1}$
SP	$80 \times 80 \times 8$	$8.47 \cdot 10^{-3}$	$2.5 \cdot 10^{-3}$	$4.6 \cdot 10^{-5}$	$3.6 \cdot 10^{+0}$
FE	$4.9 \cdot 10^{4}$	$4.59 \cdot 10^{-2}$	$6.1 \cdot 10^{-3}$	$6.6 \cdot 10^{-4}$	$2.1 \cdot 10^{+1}$

Table 3.5: Results of demagnetization-field computations for a vortex state in a thin square. Modified from [67].

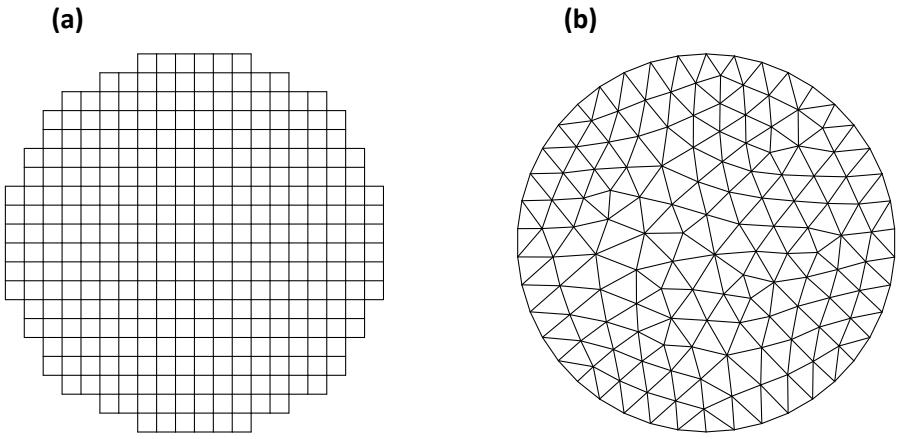

Figure 3.17: Discretization of a circle **(a)** with a regular cuboid grid **(b)** with an irregular mesh of triangles.

Spherical Geometry

The geometries featured in the preceding sections are perfectly approximated by both the regular cuboid meshes used by the Fourier-space methods and the tetrahedral meshes used by the finite-element method. Irregular tetrahedral meshes however are able to approximate curved geometries better than regular cuboid meshes, see Fig. 3.17. The finite-element method is thus expected to superseed the Fourier-space methods for curved geometries. As a test problem, demagnetization energy and field of a homogeneously magnetized sphere with radius $R = 0.5$ and $\boldsymbol{M} = (0, 0, 1)^T$ are computed. The sphere was approximated on the regular grid by testing the cell centers $\boldsymbol{r}_i$ against the sphere condition

$$\boldsymbol{M}_i = \begin{cases} (0,0,1)^T & \text{if } |\boldsymbol{r}_i| < R \\ 0 & \text{else} \end{cases} \tag{3.3.5}$$

where $\boldsymbol{M}_i$ is the magnetization in cell i. The irregular mesh used for the finite-element calculation was created such that the discrete volume coincides with the analytical volume $V = 4/3\pi R^3$.

In Fig. 3.15d the results of the energy calculations are presented. As expected the finite-element method converges faster than the Fourier-space methods. A comparison of the field computation is given in Fig. 3.18. On the regular grid, the field computation shows strong artifacts that obviously result from the bad approximation of the surface. The finite-element result on the other hand features a perfectly homogeneous demagnetization-field as predicted by theory.

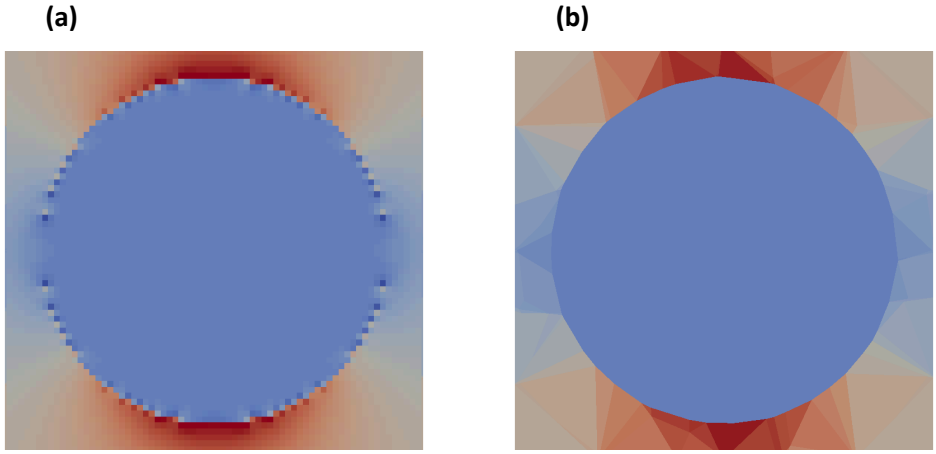

Figure 3.18: Demagnetization field of a uniformly magnetized sphere. The component H_3 is shown on the middle plane of the sphere. **(a)** Computed with the demagnetization-tensor method on a $50 \times 50 \times 50$ grid. **(b)** Computed with the finite-element method on a mesh of 9429 tetrahedra including the shell elements. From [67].

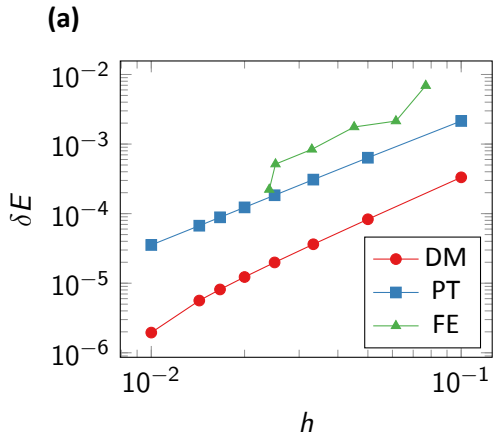

(b)

Method	Rate
DM	2.179 ± 0.065
SP	1.785 ± 0.004
FE	2.425 ± 0.343

Figure 3.19: Convergence comparison of the different demagnetization-field methods. **(a)** The relative error in the energy δE of a flower state in a unit cube is plotted against the cell size h. The auxiliary nodes from the third order finite-element method are taken into account for the determination of h. **(b)** Experimental convergence rates computed from the results of plot (a). Modified from [67].

3.3.1 Convergence

Figure 3.19 shows the convergence rates for the flower state in the unit cube as described in Sec. 3.3. Both the Fourier-space methods and the finite-element method feature a convergence rate of approximately 2.

3.3.2 Conclusion

Three different methods for the demagnetization-field computation were discussed in detail and compared to each other. The demagnetization-tensor method and the scalar-potential method compute the demagnetization-field by a fast-convolution technique. The scalar-potential method is faster than the demagnetization-tensor method by a factor of 1.5 and requires about 30% less memory, see [40], but it is also less accurate due to the additional numerical computation of the gradient.

In contrast to the Fourier-space methods, the finite-element method is able to handle irregular grids. This makes it a good choice for computations on curved geometries, which is confirmed by numerical experiments on a sphere.

However, due to the very efficient fast Fourier-transform algorithm, the demagnetization-tensor method and the scalar-potential method are still the better choice for cuboid domains.

CHAPTER 4

Time Integration of the Landau-Lifshitz-Gilbert Equation

The Landau-Lifshitz-Gilbert equation as introduced in Sec. 2.3 is a nonlinear differential equation that describes the motion of the magnetization field $\boldsymbol{m}(\boldsymbol{r})$ in an effective field $\boldsymbol{H}_{\text{eff}}(\boldsymbol{r})$. For a constant effective field, the Landau-Lifshitz-Gilbert equation is an ordinary differential equation in every point. However, the exchange field and the demagnetization field add a spatial coupling of the magnetization, see Sec. 2.3.3, and turn the ordinary differential equation into a partial differential equation in space and time.

This chapter is dedicated to the numerical solution of the Landau-Lifshitz-Gilbert equation. The challenge is to find an integration scheme that is both stable and efficient. Furthermore it is considered beneficial if the integration scheme conserves important properties of the Landau-Lifshitz-Gilbert equation, see Sec. 2.3.5.

In the following a brief overview of available integration methods is given and their suitability for micromagnetism is discussed. We distinguish between collocation methods, see Sec. 4.1, and weak methods, see Sec. 4.2 and 4.3. For a more detailed review on integration schemes for the Landau-Lifshitz-Gilbert equation, the reader is referred to the work by Cimrak [27].

A weak implicit scheme based on the work of Alouges [68] is described in greater detail in Sec. 4.3. This scheme is combined with the shell-transformation method for the demagnetization-field computation. Along with the description of this method, numerical tests for its validation are presented.

4.1 Collocation Methods

This section gives an overview of different collocation methods for the numerical integration. These methods solve the Landau-Lifshitz-Gilbert equation pointwise. For the finite-difference discretization scheme used in Sec. 3.1 these methods can be applied per simulation cell. For finite-element methods with Lagrange functions, the collocation methods are applied per mesh node.

4.1.1 Explicit Integration

The most basic explicit integration scheme is the so-called Euler method. Consider the time derivate of the magnetization at time t

$$\partial_t \boldsymbol{m} = \boldsymbol{f}(t, \boldsymbol{m}(t)) \tag{4.1.1}$$

and the initial value $\boldsymbol{m}_0 = \boldsymbol{m}(t_0)$. A single step of the Euler method is given by

$$\frac{\boldsymbol{m}^{k+1} - \boldsymbol{m}^k}{\tau} = \boldsymbol{f}(t_k, \boldsymbol{m}^k) \tag{4.1.2}$$

where $\boldsymbol{m}^k = \boldsymbol{m}(t_k)$ and $\tau = t_{k+1} - t_k$ is the step size. Thus from a given magnetization $\boldsymbol{m}^k$ the subsequent magnetization $\boldsymbol{m}^{k+1}$ is computed by

$$\boldsymbol{m}^{k+1} = \boldsymbol{m}^k + \tau \boldsymbol{f}(t_k, \boldsymbol{m}^k). \tag{4.1.3}$$

The magnetization at an arbitrary time $\boldsymbol{m}(t)$ is obtained by performing a number of integration steps starting from the known initial value $\boldsymbol{m}_0$. The Euler method is a first order method. It is usually very easy to implement since it is always linear in the solution $\boldsymbol{m}^{k+1}$ regardless of the form of the right-hand side $\boldsymbol{f}(t, \boldsymbol{m})$.

Explicit methods are usually applied to the explicit form of the Landau-Lifshitz-Gilbert equation as given by Eqn. 2.3.23

$$\partial_t \boldsymbol{m} = -\gamma'(\boldsymbol{m} \times \boldsymbol{H}_{\text{eff}}) - \alpha' \boldsymbol{m} \times (\boldsymbol{m} \times \boldsymbol{H}_{\text{eff}}). \tag{4.1.4}$$

which leads to a right-hand side $\boldsymbol{f}(t, \boldsymbol{m})$ of the form

$$\boldsymbol{f}(t, \boldsymbol{m}) = \boldsymbol{m} \times \boldsymbol{A}(t, \boldsymbol{m}). \tag{4.1.5}$$

In Sec. 2.3.5 it was shown that the Landau-Lifshitz-Gilbert equation preserves the modulus of the magnetization $\partial_t |\boldsymbol{m}| = 0$. This property is violated by the Euler method. Inserting

Eqn. 4.1.5 into Eqn. 4.1.2 and scalar multiplication with $\tau(\boldsymbol{m}^{k+1} + \boldsymbol{m}^k)$ yields

$$|\boldsymbol{m}^{k+1}|^2 - |\boldsymbol{m}^k|^2 = \tau[\boldsymbol{m}^k \times \boldsymbol{A}(t_k, \boldsymbol{m}^k)] \cdot (\boldsymbol{m}^{k+1} + \boldsymbol{m}^k) \tag{4.1.6}$$

$$= \tau[\boldsymbol{m}^k \times \boldsymbol{A}(t_k, \boldsymbol{m}^k)] \cdot (\boldsymbol{m}^{k+1} - \boldsymbol{m}^k) \tag{4.1.7}$$

$$= |\tau \boldsymbol{m}^k \times \boldsymbol{A}(t_k, \boldsymbol{m}^k)|^2 \tag{4.1.8}$$

$$\geq 0. \tag{4.1.9}$$

The modulus is only preserved if $\boldsymbol{m}^k \times \boldsymbol{A}(t_k, \boldsymbol{m}^k) = \boldsymbol{f}(t, \boldsymbol{m}^k) = 0$. This is the case for local energy minima only in which case $\boldsymbol{m}^k = \boldsymbol{m}^{k+1}$. Obviously Eqn. 4.1.9 implies a monotonically increasing modulus of $\boldsymbol{m}$, which leads to unrealistic solutions for long integration times. A common variation of the Euler method is the application of an additional normalization

$$\boldsymbol{m}^{k+1} = \frac{\boldsymbol{m}^k + \tau \boldsymbol{f}(t_k, \boldsymbol{m}^k)}{|\boldsymbol{m}^k + \tau \boldsymbol{f}(t_k, \boldsymbol{m}^k)|}. \tag{4.1.10}$$

However, due to its low order this method requires very small time steps in order to deliver accurate results. A more general scheme is given by the explicit Runge-Kutta method [69]. A single integration step of the Runge-Kutta method involves the evaluation of s intermediate results $\boldsymbol{k}_i$. The solution of a complete integration step $\boldsymbol{m}^{k+1}$ is given as a linear superposition of the intermediate results $\boldsymbol{k}_i$ by

$$\boldsymbol{m}^{k+1} = \boldsymbol{m}^k + \tau \sum_i^s b_i \boldsymbol{k}_i \tag{4.1.11}$$

$$\boldsymbol{k}_i = \boldsymbol{f}\left(t_k + \tau c_i,\ \boldsymbol{m}^k + \tau \sum_j^{i-1} a_{ij} \boldsymbol{k}_j\right) \tag{4.1.12}$$

where the coefficients a_{ij}, b_i and c_i are given by a so-called Butcher tableau [69] that specifies a particular Runge-Kutta method. The resulting method is of order s. Higher order methods usually allow for a larger time step without loss of accuracy. In practical applications the additional effort required for the computation of the intermediate results is often more than compensated by the larger time step. Due to its explicit nature the calculation of an intermediate result $\boldsymbol{k}_i$ does only depend on the results of previous results $\boldsymbol{k}_{j<i}$. Thus the Runge-Kutta method like the Euler method only involves problems linear in the intermediate solutions $\boldsymbol{k}_i$. In fact the Euler method is a special case of the Runge-Kutta method.

Runge-Kutta methods can be used with a fixed time step like the Euler method. However, a common practice is the adaptive step-size control. The error of an integration step of order n is estimated by a computation of order $n + 1$. The step size is then adapted such that the error remains in certain error bounds. Examples for adaptive Runge-Kutta methods are the Runge-Kutta-Fehlberg method [70] and the Cash-Karp method [71].

Explicit methods turn out to deliver good results for many applications in the framework of finite-difference discretization [72]. However, the time step τ has to be scaled with the quadratic

mesh size h^2 in order to keep the time integration scheme stable [73]. For irregular meshes as used in the finite-element framework, h is derived from the smallest cell. This often leads to impractically small time steps. Another difficulty is the stiffness of the problem under consideration, see [73]. It is a well known fact that implicit methods are unconditionally stable and outperform explicit algorithms regarding the solution of stiff problems [74].

4.1.2 Implicit Integration

The implicit counterpart of the Euler method is the so-called backward Euler defined by

$$\frac{\boldsymbol{m}^{k+1} - \boldsymbol{m}^k}{\tau} = \boldsymbol{f}(t_k + \tau, \boldsymbol{m}^{k+1}). \tag{4.1.13}$$

Depending on the form of the right-hand side $\boldsymbol{f}(t, \boldsymbol{m})$, the computation of a single integration step can be very costly. In the case of micromagnetics the right-hand side is at least quadratic in $\boldsymbol{m}$, see Eqn. 4.1.4. The resulting equations are usually solved with an iterative Newton method.

Like the explicit Euler method, the backward Euler suffers from the violation of the preservation of modulus. By a similar procedure as shown in Eqn. 4.1.9 one obtains

$$|\boldsymbol{m}^{k+1}|^2 - |\boldsymbol{m}^k|^2 \leq 0. \tag{4.1.14}$$

In contrast to the explicit method, here the modulus is always decreased. The same normalization procedure as in Eqn. 4.1.10 can be used in order to preserve the modulus of the magnetization. An alternative approach is the reduction from $3N$ values for the representation of the magnetization to $2N$ as proposed in [75]. This approach reduces the size of the nonlinear problem. The third component of the magnetization is reconstructed after each step by the normalization condition $|\boldsymbol{m}| = 1$.

4.1.3 Midpoint Scheme

A collocation scheme that turns out to be very suitable for micromagnetics is the so-called midpoint rule given by

$$\frac{\boldsymbol{m}^{k+1} - \boldsymbol{m}^k}{\tau} = \boldsymbol{f}(t_k + \tau/2, \boldsymbol{m}^{k+1/2}) \tag{4.1.15}$$

where the magnetization at the midpoint is defined as $\boldsymbol{m}^{k+1/2} = (\boldsymbol{m}^{k+1} + \boldsymbol{m}^k)/2$. Consider again the general form of the Landau-Lifshitz-Gilbert equation

$$\boldsymbol{f}(t, \boldsymbol{m}) = \boldsymbol{m} \times \boldsymbol{A}(t, \boldsymbol{m}) \tag{4.1.16}$$

as introduced in Eqn. 4.1.5. Inserting into Eqn. 4.1.15 and multiplication with $\boldsymbol{m}^{k+1/2}$ yields

$$|\boldsymbol{m}^{k+1}|^2 - |\boldsymbol{m}^k|^2 = 2\tau \boldsymbol{m}^{k+1/2} \cdot \left[\boldsymbol{m}^{k+1/2} \times \boldsymbol{A}\left(t_k + \tau/2, \boldsymbol{m}^{k+1/2}\right)\right] = 0. \tag{4.1.17}$$

The midpoint method naturally preserves the modulus of the magnetization. Moreover, this method also preserves the Liapunov structure of the Landau-Lifshitz-Gilbert equation for a finite damping $\alpha > 0$ and the Hamiltonian structure for vanishing damping $\alpha = 0$, see Sec. 2.3.5. The proof of these properties along with detailed numerical investigations of the midpoint method is given in [26].

As mentioned in [27] there are no analytical convergence results for any of the above described collocation methods. However, collocation methods are successfully applied and deliver reliable results for many real world problems.

4.2 Weak Method by Bartels and Prohl

If the finite-element method is used for spatial discretization, then a natural choice for the time-integration is a method that does also rely on the finite-element method. An implicit method that solves the Landau-Lifshitz-Gilbert equation in a weak sense was introduced by Bartels and Prohl in [76]. The method is based on the implicit form of the Landau-Lifshitz-Gilbert equation given by Eqn. 2.3.17. A time step is performed by seeking for the next magnetization configuration $\boldsymbol{m}_h^{k+1}$ given by

$$\left(\delta \boldsymbol{m}_h^{k+1}, \phi_h\right)_h + \alpha \left(\boldsymbol{m}_h^k \times \delta \boldsymbol{m}_h^{k+1}, \phi_h\right)_h = \gamma \left(\boldsymbol{m}_h^{k+1/2} \times \boldsymbol{H}_{\text{eff}}\left[t + \tau/2, \boldsymbol{m}_h^{k+1/2}\right], \phi_h\right)_h \;\forall\, \phi_h \in \boldsymbol{V}_h \quad (4.2.1)$$

where $\boldsymbol{m}_h^k$ and $\boldsymbol{m}_h^{k+1}$ are elements of the discrete finite-element function space $\boldsymbol{V}_h$. Furthermore $\boldsymbol{m}_h^{k+1/2}$ and $\delta \boldsymbol{m}_h^{k+1}$ are defined as

$$\boldsymbol{m}_h^{k+1/2} = \frac{\boldsymbol{m}_h^{k+1} + \boldsymbol{m}_h^k}{2} \quad (4.2.2)$$

$$\delta \boldsymbol{m}_h^{k+1} = \frac{\boldsymbol{m}_h^{k+1} - \boldsymbol{m}_h^k}{\tau} \quad (4.2.3)$$

and $(\cdot, \cdot)_h$ denotes the reduced L_2 scalar product

$$(\boldsymbol{a}, \boldsymbol{b})_h = \int_\Omega \mathcal{I}_h(\langle \boldsymbol{a}, \boldsymbol{b} \rangle)\, \mathrm{d}\boldsymbol{r} \quad (4.2.4)$$

where $\mathcal{I}_h$ is the nodal interpolation operator on V_h. The second term of the left-hand side of Eqn. 4.2.1 is motivated by the equality

$$\left(\boldsymbol{m}_h^k \times \delta \boldsymbol{m}_h^{k+1}, \phi_h\right)_h = \left(\boldsymbol{m}_h^{k+1/2} \times \delta \boldsymbol{m}_h^{k+1}, \phi_h\right)_h. \quad (4.2.5)$$

The underlying construction principle is a midpoint scheme similar to Eqn. 4.1.15. Thus the modulus of the magnetization is preserved at least on the nodes of the finite-element mesh.

Convergence analysis and numerical experiments for the case of the exchange field being the only effective-field contribution are given in [76]. Like for the midpoint-collocation method, a nonlinear system of equations has to be solved for every time step.

4.3 Weak Method by Alouges

Another weak formulation of the Landau-Lifshitz-Gilbert equation was proposed by Alouges in [68]. The proposed scheme is a two-step method. In a first step the time derivative of the magnetization $\partial_t \boldsymbol{m}$ is computed. A weak formulation of this problem is obtained by multiplying the implicit form of the Landau-Lifshitz-Gilbert equation 2.3.17 with test functions ϕ

$$\int_\Omega (\boldsymbol{v} - \alpha \boldsymbol{m} \times \boldsymbol{v}) \cdot \phi \, \mathrm{d}\boldsymbol{r} + \int_\Omega \gamma (\boldsymbol{m} \times \boldsymbol{H}_{\text{eff}}) \cdot \phi \, \mathrm{d}\boldsymbol{r} = 0 \; \forall \; \phi \in \boldsymbol{V}. \tag{4.3.1}$$

where the solution $\boldsymbol{v}$ of this system solves for $\partial_t \boldsymbol{m}$ in a weak sense. The individual terms of the Landau-Lifshitz-Gilbert equation are pointwise perpendicular to the magnetization $\boldsymbol{m}$. For the terms $\boldsymbol{m} \times \boldsymbol{v}$ and $\boldsymbol{m} \times \boldsymbol{H}_{\text{eff}}$ this follows from the properties of the cross product. As a sum of the latter terms this does also hold for the solution $\boldsymbol{v}$. Thus it is sufficient to test Eqn. 4.3.1 with functions from the tangent space $\mathcal{T}_m$ defined by

$$\mathcal{T}_m = \{\boldsymbol{x} \in \boldsymbol{H}^1(\Omega); \boldsymbol{x} \cdot \boldsymbol{m} = 0\}. \tag{4.3.2}$$

Instead of testing with ϕ directly it is hence possible to test with $\boldsymbol{m} \times \boldsymbol{w} \in \mathcal{T}_m$ where $\boldsymbol{w}$ are the new test functions. While the cross-product terms $\boldsymbol{m} \times \boldsymbol{v}$ and $\boldsymbol{m} \times \boldsymbol{H}_{\text{eff}}$ always fulfill the tangent-space constraint by definition, the solution $\boldsymbol{v}$ does not. Hence the restriction of test functions to the tangent space $\mathcal{T}_m$ requires the explicit restriction of the solution $\boldsymbol{v}$ to $\mathcal{T}_m$. An equivalent formulation of Eqn. 4.3.1 is thus given by seeking a solution $\boldsymbol{v} \in \mathcal{T}_m$ that fulfills

$$\int_\Omega \underbrace{\boldsymbol{v} \cdot (\boldsymbol{m} \times \boldsymbol{w})}_{\text{I}} \, \mathrm{d}\boldsymbol{r} - \alpha \int_\Omega \underbrace{(\boldsymbol{m} \times \boldsymbol{v}) \cdot (\boldsymbol{m} \times \boldsymbol{w})}_{\text{II}} \, \mathrm{d}\boldsymbol{r} + \gamma \int_\Omega \underbrace{(\boldsymbol{m} \times \boldsymbol{H}_{\text{eff}}(\boldsymbol{m})) \cdot (\boldsymbol{m} \times \boldsymbol{w})}_{\text{III}} \, \mathrm{d}\boldsymbol{r} = 0 \; \forall \; \boldsymbol{w} \in \boldsymbol{V}. \tag{4.3.3}$$

This formulation can be significantly simplified by application of vector identities and the properties of the magnetization $|\boldsymbol{m}| = 1$ and $\boldsymbol{m} \cdot \boldsymbol{v} = 0$. The individual terms read

$$\text{I)} \quad \boldsymbol{v} \cdot (\boldsymbol{m} \times \boldsymbol{w}) = -\boldsymbol{w} \cdot (\boldsymbol{m} \times \boldsymbol{v}) \tag{4.3.4}$$

$$\text{II)} \quad (\boldsymbol{m} \times \boldsymbol{v}) \cdot (\boldsymbol{m} \times \boldsymbol{w}) = \boldsymbol{v} \cdot \boldsymbol{w} \tag{4.3.5}$$

$$\text{III)} \quad (\boldsymbol{m} \times \boldsymbol{H}_{\text{eff}}) \cdot (\boldsymbol{m} \times \boldsymbol{w}) = \boldsymbol{H}_{\text{eff}} \cdot \boldsymbol{w} - (\boldsymbol{m} \cdot \boldsymbol{w})(\boldsymbol{H}_{\text{eff}} \cdot \boldsymbol{m}). \tag{4.3.6}$$

The system is further simplified by restricting the test funtions $\boldsymbol{w}$ to the tangent space $\mathcal{T}_m$. This does not affect the validity of Eqn. 4.3.3 since the cross product $\boldsymbol{m} \times \boldsymbol{w}$ cancels the non-tangential part of $\boldsymbol{w}$ in any case. With the restriction of $\boldsymbol{w} \in \mathcal{T}_m$ the second term on the right-hand side of Eqn. 4.3.6 vanishes. The problem of finding $\boldsymbol{v} = \partial_t \boldsymbol{m}$ is reduced to seeking $\boldsymbol{v} \in \mathcal{T}_m$ given by

$$\int_\Omega (\alpha \boldsymbol{v} + \boldsymbol{m} \times \boldsymbol{v}) \cdot \boldsymbol{w} \, \mathrm{d}\boldsymbol{r} - \gamma \int_\Omega \boldsymbol{H}_{\text{eff}}(\boldsymbol{m}) \cdot \boldsymbol{w} \, \mathrm{d}\boldsymbol{r} = 0 \; \forall \; \boldsymbol{w} \in \mathcal{T}_m. \tag{4.3.7}$$

The most notable difference between Eqn. 4.3.7 and Eqn. 4.3.1 is the term including the effective field. In Eqn. 4.3.7 this term depends on the magnetization only through the effective field in contrast to Eqn. 4.3.1.

The solution $\boldsymbol{v}$ can be used to construct an explicit integration scheme. After discretization a single time step is carried out by

$$\boldsymbol{m}_i^{k+1} = \frac{\boldsymbol{m}_i^k + \tau \boldsymbol{v}_i}{|\boldsymbol{m}_i^k + \tau \boldsymbol{v}_i|} \tag{4.3.8}$$

where τ is the time step and $\boldsymbol{m}_i$ and $\boldsymbol{v}_i$ denote the corresponding field values at computation node i [77]. Note that due to the normalization, this scheme preserves the modulus of the magnetization node-wise. Obviously it is not possible to preserve the norm everywhere due to the choice of discrete function space. However, this explicit scheme can be simply converted into an implicit theta-scheme by replacing $\boldsymbol{m}$ by $\boldsymbol{m} + \theta\tau\boldsymbol{v}$ in Eqn. 4.3.7. The weak formulation then reads

$$\int_\Omega (\alpha \boldsymbol{v} + \boldsymbol{m} \times \boldsymbol{v}) \cdot \boldsymbol{w} \, \mathrm{d}\boldsymbol{r} - \gamma \int_\Omega \boldsymbol{H}_{\text{eff}}(\boldsymbol{m} + \theta\tau\boldsymbol{v}) \cdot \boldsymbol{w} \, \mathrm{d}\boldsymbol{r} = 0 \; \forall \; \boldsymbol{w} \in \mathcal{T}_m \tag{4.3.9}$$

with $\theta \in [0, 1]$. The advantage of the presented scheme over the weak formulation in Eqn. 4.3.1 is revealed when taking the exchange field, given by Eqn. 2.3.27, as effective field. Inserting Eqn. 2.3.27 in Eqn. 4.3.9 and performing integration by parts yields

$$\int_\Omega (\alpha \boldsymbol{v} + \boldsymbol{m} \times \boldsymbol{v}) \cdot \boldsymbol{w} \, \mathrm{d}\boldsymbol{r} + \frac{2\gamma A}{\mu_0 M_\mathrm{s}} \int_\Omega \boldsymbol{\nabla}(\boldsymbol{m} + \theta\tau\boldsymbol{v}) \boldsymbol{\nabla} \boldsymbol{w} \, \mathrm{d}\boldsymbol{r} = 0 \; \forall \; \boldsymbol{w} \in \mathcal{T}_m \tag{4.3.10}$$

where the exchange boundary condition from Eqn. 2.3.35 was taken into account, which leads to a vanishing boundary integral. Since the exchange field is linear in the magnetization, the resulting integration scheme is linear in the solution $\boldsymbol{v}$ and implicit. Adding nonlinear contributions to the effective field, e.g. higher-order anisotropy terms, obviously breaks the linearity of the scheme. But even the inclusion of the linear demagnetization field leads to problems, because the computation of the dense linear operator is often avoided by variational computation of the connected Poisson problem, see Sec. 3.2.

Thus it was proposed in [78, 79] to treat only the exchange contribution implicitly. This method is justified by the fact that the exchange contribution has the highest order due to its second spatial derivative and is the main cause for the stiffness of the problem. This results in the weak formulation

$$\begin{aligned} \int_\Omega (\alpha \boldsymbol{v} + \boldsymbol{m} \times \boldsymbol{v}) \cdot \boldsymbol{w} \, \mathrm{d}\boldsymbol{r} + \frac{2\gamma A}{\mu_0 M_\mathrm{s}} \int_\Omega \boldsymbol{\nabla}(\boldsymbol{m} + \theta\tau\boldsymbol{v}) \boldsymbol{\nabla} \boldsymbol{w} \, \mathrm{d}\boldsymbol{r} \\ - \gamma \int_\Omega \boldsymbol{H}_{\text{expl}}(\boldsymbol{m}) \cdot \boldsymbol{w} \, \mathrm{d}\boldsymbol{r} = 0 \; \forall \; \boldsymbol{w} \in \mathcal{T}_m \end{aligned} \tag{4.3.11}$$

where $\boldsymbol{H}_{\text{expl}}$ includes all contributions to the effective field except the exchange field.

4.3.1 Discretization

The discretization of Eqn. 4.3.10 is done component-wise with Lagrange functions of first order, resulting in the discrete vector-function space $\boldsymbol{V}_h$. A challenge specific to the method proposed by Alouges is the restriction of test functions and solution to the tangential space $\mathcal{T}_m$. In general it is not possible to construct a subspace $\boldsymbol{V}_h \subset \mathcal{T}_m$. Thus the tangent-space restriction has to be relaxed. This can either be done by requiring this restriction on the computation nodes or in an integral sense. The actual implementation of the restrictions is done with a Lagrange-multiplier ansatz as suggested in [78]. Consider the following short-hand notation of the original problem defined on the tangent space

$$a(\boldsymbol{v}, \boldsymbol{w}) = L(\boldsymbol{w}) \;\forall\; \boldsymbol{w} \in \mathcal{T}_m \text{ with } \boldsymbol{v} \in \mathcal{T}_m \tag{4.3.12}$$

where $a(\boldsymbol{v}, \boldsymbol{w})$ is a bilinear form and $L(\boldsymbol{w})$ is a linear form given by

$$a(\boldsymbol{v}, \boldsymbol{w}) = \int_\Omega (\alpha \boldsymbol{v} + \boldsymbol{m} \times \boldsymbol{v}) \cdot \boldsymbol{w} \, \mathrm{d}\boldsymbol{r} + \frac{2\gamma A \theta \tau}{\mu_0 M_s} \int_\Omega \boldsymbol{\nabla v} \boldsymbol{\nabla w} \, \mathrm{d}\boldsymbol{r} \tag{4.3.13}$$

$$L(\boldsymbol{w}) = -\frac{2\gamma A}{\mu_0 M_s} \int_\Omega \boldsymbol{\nabla m} \boldsymbol{\nabla w} \, \mathrm{d}\boldsymbol{r} + \gamma \int_\Omega \boldsymbol{H}_{\text{expl}}(\boldsymbol{m}) \cdot \boldsymbol{w} \, \mathrm{d}\boldsymbol{r}. \tag{4.3.14}$$

Applying the Lagrange-multipier ansatz yields the system

$$a(\boldsymbol{v}, \boldsymbol{w}) + \int_\Omega \lambda \, \boldsymbol{m} \cdot \boldsymbol{w} \, \mathrm{d}\boldsymbol{r} = L(\boldsymbol{w}) \qquad \forall\; \boldsymbol{w} \in \boldsymbol{V}_h \tag{4.3.15}$$

$$\int_\Omega \boldsymbol{v} \cdot \boldsymbol{m} \, \sigma \, \mathrm{d}\boldsymbol{r} = 0 \qquad \forall\; \sigma \in V_h \tag{4.3.16}$$

Here the solution is explicitly restricted to the tangent space in an integral sense by Eqn. 4.3.16. The Lagrange multiplier field in Eqn. 4.3.15 is crucial to relieve the tangent-space constraint on the test functions. This formulation leads to the following block system of equations

$$\begin{pmatrix} A & B^T \\ B & 0 \end{pmatrix} \begin{pmatrix} v \\ \lambda \end{pmatrix} = \begin{pmatrix} b \\ 0 \end{pmatrix} \tag{4.3.17}$$

which is a saddle-point problem. The $3N \times 3N$ matrix A results from discretization of the bilinear form $a(\boldsymbol{v}, \boldsymbol{w})$ and the vector b results from discretization of the linear form $L(\boldsymbol{w})$. The $3N \times N$ matrix B and its transpose arise from discretization of the constraint in Eqn. 4.3.16 and the Lagrange-multiplier term in Eqn. 4.3.15.

An alternative Lagrange-multiplier approach applies the tangent-space restriction exactly on the computation nodes. In this case the integrals in Eqn. 4.3.15 and Eqn. 4.3.16 are replaced by node-wise computations

$$a(\boldsymbol{v}_i, \boldsymbol{w}_j) + \lambda_i \, \boldsymbol{m}_j \cdot \boldsymbol{w}_j = L(\boldsymbol{w}_j) \qquad \forall\; j \in \{1, 2, \dots, N\} \tag{4.3.18}$$

$$\boldsymbol{v}_k \cdot \boldsymbol{m}_k \, \sigma_l = 0 \qquad \forall\; l \in \{1, 2, \dots, N\} \tag{4.3.19}$$

where f_x denotes the value of a function f at node x, e.g. $\boldsymbol{m}_j$ denotes the value of the magnetization $\boldsymbol{m}$ at node j. The resulting block system has the same structure as Eqn. 4.3.17. However, the off-diagonal blocks have only contributions of degrees of freedom belonging to the same computation node. Hence $B^T B$ is diagonal.

Unique Solution

Consider the splitting of the bilinear form $a = b + c$ into a symmetric form $b(\boldsymbol{v}, \boldsymbol{w})$ and a skew-symmetric form $c(\boldsymbol{v}, \boldsymbol{w})$

$$b(\boldsymbol{v}, \boldsymbol{w}) = \alpha \int_\Omega \boldsymbol{v} \cdot \boldsymbol{w} \, \mathrm{d}\boldsymbol{r} + \frac{2\gamma A \theta \tau}{\mu_0 M_s} \int_\Omega \nabla \boldsymbol{v} \nabla \boldsymbol{w} \, \mathrm{d}\boldsymbol{r} \tag{4.3.20}$$

$$c(\boldsymbol{v}, \boldsymbol{w}) = \int_\Omega \boldsymbol{m} \times \boldsymbol{v} \cdot \boldsymbol{w} \, \mathrm{d}\boldsymbol{r}. \tag{4.3.21}$$

The symmetric form b consists of a mass and a stiffness contribution, both scaled with positive constants. Thus b is positive definite and so is the matrix A. Furthermore, the matrix B has full rank. In the case of a node-wise constraint this is directly given due to the nonzero magnetization $|\boldsymbol{m}| > 0$. For a weak constraint the magnetization additionally has to be sufficiently smooth.

The block matrix is singular if and only if there exists a nonzero vector $(x, y)^T$ that solves

$$\begin{pmatrix} A & B^T \\ B & 0 \end{pmatrix} \begin{pmatrix} x \\ y \end{pmatrix} = \begin{pmatrix} 0 \\ 0 \end{pmatrix} \tag{4.3.22}$$

or equivalently

$$Ax + B^T y = 0 \tag{4.3.23}$$

$$Bx = 0. \tag{4.3.24}$$

Equation 4.3.24 immediately yields $x \in \ker B$. If there exists a nonzero x that fulfills Eqn. 4.3.23 then it also has to fulfill

$$x^T A x + x^T B^T y = 0. \tag{4.3.25}$$

The second term vanishes since $x^T B^T = 0$ by the choice of $x \in \ker B$. Since A is positive definite, as shown above, it follows $x = 0$. Inserting into Eqn. 4.3.23 yields $B^T y = 0$ which results in $y = 0$ due to the full rank of B. Hence the block matrix is invertible and Eqn. 4.3.17 has a unique solution.

4.3.2 Implicit Integration of the Demagnetization Field

The numerical stability of the method presented in the preceding section can be further improved by treating the demagnetization field implicitly. Application of the shell-tansformation

method according to Eqn. 3.2.31 for the implicit demagnetization-potential computation yields

$$\int_{\Omega_{\text{cuboid}}} \nabla u \cdot \nabla w_1 \, \mathrm{d}\boldsymbol{r} + \int_{\Omega_{\text{shell}}} (\nabla u)^T \boldsymbol{g} \, \nabla w_1 \, \mathrm{d}\boldsymbol{r} = M_s \int_{\Omega_{\text{sample}}} (\boldsymbol{m} + \theta\tau \boldsymbol{v}) \cdot \nabla w_1 \, \mathrm{d}\boldsymbol{r} \; \forall \; w_1 \in V \quad (4.3.26)$$

where the right-hand side is now coupled to the solution $\boldsymbol{v}$ in contrast to the explicit computation. Vice versa the solution $\boldsymbol{v}$ of Eqn. 4.3.11 is coupled to the potential u by the effective-field term. This bidirectional coupling together with the Lagrange multiplier ansatz discussed in the previous chapter leads to the block system

$$\begin{pmatrix} A & B^T & 0 \\ B & 0 & D \\ 0 & E & C \end{pmatrix} \begin{pmatrix} v \\ \lambda \\ u \end{pmatrix} = \begin{pmatrix} b \\ 0 \\ c \end{pmatrix}. \quad (4.3.27)$$

Here the matrices A, B and the vector b are the same as introduced in Eqn. 4.3.17. The matrix C is the modified stiffness matrix arising from discretization of the left-hand side of Eqn. 4.3.26. The off-diagonal matrices D and E arise from the coupling integrals

$$-\gamma \int_{\Omega} \boldsymbol{\nabla} u \cdot \boldsymbol{w} \, \mathrm{d}\boldsymbol{r} \quad (4.3.28)$$

and

$$\theta\tau M_s \int_{\Omega_{\text{sample}}} \boldsymbol{v} \cdot \nabla w_1 \, \mathrm{d}\boldsymbol{r} \quad (4.3.29)$$

respectively. Finally the vector c is given by the explicit right-hand side of the demagnetization-field problem

$$M_s \int_{\Omega_{\text{sample}}} \boldsymbol{m} \cdot \nabla w_1 \, \mathrm{d}\boldsymbol{r}. \quad (4.3.30)$$

4.3.3 Numerical Treatment

Since the linear system given by Eqn. 4.3.27 is sparse, an iterative solver is favored over a direct solver. However, the system is indefinite and asymmetric which forbids the use of the fast conjugate-gradient method. Methods capable of solving such systems are the generalized minimal residual method (GMRES) developed by Saad, see [59], and the biconjugate gradient stabilized method (BICGSTAB) developed by van der Vorst et al., see [80]. It shows, however, that ignoring the block structure and applying an iterative method to the system as a whole leads to bad convergence behaviour.

Thus a Schur-complement ansatz with block preconditioning for the subsystems is applied.

$$Cz = c \quad (4.3.31)$$

$$S \begin{pmatrix} v \\ \lambda \end{pmatrix} = \begin{pmatrix} b \\ 0 \end{pmatrix} - \begin{pmatrix} D \\ 0 \end{pmatrix} z \quad (4.3.32)$$

where S is the Schur complement of the block C defined by

$$S = \begin{pmatrix} A & B^T \\ B & 0 \end{pmatrix} - \begin{pmatrix} D \\ 0 \end{pmatrix} C^{-1} \begin{pmatrix} E & 0 \end{pmatrix} = \begin{pmatrix} A - DC^{-1}E & B^T \\ B & 0 \end{pmatrix}. \tag{4.3.33}$$

Equation 4.3.31 is exactly the demagnetization problem as introduced in Sec. 3.2.3. Thus it is efficiently solved by a preconditioned conjugate-gradient method. Equation 4.3.32 is the saddle-point problem introduced in Eqn. 4.3.17 complemented by couling terms of the demagnetization potential. Thus this problem is also indefinite and asymmetric. A BICGSTAB method for the solution of this saddle-point problem is used. For the preconditioning consider the following decomposition of the original block problem 4.3.17

$$\begin{pmatrix} A & B^T \\ B & 0 \end{pmatrix} = \begin{pmatrix} \mathbb{1} & 0 \\ BA^{-1} & \mathbb{1} \end{pmatrix} \begin{pmatrix} A & B^T \\ 0 & -BA^{-1}B^T \end{pmatrix}. \tag{4.3.34}$$

Due to the identity blocks on the diagonal, the iterative solver is expected to converge faster for the first matrix on the right-hand side than for the original matrix on the left-hand side. Since the Schur complement S in Eqn. 4.3.32 differs from the original saddle-point problem only in a coupling term, the second matrix of the right-hand side of Eqn. 4.3.34 is considered to be a suitable preconditioner. Instead of the original problem $\mathcal{A}x = b$ the preconditioned problem

$$\mathcal{A}\mathcal{P}^{-1}y = b \tag{4.3.35}$$

$$x = \mathcal{P}^{-1}y \tag{4.3.36}$$

is solved, where $\mathcal{P}$ is given by an approximate inverse

$$\mathcal{P}^{-1} \approx \begin{pmatrix} A & B^T \\ 0 & -BA^{-1}B^T \end{pmatrix}^{-1}. \tag{4.3.37}$$

The coupling term in the $1,1$-block of Eqn. 4.3.33 contains the inverse of the demagnetization matrix C. This inverse is not computed explicitly, but solved iteratively for every iteration of the outer iterative solver. This combination of Schur complement and block preconditioning proved both reliable and efficient for a variety of problems.

4.3.4 Validation and Numerical Experiments

The presented algorithm is validated with different numerical tests. The first test is taken from the original publication of Alouges [68]. In order to make the results comparable to those published in [68], the following dimensionless system is solved with the method described in the preceding sections

$$\int_\Omega (\alpha \boldsymbol{v} - \boldsymbol{m} \times \boldsymbol{v}) \cdot \boldsymbol{w} \, \mathrm{d}\boldsymbol{r} = -(1+\alpha^2) \int_\Omega \boldsymbol{\nabla}(\boldsymbol{m} + \theta\tau\boldsymbol{v}) \boldsymbol{\nabla} \boldsymbol{w} \, \mathrm{d}\boldsymbol{r}. \tag{4.3.38}$$

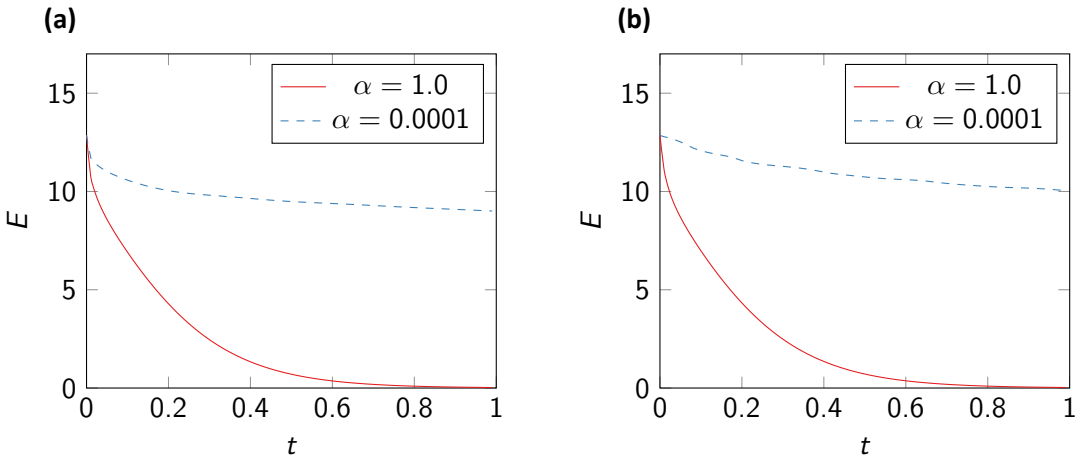

Figure 4.1: Total energy of an exchange coupled system with different damping. **(a)** For a backward Euler-like scheme ($\theta = 1$). **(b)** For a Crank-Nicholson-like scheme ($\theta = 0.5$).

Note the missing material parameters and the changed sign on the left-hand side which leads to a reversed direction of precession. The initial value for the magnetization is given by the parameterization

$$\boldsymbol{m}(\boldsymbol{r}) = \begin{pmatrix} -\frac{r_2}{r_{12}} \sin\left(\frac{\pi r_{12}}{2}\right) \\ \frac{r_1}{r_{12}} \sin\left(\frac{\pi r_{12}}{2}\right) \\ \cos\left(\frac{\pi r_{12}}{2}\right) \end{pmatrix} \tag{4.3.39}$$

with $r_{12} = \sqrt{r_1^2 + r_2^2}$. The time evolution of the total energy of this nonphysical but mathematically equivalent system is computed with a backward Euler-like scheme ($\theta = 1$) and with a Crank-Nicholson-like scheme ($\theta = 0.5$). Figure 4.1 shows the results of the computation that are in good agreement to the results presented in [68]. As expected the energy decreases faster with a higher damping α. For a low damping the Crank-Nicholson scheme shows a lower diffusion than the backward Euler which is also expected as shown in [68].

In a next test the computation of the time derivative of the magnetization $\boldsymbol{v} = \partial_t \boldsymbol{m}$ for an exchange coupled system is compared to the analytical solution. The geometry used for this test is a cuboid of size $2 \times 2 \times 0.2$ µm with material parameters chosen similar to permalloy, i.e.

$$A = 1.3 \cdot 10^{-11}\,\text{J/m} \tag{4.3.40}$$

$$M_s = 8.0 \cdot 10^{5}\,\text{A/m} \tag{4.3.41}$$

$$K_1 = K_2 = 0. \tag{4.3.42}$$

Further the damping constant was chosen as $\alpha = 0.02$ and the gyromagnetic ratio as $\gamma = 2.211 \cdot 10^5$ m/As. The vector $\boldsymbol{v}$ is computed once for a magnetization configuration defined by

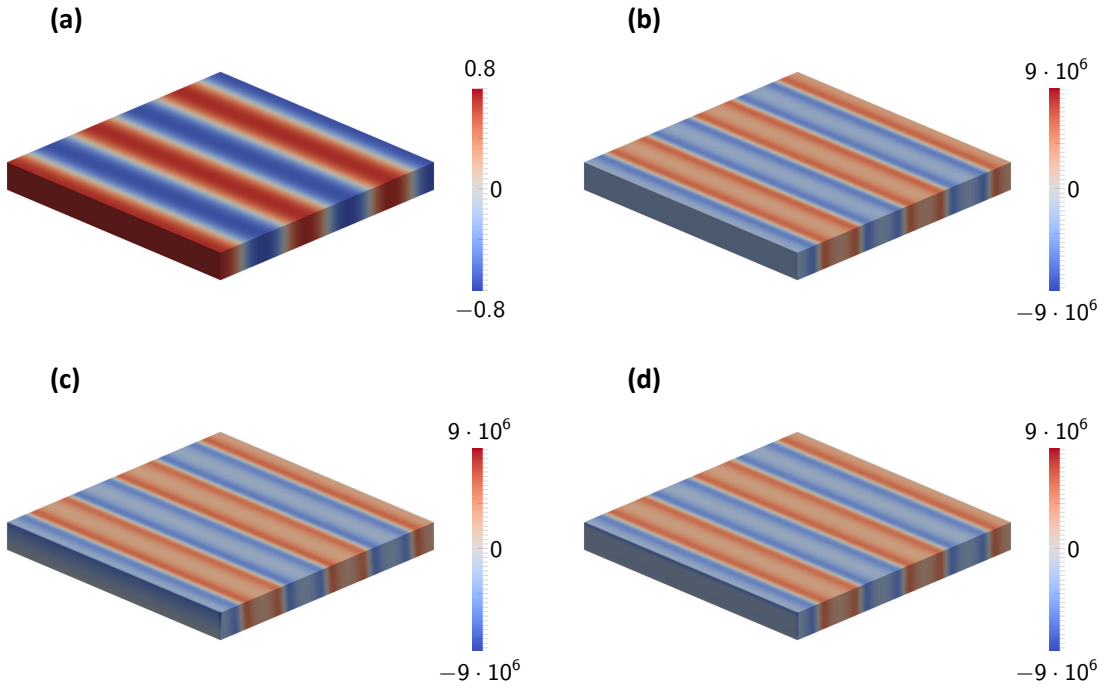

Figure 4.2: Validation problem for the computation of the time derivative of the magnetization $\boldsymbol{v}(\boldsymbol{m})$. **(a)** r_1-component of the magnetization configuration $\boldsymbol{m}$. **(b)** Analytical solution of the time derivative $\boldsymbol{v}$. **(c)** Numerical solution of $\boldsymbol{v}$, computed with node-wise tangent-space constraint and a single-layer spatial discretization. **(d)** Numerical solution of $\boldsymbol{v}$, computed with node-wise tangent-space constraint and a spatial discretization with 5 layers.

the normalized version of

$$\boldsymbol{m}(\boldsymbol{r}) = \begin{pmatrix} \sin(2.5 \cdot 10^6 \pi r_1) \\ 1 \\ 0 \end{pmatrix} \tag{4.3.43}$$

where the center of the cuboid geometry coincides with the coordinate origin $(0, 0, 0)$.

In order to compare the solution to the analytical result $\partial_t \boldsymbol{m}(t, \boldsymbol{m})$ the parameter θ was chosen as zero which corresponds to an explicit scheme and thus solves for time derivative at time t instead of time $t + \tau$. The magnetization configuration $\boldsymbol{m}$ and the analytical solution of $\boldsymbol{v}$ as well as the solution computed with node-wise constraints according to Eqn. 4.3.18 and 4.3.19 are depicted in Fig. 4.2. A comparison of the solution computed with weak constraints and node-wise constraints is presented in Fig. 4.3. It shows not only a very good agreement between analytical and numerical solution, but also a good agreement of the solutions computed with weak constraints and with node-wise constraints. Deviations of the numerical solutions occur especially at the boundaries. Figure 4.4 shows the deviations of analytical and numerical solutions at the sample boundaries. Obviously the errors can be significantly reduced by

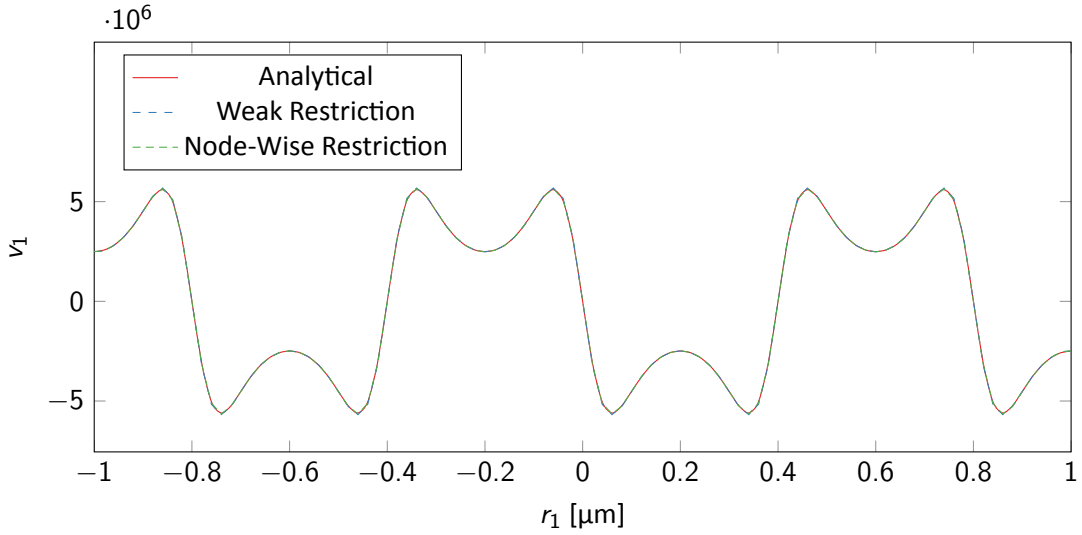

Figure 4.3: The r_1-component of the time derivative of the magnetization on the r_1 axis $v_1(r_1, 0, 0)$. The analytical solution is compared to the numerical solution with weak tangent-space restriction and node-wise tangent-space restriction.

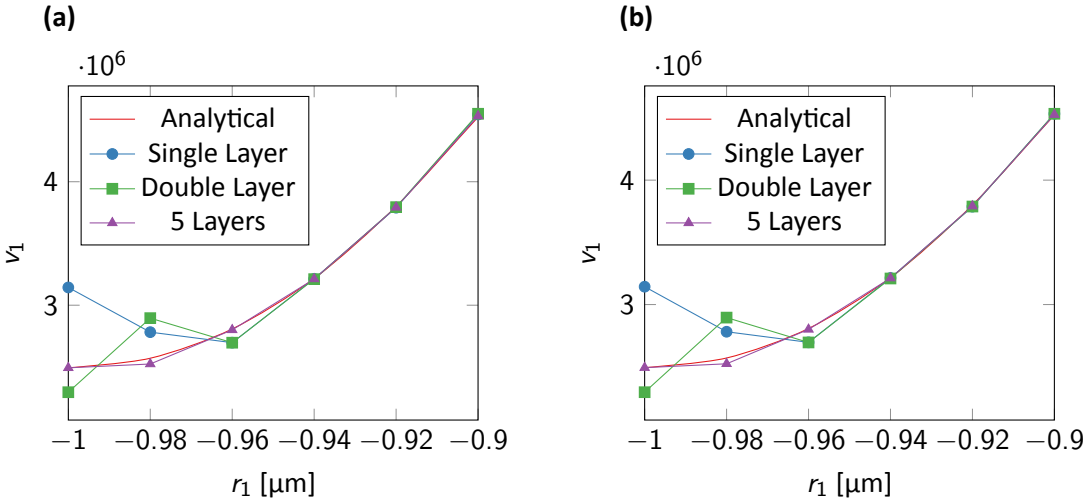

Figure 4.4: The r_1-component of the time derivative of the magnetization on the r_1-axis $v_1(r_1, 0, 0)$ at the boundary of the magnetized region. The computation was performed with a different number of simulation cells in the r_3-direction. **(a)** Weak tangent-space constraint. **(a)** Node-wise tangent-space constraint.

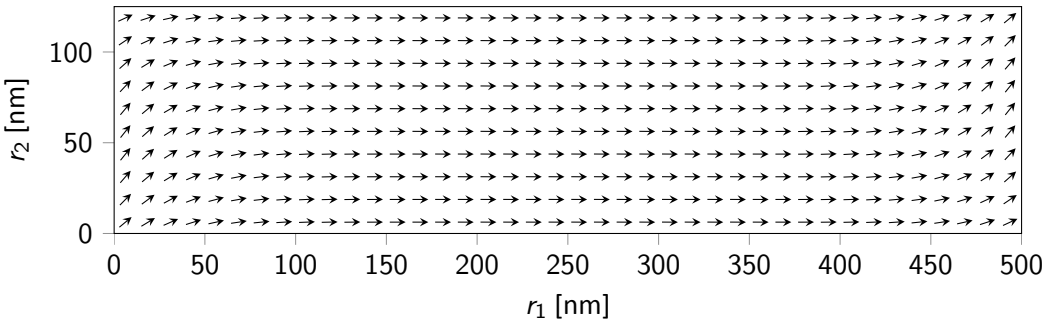

Figure 4.5: In-plane magnetization of a magnetic s-state on the middle plane of a thin film. The out-of-plane magnetization for this configuration is approximately zero. Modified from [64].

finer discretization. The errors at the boundaries can be explained by the violation of the exchange boundary condition Eqn. 2.3.35. Although the chosen magnetization parameterization Eqn. 4.3.43 analytically fulfills the boundary condition, the discretized magnetization in general does not.

µMag Standard Problem #4

The validation of the time stepping as well as the coupling to the demagnetization field is done via the µMAG standard problem #4, see [81]. It describes the switching process of a magnetic thin-film element under the influence of an external Zeeman field. This problem was designed as validation problem and as such it is sensitive to all vital parts of dynamical micromagnetics. Another reason for the choice of the standard problem #4 as validation problem is the availability of a large number of reference solutions.

A magnetic cuboid with size $500 \times 125 \times 3\,\mathrm{nm}$ and the material parameters of permalloy, see Eqns. 4.3.40–4.3.42, is considered. The problem itself consist of two parts. In a first step the magnetic region is relaxed in a specific local energy minimum called s-state. This is achieved by performing a time integration with the following start value for the magnetization

$$\boldsymbol{m}(\boldsymbol{r}) = \begin{pmatrix} \cos\left(\left|\pi r_1 \cdot 10^{-3}\right|\right) \\ \sin\left(\left|\pi r_1 \cdot 10^{-3}\right|\right) \\ 0 \end{pmatrix}. \tag{4.3.44}$$

The resulting s-state is pictured in Fig. 4.5. In a second step an external Zeeman field $\boldsymbol{H}_{\text{zeeman}}$ with a magnitude of $25\,\mathrm{mT}$ is applied with an angle of 170° to the sample

$$\boldsymbol{H}_{\text{zeeman}} = 25 \begin{pmatrix} \cos(170^\circ) \\ \sin(170^\circ) \\ 0 \end{pmatrix} \mathrm{mT}. \tag{4.3.45}$$

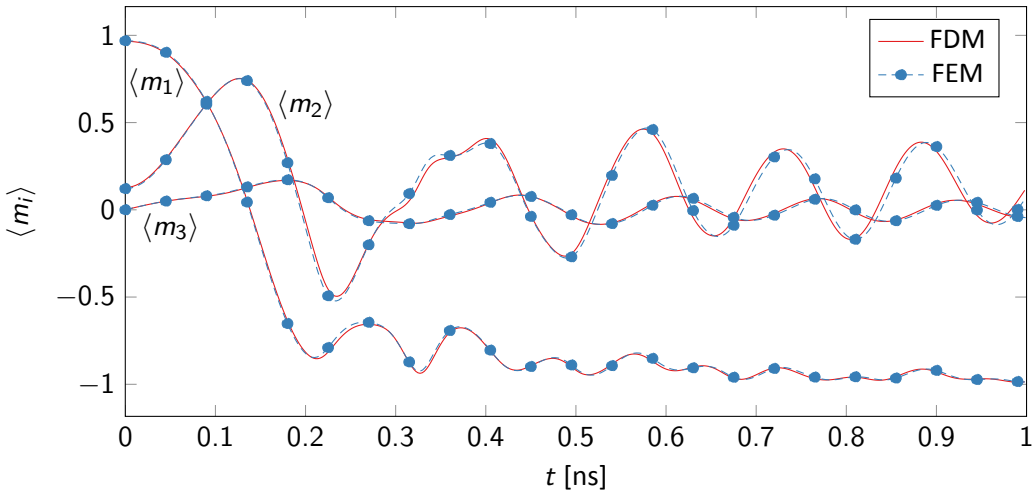

Figure 4.6: The time evolution of the averaged magnetization components $\langle m_i \rangle$ for the standard problem #4. The results of the finite-element (FEM) method are compared to results from the well tested finite-difference simulation code MicroMagnum (FDM). Modified from [64].

For this part of the problem the previously calculated s-state is taken as initial magnetization. Since the external field is directed opposite to the predominant magnetization direction, a switching process is initiated. Figure 4.6 shows the simulation results for this switching process in comparison to a reference result calculated with the finite-difference code MicroMagnum [82]. Obviously the reference solution is well reproduced by the methods presented in the preceding sections.

CHAPTER 5

Implementation

The implementation of a simulation program for the solution of dynamical micromagnetic problems is a challenging task. On the one hand, a complete dynamical code has to solve several subproblems, which naturally results in a high number of potential error sources. On the other hand an efficient micromagnetic code should be both fast and capable of handling large problems. To achieve this goal the code should be highly optimized for the problem at hand and high performance programming techniques such as parallel computing should be used.

This chapter is dedicated to the implementation of micromagnetic codes. Section 5.1 gives an overview over existing codes. In Sec. 5.2 the micromagnetic finite-element code magnum.fe is presented.

5.1 Existing Codes

The available codes can be roughly divided into finite-difference codes and finite-element codes. A very popular and established open-source finite-difference code is OOMMF [83]. Like almost all finite-difference codes it uses a Fourier space method as introduced in Sec. 3.1 for the computation of the demagnetization field. The exchange field is computed with finite differences as described in [72] and the time integration is done with explicit Runge-Kutta methods, see Sec. 4.1.1. In recent years the use of graphics processing units for highly parallel computations has gained much attention in the scientific computing community. The open-source codes MicroMagnum [82] and MuMax [84] implement similar methods to OOMMF and are able to perform the simulations entirely on graphics processing units. A closed-source code of this category is GPMagnet [36]. These codes provide a significant speedup compared to OOMMF, which performs all computations on the central processing unit. Further finite-difference codes include M^3S [85], NMag finite difference [86] and Yamms [87] which is described in detail in [88].

Available open-source finite-element codes include magpar [89] and NMag [90]. Closed-source

```
# Set up the bilinear form for the demagnetization problem
a = Dx(v, i) * Dx(u, i)           * dx(0) # Omega_sample
a+= Dx(v, i) * Dx(u, i)           * dx(1) # Omega_air
a+= Dx(v, i) * g1[i,j] * Dx(u, j) * dx(2) # Omega_shell, r_1 halfplane
a+= Dx(v, i) * g2[i,j] * Dx(u, j) * dx(3) # Omega_shell, r_2 halfplane
a+= Dx(v, i) * g3[i,j] * Dx(u, j) * dx(4) # Omega_shell, r_3 halfplane

# Create Dirichlet boundary conditions
bc = DirichletBC(VS, Constant(0.0), DomainBoundary())

# Assemble system matrix and apply boundary conditions
A = assemble(a)
bc.apply(A)
```

Listing 5.1: Weak form of the demagnetization-field problem as described in Sec. 3.2.3. In order to handle the cuboid shell properly, the volume integral is split up into integrals over different subdomains (`dx(0)` – `dx(4)`). The indices `i` and `j` are used to define vector–vector and matrix–vector products.

finite-element codes are FEMME [91] and TetraMag [92]. The latter also makes use of graphics processing units. To the knowledge of the author, these codes use the finite-element boundary-element coupling described in Sec. 3.2.2 for the demagnetization-field computation and implicit collocation methods for the integration of the Landau-Lifshitz-Gilbert equation as described in Sec. 4.1.2.

A micromagnetic code that implements the weak formulation introduced in Sec. 4.3 is FELL-GOOD [79]. For the demagnetization-field computation this code uses a nonuniform fast-Fourier-transform method.

5.2 magnum.fe

An integral part of the work presented in this thesis was the development of magnum.fe, a finite-element micromagnetic simulation tool, see [64]. magnum.fe implements the transformation method for the demagnetization-field computation introduced in Sec. 3.2.3 and the weak method for the integration of the Landau-Lifshitz-Gilbert equation introduced in Sec. 4.3. The code is based on the recently published finite-element package FEniCS [93] and uses Gmsh [94] for mesh creation.

FEniCS is written in C++ and features a Python scripting interface. The core component of FEniCS is the so-called form compiler FFC [95]. This form compiler produces efficient C++ code for the assembly of system matrices. It takes the description of a weak form in the unified form language UFL [96] and produces assembly code that conforms to the unified form-assembly

```
# Set up mixed function space
VV = VectorFunctionSpace(mesh, "CG", 1) # Solution
VS = FunctionSpace(mesh, "CG", 1)       # Lagrange Multipliers
V  = VV * VS

# Set up test and trial functions
(v, lamb)  = TrialFunctions(V)
(w, sigma) = TestFunctions(V)

# Prefactor for exchange field
f_ex = (- 2.0 * Aex * gamma) / (mu0 * ms)

# Set up bilinear form
a  = alpha * dot(v, w)           * dx \
   +         dot(cross(m, v), w) * dx \
   + sigma * inner(m, v)         * dx \
   + lamb  * inner(m, w)         * dx \
   - 0.5 * dt * f_ex * Dx(v[i],j) * Dx(w[i],j) * dx

# Set up linear form
L  = f_ex * Dx(m[i],j) * Dx(w[i],j) * dx
```

Listing 5.2: Weak form of the Landau-Lifshitz-Gilbert equation according to the method described in Sec. 4.3. A mixed function space is used to implement the Lagrange-multiplier ansatz. The constraints are fulfilled in a weak sense.

code UFC [97]. Sample codes for the weak forms of the demagnetization-field problem and the Landau-Lifshitz-Gilbert equation are given in Listing 5.1 and 5.2 respectively. FEniCS provides a just-in-time compiler that enables the compilation of form-assembly code at runtime. Further bindings for a couple of established open-source linear-algebra libraries are provided. Thus the entire problem definition and solution with FEniCS can be done in Python without suffering from the usually poor performance of interpreted languages.

Beside the Python interface, FEniCS also provides an almost equivalent C++ interface. In fact the Python interface is just a thin wrapping layer generated with the Simplified Wrapper and Interface Generator (SWIG) [98]. Nonetheless the Python interface is much simpler to use while adding only a small overhead. Hence magnum.fe uses the Python interface where possible. However, the algorithms used by magnum.fe require some functionality that is not provided by FEniCS. Extending FEniCS at the level of the Python interface will usually lead to performance issues when dealing with large problem sizes. The performance relevant extensions to FEniCS are therefore written in C++. Like FEniCS, magnum.fe uses SWIG to exploit the functionality of the C++ code to the Python interface. The dependencies of the different modules in both Python and C++ are visualized in Fig. 5.1. In the following the most important extensions to FEniCS are presented in detail.

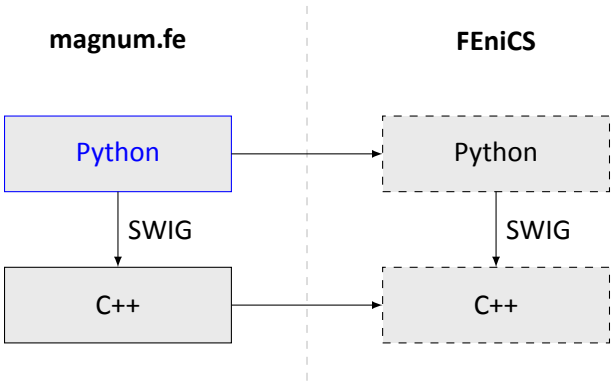

Figure 5.1: Dependencies between magnum.fe and FEniCS. Both magnum.fe and FEniCS have a C++ module whose functionality is exposed to the Python code via SWIG. Furthermore the C++ component of magnum.fe depends on the C++ component of FEniCS and the Python module of magnum.fe depends on the Python module of FEniCS.

5.2.1 Mesh Generation

The application of the cuboid shell-transformation method as described in Sec. 3.2.3 requires a mesh that properly represents the different regions Ω_{sample}, Ω_{air} and Ω_{shell}. Furthermore the cuboid shell is divided into six shell patches. The planar interfaces between the cuboid shell patches and the region Ω_{air} can be perfectly approximated by tetrahedra. Thus the mesh is required to accurately separate these regions. The meshing routine of magnum.fe is written in C++ and uses libGmsh [94]. The resulting meshing data is used to create a mesh object that is compatible with FEniCS.

Usually the user provides a mesh of the sample. The meshing routine of magnum.fe is able to read a variety of mesh formats and to create the required shell regions of the mesh. Figure 5.2 shows an example mesh for a spherical sample. Note that the cuboid shell patches are meshed in a regular fashion. The number of layers in the shell patches is configurable. This parameter is vital in order to control the quality of the demagnetization-field approximation.

5.2.2 Node-Wise Operations

FEniCS supports a great variety of finite elements. Beside the standard Lagrange elements in H^1 a number of elements in $H(\text{div})$ as well as in $H(\text{rot})$ is supported. As a consequence the interface of FEniCS exhibits a very abstract notion of degrees of freedom. When dealing with standard Lagrange elements, this means that there is no simple way to get a mapping between nodes and degrees of freedom although such mapping exists in theory. Moreover FEniCS does not provide a method to identify the degrees of freedom belonging to the same node when using component-wise Lagrange vector functions. This is particularly problematic for the im-

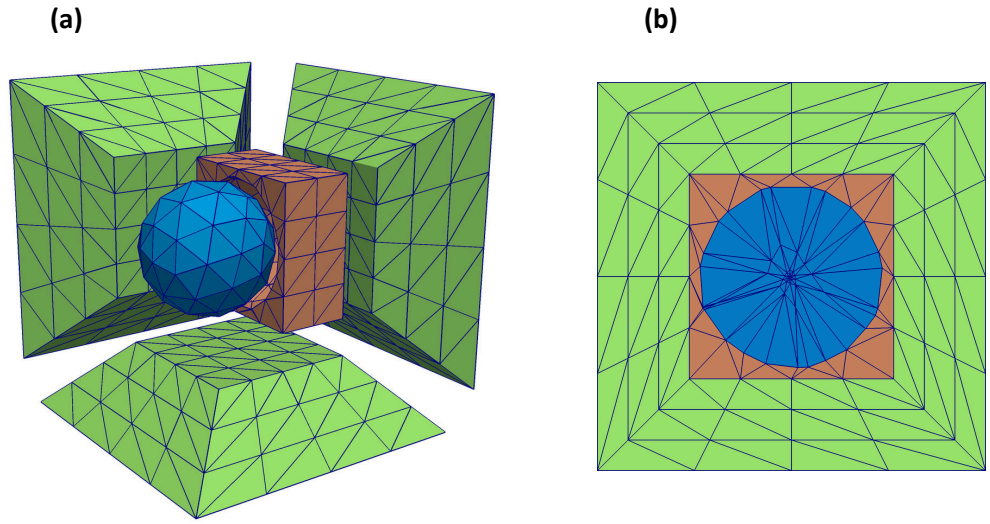

Figure 5.2: The mesh of a spherical sample surrounded by a cuboid shell as required by the cuboid shell-transformation method for the computation of the demagnetization field. The different regions are marked by colors: Ω_{sample} (blue), Ω_{air} (orange), Ω_{shell} (green). **(a)** Explosion view of the different regions. **(b)** Cut through the composite mesh. Modified from [64].

```
# Set up function space and function
V      = VectorFunctionSpace(mesh, "CG", 1)
m      = interpolate(some_expression, V)

# Compute node-wise normalized m
m_norm = DofAssembler.assemble(NormalizedVector(V, m))
```

Listing 5.3: Example usage of the `DofAssembler` class to perform node-wise normalization of the function `m`.

plementation of the integration scheme introduction in Sec. 4.3 since this scheme requires the node-wise renormalization of the magnetization after each time step.

In the style of the `Assembler` class in FEniCS which handles the assembly of matrices and vectors, magnum.fe introduces the `DofAssembler` class. This class offers an `assemble` method that is able to create matrices and vectors from instances of the `DofForm` class. By subclassing `DofForm`, node-wise operations may be implemented. The fact that the local numbering of degrees of freedom per cell is constant is used to express the node-wise operations per cell. The `DofAssembler` class uses the same level of abstraction as the original `Assembler` class. Thus it fully supports different linear algebra backends and parallelization features.

5.2.3 Conclusion

The micromagnetic code magnum.fe implements different finite-element methods for the solution of dynamical micromagnetic problems. Due to the use of the high-level finite-element package FEniCS, the code is both very readable and extendable. Performance relevant extensions to the FEniCS library were implemented in C++ and make use of the existing abstraction layers where possible. magnum.fe is open-source, well documented and available for download at [99].

CHAPTER 6

A Physical Example

As a physical example, the domain-wall structure of a tail-to-tail wall in a magnetic nanorod is investigated. The material parameters of the nanorods are chosen to be similar to those of permalloy, see Eqns. 4.3.40–4.3.42, and the diameter of the rod is varied between 10 nm and 50 nm. The initial magnetization is chosen as an infinitely thin tail-to-tail wall. The resulting discrete representation reads

$$\boldsymbol{m}_i = \operatorname{sgn}(r_{3,i}) \begin{pmatrix} 0 \\ 0 \\ 1 \end{pmatrix} \tag{6.0.1}$$

where the cylindrical axis of the rod is chosen parallel to the r_3-axis and the center of the rod coincides with the coordinate origin $(0, 0, 0)$. Figure 6.1 shows the tetrahedral mesh that was created with Gmsh [94]. For the sake of comparability the same mesh is used for all different rod diameters and scaled accordingly. The length of the rod is chosen to be 10 times the diameter, which is much larger than the expected width of the domain wall. The high length guarantees a low influence of surface effects at the rod faces on the domain wall, which is located in the center of the rod.

The initial state is relaxed into an energetical minimum by computation of the time evolution with a high damping $\alpha = 1$. As discussed in [100] the domain-wall in a ferromagnetic rod is expected to be of transverse type for small diameters, see Fig. 6.2a and 6.3a, and of vortex type

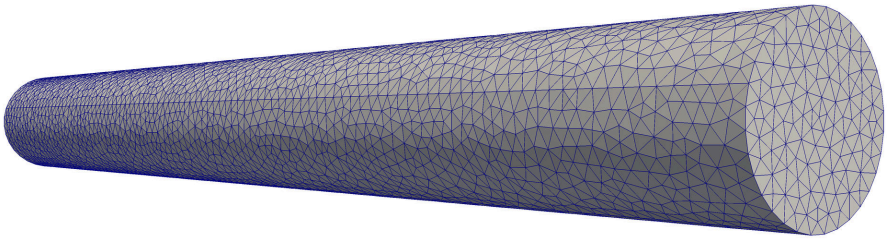

Figure 6.1: Tetrahedral mesh used for the discretization of the nanorods. The mesh consists of 7275 nodes and 39344 cells.

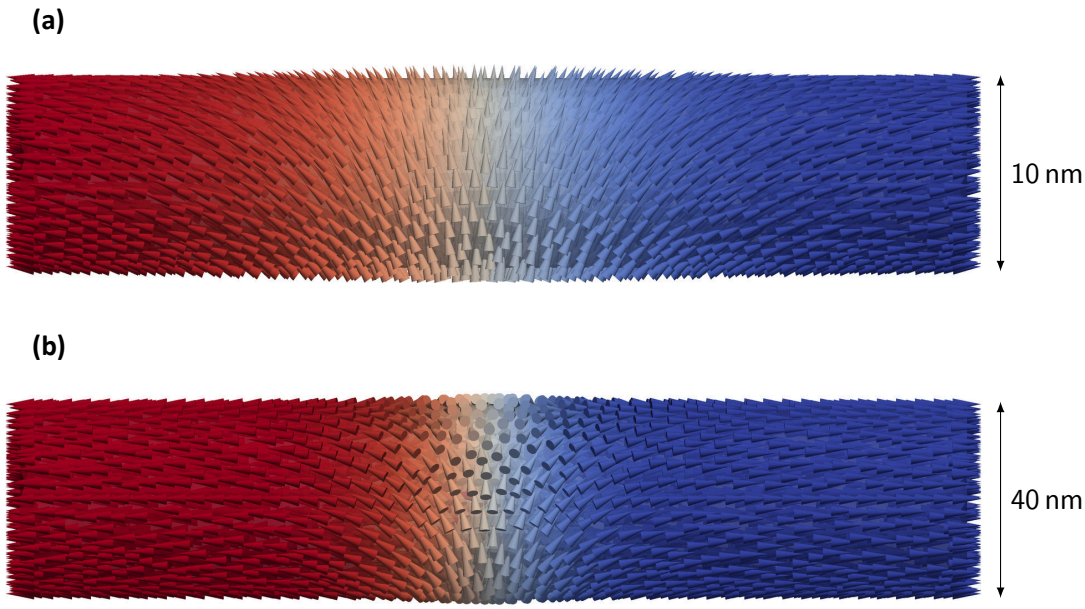

Figure 6.2: Cutout of the simulated rod, showing the domain wall for different rod diameters. The r_3-component of the magnetization is color coded. **(a)** Diameter of $d = 10$ nm. The energetically favored domain wall is of transverse type. **(b)** Diameter of $d = 40$ nm. The energetically favored domain wall is of vortex type.

for large diameters, see Fig. 6.2b and Fig. 6.3b. The critical diameter depends on the exchange length of the material. For permalloy this critical diameter is expected to be at around 20 nm.

The change of domain-wall structure is explained by the competing exchange and demagnetizaion energy. As shown in Eqn. 2.2.21 the demagnetization energy is generated by volume charges and surface charges. The surface charges are given by the normal-component of the magnetization at the boundary. Remember also that the exchange energy is basically given by the squared gradient of the magnetization, see Eqn. 2.2.10.

In a transverse wall the magnetization is homogeneous in the rotation plane, which leads to a low exchange energy of this wall type. The demagnetization energy of the transverse wall, however, is large due to the generated surface charges. In contrast, the vortex wall does not create any surface charges, but the inner curling structure leads to a high exchange energy.

A rod with a large diameter features a large surface, which leads to a high influence of the demagnetization energy. Thus the vortex wall is the favored magnetization configuration in large rods. A decrease of the diameter changes the ratio of exchange energy to demagnetization energy, which ultimately results in an exchange dominated system that favors the transverse wall over the vortex wall.

While the energy density of the demagnetization field does not depend on the spatial scaling of a magnetization configuration, the exchange-energy density increases with decresing size

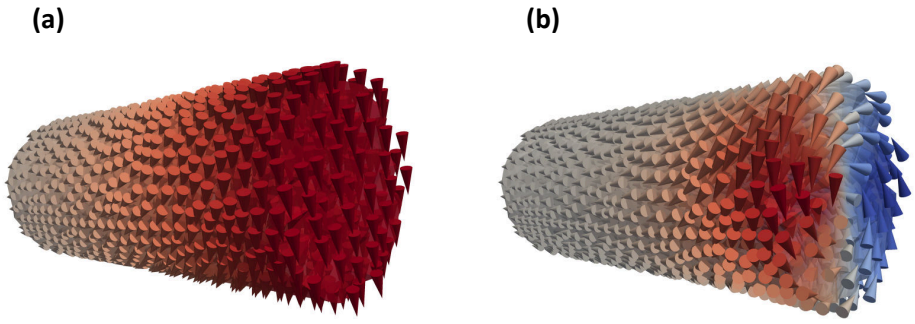

Figure 6.3: Detailed view at the structure of the domain wall within the rod. A cutout of the rod is shown, with the cut being chosen at the center of the domain wall. The r_1-component of the magnetization is color coded. **(a)** Transverse wall. **(b)** Vortex wall.

due to its dependence on the gradient of the magnetization. This effect could be successfully reproduced with the finite-element code magnum.fe. The critical diameter for the domain-wall type was found to be between 24 nm and 25 nm, which is in good agreement to theoretical results, see [100].

CHAPTER 7

Conclusion and Outlook

Different discrete algorithms for the solution of the dynamical micromagnetic equations are presented. The focus of this work is the application of the finite-element method. The micromagnetic code magnum.fe is written that implements the presented finite-element algorithms.

The computation of the demagnetization-field with Fourier-space techniques as well as with finite-element techniques is described in detail. Within the class of Fourier-space methods an alternative to the well-known convolution with the demagnetization tensor is presented. For the solution with the finite-element method a transformation technique is described that solves the open-boundary problem by a mapping of the exterior space to a finite shell. The methods are validated and compared to each other. Fourier-space methods require a regular grid, whereas finite-element methods are able to handle irregular meshes. Thus it comes as no surprise that the finite-element method outperforms the Fourier-space methods on curved geometries. On cuboid structures however, the Fourier-space methods are both fast and accurate.

An overview over methods for the integration of the Landau-Lifshitz-Gilbert equation is given. An implicit, weak formulation originally proposed by Alouges is discussed in detail and extended by an implicit demagnetization-field computation.

Finally the implementation of the finite-element methods with the recently published library FEniCS is described and the domain-wall structure of tail-to-tail walls in nanorods is investigated.

7.1 Extending magnum.fe

The finite-element code magnum.fe provides the functionality for full three-dimensional micromagnetic simulations including demagnetization-field and exchange field. In order to optimize magnum.fe with respect to performance and versatility a number of improvements are planned for the near future.

In order to distribute the computation of large systems, magnum.fe is planned to make use of the message passing interface (MPI). Most of the functionality of both FEniCS and magnum.fe is already MPI capable und thus only a small set of functions have to be modified in order to achieve this goal.

In order to support the best method for each particular problem, a number of alternative algorithms should be integrated into the code. For example the implementation of the finite-element–boundary-element coupling as introduced in Sec. 3.2.2 is planned to be integrated into magnum.fe in the near future.

There are many further improvements of magnum.fe one could think of. The code is open source and available at Github, see [99]. Github is a so-called social coding platform and supports collaboration through the version management system Git. In the recent publication [64] the code is described and the readers are encouraged to contribute to magnum.fe.

7.2 Optimal Control

Based on magnum.fe an optimal-control code is currently developed by the Master-student Jonas Holländer. The aim of this project is the retrieval of an optimal external field here called $\boldsymbol{u}(\boldsymbol{r}, t)$ for the minimization of the functional

$$\min\ J(\boldsymbol{u}, \boldsymbol{m}) \equiv \frac{1}{2}\|\boldsymbol{m} - \overline{\boldsymbol{m}}\|^2_{L^2(\Omega_T)} + \frac{\kappa}{2}\|\boldsymbol{m}(T) - \overline{\boldsymbol{m}}\|^2_{L^2(\Omega)} + \frac{\lambda}{2}\|\boldsymbol{u}\|^2_{L^2(\Omega_T)} \tag{7.2.1}$$

with the magnetization $\boldsymbol{m}$ being subject to the Landau-Lifshitz-Gilbert equation including the exchange field and an external field given by the control $\boldsymbol{u}$. Here $\Omega_T = (0, T)\times\Omega$, $\overline{\boldsymbol{m}}$ is a desired magnetization configuration and κ and λ are scalar parameters. The functional is designed such that deviations from the magnetization $\boldsymbol{m}$ to the desired magnetization $\overline{\boldsymbol{m}}$ are penalized. The first term of Eqn. 7.2.1 penalizes these deviations at every time. The second term penalizes the deviation at the end of the simulation T. The last term accounts for the costs of the control $\boldsymbol{u}$. By choice of κ and λ the relative influence of these terms on the functional can be tuned.

Jonas Holländer uses an adjoint method in order to construct a gradient descent method for minimization of the functional J.

Acknowledgement

Many people contributed to this thesis in one way or the other. Particularly I want to thank

Professor Dr. Michael Hinze for the supervision of this thesis, for patiently introducing me to numerical mathematics and for many inspiring discussions.

Privatdozent Dr. Guido Meier for ''physical'' support and for valuable advice on the publication of manuscripts.

Professor Dr. Dietmar P. F. Möller for kind advice on computer science.

Professor Dr. Ulrich Merkt for the opportunity to work within the Graduiertenkolleg 1286 and for valuable advice in many fields.

Dr. André Drews for coordination of our simulation group, for a lot of support and for sharing his knowledge on micromagnetism with me.

Theo Gerhardt for many inspriring discussions, enjoyable lunch breaks and evenings, and for proof reading the whole thesis.

Gunnar Selke for sharing his endless knownledge on any programming related questions with me.

Christoph Hübner for inspiring discussions, especially during lunch breaks.

Dr. Benjamin Krüger for knowing almost everything about micromagnetism and sharing this knowledge with me.

Professor Dr. Thomas Schrefl for being such a nice host during my six-week scientific visit to Vienna/St. Pölten, for teaching me a lot on finite-element micromagnetism, and for giving me the oppurtunity to attend interesting conferences.

Privatdozent Dr. Dieter Suess for long discussions on computational micromagnetics, especially on boundary conditions.

Lukas Exl for so much mathematical input and for a great time in Vienna and Hamburg.

Dr. Florian Bruckner for explaining the boundary-element method to me and for many critical questions.

Johann Fischbacher for teaching me the physics of skiing.

Christian Kahle for valuable advice on block preconditioning.

All members of the Graduiertenkolleg 1286 for workshops that were both inspiring and fun.

Dr. Katrin Buth for her work for the Graduiertenkolleg.

All organizers and participants of the Lothar Collatz school retreat for a great workshop.

Dr. Markus Bolte for laying the foundation of this work by supervising my diploma thesis.

The DFG for financial support via the Graduiertenkolleg 1286.

My parents and my sister for supporting me in everything I do and for making this work possible in the first place.

My friends for all the pleasant distractions from work.

My girlfriend Hanna for always supporting and encouraging me and for taking some of the weight off my shoulders in the last exhausting months.

Polli for being who she is.

Bibliography

[1] T. Schrefl, M. E. Schabes, D. Suess, and M. Stehno. Dynamic micromagnetic write head fields during magnetic recording in granular media. *IEEE Transactions on Magnetics*, 40 (4):2341–2343, 2004.

[2] M. E. Schabes. Micromagnetic simulations for terabit/in^2 head/media systems. *Journal of Magnetism and Magnetic Materials*, 320(22):2880–2884, 2008.

[3] D. Suess, T. Schrefl, S. Fahler, M. Kirschner, G. Hrkac, F. Dorfbauer, and J. Fidler. Exchange spring media for perpendicular recording. *Applied Physics Letters*, 87(1):012504–012504, 2005.

[4] S. Tehrani, J. Slaughter, E. Chen, M. Durlam, J. Shi, and M. DeHerren. Progress and outlook for MRAM technology. *IEEE Transactions on Magnetics*, 35(5):2814–2819, 1999.

[5] J. O. Oti and S. E. Russek. Micromagnetic simulations of magnetoresistive behavior of sub-micrometer spin-valve MRAM devices. *IEEE Transactions on Magnetics*, 33(5): 3298–3300, 1997.

[6] S. S. Parkin, M. Hayashi, and L. Thomas. Magnetic domain-wall racetrack memory. *Science*, 320(5873):190–194, 2008.

[7] J. Fidler, T. Schrefl, S. Hoefinger, and M. Hajduga. Recent developments in hard magnetic bulk materials. *Journal of Physics: Condensed Matter*, 16(5):S455, 2004.

[8] A. Muxworthy, D. Heslop, and W. Williams. Influence of magnetostatic interactions on first-order-reversal-curve (FORC) diagrams: A micromagnetic approach. *Geophysical Journal International*, 158(3):888–897, 2004.

[9] D.-H. Kim, E. A. Rozhkova, I. V. Ulasov, S. D. Bader, T. Rajh, M. S. Lesniak, and V. Novosad. Biofunctionalized magnetic-vortex microdiscs for targeted cancer-cell destruction. *Nature Materials*, 9(2):165–171, 2009.

[10] A. Hubert and R. Schäfer. *Magnetic Domains*. Springer, Berlin, 1998.

[11] D. J. Thouless. *Quantum Mechanics of Many-Body Systems*. Academic Press, New York, 1961.

[12] J. D. Jackson. Classical electrodynamics, 3rd ed. *American Journal of Physics*, 67(9):841, 1999.

[13] D. J. Griffiths. *Introduction to Quantum Mechanics*. Prentice Hall, New Jersey, 1994.

[14] W. Döring. Mikromagnetismus. In S. Flügge, editor, *Handbuch der Physik*, volume 18/2, pages 314–437. Springer, Berlin Heidelberg, 1966.

[15] L. D. Landau and E. M. Lifshitz. On the theory of the dispersion of magnetic permeability in ferromagnetic bodies. *Physikalische Zeitschrift der Sowjetunion*, 8:153–169, 1935.

[16] T. L. Gilbert. A Lagrangian formulation of the gyromagnetic equation of the magnetic field. *Physical Review*, 100:1243, 1955.

[17] T. L. Gilbert. A phenomenological theory of damping in ferromagnetic materials. *IEEE Transactions on Magnetics*, 40(6):3443–3449, 2004.

[18] L. D. Landau and E. M. Lifshitz. Mechanics. In *Course of Theoretical Physics*. Pergamon Press, Oxford, 1969.

[19] J.-E. Wegrowe and M.-C. Ciornei. Magnetization dynamics, gyromagnetic relation, and inertial effects. *American Journal of Physics*, 80(7):607–611, 2012.

[20] N. Bode, L. Arrachea, G. S. Lozano, T. S. Nunner, and F. von Oppen. Current-induced switching in transport through anisotropic magnetic molecules. *Physical Review B*, 85: 115440, 2012.

[21] G. Carbou and P. Fabrie. Regular solutions for Landau-Lifschitz equation in a bounded domain. *Differential and Integral Equations*, 14(2):213–229, 2001.

[22] G. Carbou and P. Fabrie. Regular solutions for Landau-Lifschitz equation in R^3. *Communications in Applied Analysis*, 5(1):17–30, 2001.

[23] F. Alouges and A. Soyeur. On global weak solutions for Landau-Lifshitz equations: existence and nonuniqueness. *Nonlinear Analysis: Theory, Methods & Applications*, 18(11): 1071–1084, 1992.

[24] G. Rado and J. Weertman. Spin-wave resonance in a ferromagnetic metal. *Journal of Physics and Chemistry of Solids*, 11(3–4):315 – 333, 1959.

[25] W. F. Brown Jr. *Micromagnetics*. Interscience Publisher, New York, 1963.

[26] M. d'Aquino, C. Serpico, and G. Miano. Geometrical integration of Landau-Lifshitz-Gilbert equation based on the mid-point rule. *Journal of Computational Physics*, 209 (2):730–753, 2005.

[27] I. Cimrák. A survey on the numerics and computations for the Landau-Lifshitz equation of micromagnetism. *Archives of Computational Methods in Engineering*, 15(3):1–37, 2007.

[28] A. Thiaville, J. M. García, J. Miltat, T. Schrefl, et al. Micromagnetic study of Bloch-point-mediated vortex core reversal. *Physical Review B*, 67(9):094410, 2003.

[29] C. Kittel and P. McEuen. *Introduction to solid state physics*, volume 7. Wiley New York, 1996.

[30] A. Lyberatos, D. Berkov, and R. Chantrell. A method for the numerical simulation of the thermal magnetization fluctuations in micromagnetics. *Journal of Physics: Condensed Matter*, 5(47):8911, 1993.

[31] D. Garanin. Fokker-Planck and Landau-Lifshitz-Bloch equations for classical ferromagnets. *Physical Review B*, 55(5):3050, 1997.

[32] S. Zhang and Z. Li. Roles of nonequilibrium conduction electrons on the magnetization dynamics of ferromagnets. *Physical Review Letters*, 93(12):127204, 2004.

[33] S. Parkin and D. Mauri. Spin engineering: Direct determination of the Ruderman-Kittel-Kasuya-Yosida far-field range function in ruthenium. *Physical Review B*, 44(13):7131, 1991.

[34] I. A. Sergienko and E. Dagotto. Role of the Dzyaloshinskii-Moriya interaction in multiferroic perovskites. *Physical Review B*, 73(9):094434, 2006.

[35] M. Heide, G. Bihlmayer, and S. Blügel. Dzyaloshinskii-Moriya interaction accounting for the orientation of magnetic domains in ultrathin films: Fe/W (110). *Physical Review B*, 78(14):140403, 2008.

[36] L. Lopez-Diaz, D. Aurelio, L. Torres, E. Martinez, M. Hernandez-Lopez, J. Gomez, O. Alejos, M. Carpentieri, G. Finocchio, and G. Consolo. Micromagnetic simulations using graphics processing units. *Journal of Physics D: Applied Physics*, 45(32):323001, 2012.

[37] A. Thiaville, S. Rohart, É. Jué, V. Cros, and A. Fert. Dynamics of Dzyaloshinskii domain walls in ultrathin magnetic films. *EPL (Europhysics Letters)*, 100(5):57002, 2012.

[38] D. Berkov, K. Ramstöcck, and A. Hubert. Solving micromagnetic problems. towards an optimal numerical method. *Physica Status Solidi (a)*, 137(1):207–225, 1993.

[39] K. Fabian, A. Kirchner, W. Williams, F. Heider, T. Leibl, and A. Huber. Three-dimensional micromagnetic calculations for magnetite using FFT. *Geophysical Journal International*, 124(1):89–104, 1996.

[40] C. Abert, G. Selke, B. Krüger, and A. Drews. A fast finite-difference method for micromagnetics using the magnetic scalar potential. *IEEE Transactions on Magnetics*, 48(3):1105 –1109, 2012.

[41] E. Kritsikis, J.-C. Toussaint, O. Fruchart, H. Szambolics, and L. Buda-Prejbeanu. Fast computation of magnetostatic fields by nonuniform fast Fourier transforms. *Applied Physics Letters*, 93(13):132508–132508, 2008.

[42] J. Blue and M. Scheinfein. Using multipoles decreases computation time for magnetostatic self-energy. *IEEE Transactions on Magnetics*, 27(6):4778 –4780, 1991.

[43] C. Seberino and H. N. Bertram. Concise, efficient three-dimensional fast multipole method for micromagnetics. *IEEE Transactions on Magnetics*, 37(3):1078–1086, 2001.

[44] B. Livshitz, A. Boag, H. N. Bertram, and V. Lomakin. Nonuniform grid algorithm for fast calculation of magnetostatic interactions in micromagnetics. *Journal of Applied Physics*, 105(7):07D541, 2009.

[45] J. Jusélius and D. Sundholm. Parallel implementation of a direct method for calculating electrostatic potentials. *The Journal of Chemical Physics*, 126(9):094101, 2007.

[46] L. Exl, W. Auzinger, S. Bance, M. Gusenbauer, F. Reichel, and T. Schrefl. Fast stray field computation on tensor grids. *Journal of Computational Physics*, 231(7):2840–2850, 2012.

[47] L. Exl, C. Abert, N. J. Mauser, T. Schrefl, H. P. Stimming, and D. Suess. FFT-based Kronecker product approximation to micromagnetic long-range interactions, 2012. arXiv:1212.3509.

[48] L. Exl and T. Schrefl. Non-uniform FFT for the finite element computation of the micromagnetic scalar potential, 2013. arXiv:1305.3162.

[49] D. Fredkin and T. Koehler. Hybrid method for computing demagnetizing fields. *IEEE Transactions on Magnetics*, 26(2):415 –417, 1990.

[50] X. Brunotte, G. Meunier, and J. Imhoff. Finite element modeling of unbounded problems using transformations: a rigorous, powerful and easy solution. *IEEE Transactions on Magnetics*, 28(2):1663 –1666, 1992.

[51] W. H. Press, S. A. Teukolsky, W. T. Vetterling, and B. P. Flannery. *Numerical recipes: the art of scientific computing*. Cambridge University Press, Cambridge, 2007.

[52] J. W. Cooley and J. W. Tukey. An algorithm for the machine calculation of complex Fourier series. *Mathematics of Computation*, 19(90):297–301, 1965.

[53] A. J. Newell, W. Williams, and D. J. Dunlop. A generalization of the demagnetizing tensor for nonuniform magnetization. *Journal of Geophysical Research*, 98(B6):9551–9555, 1992.

[54] K. M. Lebecki, M. J. Donahue, and M. W. Gutowski. Periodic boundary conditions for demagnetization interactions in micromagnetic simulations. *Journal of Physics D: Applied Physics*, 41(17):175005, 2008.

[55] B. Krüger, G. Selke, A. Drews, and D. Pfannkuche. Fast and accurate calculation of the demagnetization tensor for systems with periodic boundary conditions. 2013.

[56] D. Braess. *Finite elements*. Cambridge University Press, 2007.

[57] P. G. Ciarlet. *The finite element method for elliptic problems*. Access Online via Elsevier, 1978.

[58] O. C. Zienkiewicz and R. L. Taylor. *The finite element method*, volume 3. McGraw-hill London, 1977.

[59] Y. Saad. *Iterative methods for sparse linear systems*. Society for Industrial and Applied Mathematics, 2003.

[60] C. Garcia-Cervera and A. Roma. Adaptive mesh refinement for micromagnetics simulations. *IEEE Transactions on Magnetics*, 42(6):1648–1654, 2006.

[61] N. Popovićć and D. Praetorius. Applications of $\mathcal{H}$-matrix techniques in micromagnetics. *Computing*, 74:177–204, 2005.

[62] J. Imhoff, G. Meunier, X. Brunotte, and J. Sabonnadiere. An original solution for unbounded electromagnetic 2D-and 3D-problems throughout the finite element method. *IEEE Transactions on Magnetics*, 26(5):1659–1661, 1990.

[63] F. Henrotte, B. Meys, H. Hedia, P. Dular, and W. Legros. Finite element modelling with transformation techniques. *IEEE Transactions on Magnetics*, 35(3):1434–1437, 1999.

[64] C. Abert, L. Exl, F. Bruckner, A. Drews, and D. Suess. magnum. fe: A micromagnetic finite-element simulation code based on FEniCS. *Journal of Magnetism and Magnetic Materials*, 345(0):29–35, 2013.

[65] A. Prohl. *Computational Micromagnetism*. Teubner BG GmbH, 2001.

[66] M. Kruzik and A. Prohl. Recent developments in the modeling, analysis, and numerics of ferromagnetism. *SIAM Review*, 48(3):439–483, 2006.

[67] C. Abert, L. Exl, G. Selke, A. Drews, and T. Schrefl. Numerical methods for the stray-field calculation: A comparison of recently developed algorithms. *Journal of Magnetism and Magnetic Materials*, 326(0):176–185, 2012.

[68] F. Alouges. A new finite element scheme for Landau-Lifchitz equations. *Discrete and Continuous Dynamical Systems - Series S*, 1(2):187–196, 2008.

[69] J. C. Butcher. *The numerical analysis of ordinary differential equations: Runge-Kutta and general linear methods*. Wiley-Interscience, 1987.

[70] E. Fehlberg. Classical fifth-, sixth-, seventh-, and eighth-order Runge-Kutta formulas with stepsize control. *NASA Technical Report*, 287, 1968.

[71] J. R. Cash and A. H. Karp. A variable order Runge-Kutta method for initial value problems with rapidly varying right-hand sides. *ACM Transactions on Mathematical Software (TOMS)*, 16(3):201–222, 1990.

[72] J. E. Miltat and M. J. Donahue. Numerical micromagnetics: finite difference methods. *Handbook of Magnetism and Advanced Magnetic Materials*, 2007.

[73] D. Suess, V. Tsiantos, T. Schrefl, J. Fidler, W. Scholz, H. Forster, R. Dittrich, and J. Miles. Time resolved micromagnetics using a preconditioned time integration method. *Journal of Magnetism and Magnetic Materials*, 248(2):298–311, 2002.

[74] G. W. E. Hairer. *Solving ordinary differential equations II*. Springer, 2010.

[75] Y. Nakatani, Y. Uesaka, and N. Hayashi. Direct solution of the Landau-Lifshiftz-Gilbert equation for micromagnetics. *Japanese Journal of Applied Physics*, 28(12):2485–2507, 1989.

[76] S. Bartels and A. Prohl. Convergence of an implicit finite element method for the Landau-Lifshitz-Gilbert equation. *SIAM Journal on Numerical Analysis*, 44(4):1405–1419, 2006.

[77] F. Alouges and P. Jaisson. Convergence of a finite element discretization for the Landau-Lifshitz equations in micromagnetism. *Mathematical Models and Methods in Applied Sciences*, 16(02):299–316, 2006.

[78] P. Goldenits, G. Hrkac, D. Praetorius, and D. Suess. An effective integrator for the Landau-Lifshitz-Gilbert equation. In *Proceedings of Mathmod 2012 Conference*, 2012.

[79] F. Alouges, E. Kritsikis, and J.-C. Toussaint. A convergent finite element approximation for Landau-Lifschitz-Gilbert equation. *Physica B: Condensed Matter*, 407(9):1345–1349, 2012.

[80] H. A. Van der Vorst. Bi-CGSTAB: A fast and smoothly converging variant of Bi-CG for the solution of nonsymmetric linear systems. *SIAM Journal on Scientific and Statistical Computing*, 13(2):631–644, 1992.

[81] µMAG standard problem #4. URL `http://www.ctcms.nist.gov/~rdm/std4/spec4.html`.

[82] Micromagnum. URL `http://micromagnum.informatik.uni-hamburg.de/`.

[83] M. Donahue and D. Porter. OOMMF user's guide, version 1.0. *Interagency Report*, NISTIR 6376, 1999.

[84] A. Vansteenkiste and B. Van De Wiele. MuMax: a new high-performance micromagnetic simulation tool. *Journal of Magnetism and Magnetic Materials*, 323(21):2585–2591, 2011.

[85] M. Najafi, B. Krüger, S. Bohlens, G. Selke, B. Güde, M. Bolte, and D. Möller. The micromagnetic modeling and simulation kit M^3S for the simulation of the dynamic response of ferromagnets to electric currents. *Grand Challenges in Modeling & Simulation (GCMS'08)*, 2008.

[86] Nmag finite difference. `http://cmg.soton.ac.uk/research/projects/nmag-finite-difference/`.

[87] Yamms. `https://github.com/c-abird/yamms_core`.

[88] C. Abert. Cell-size independent micromagnetic simulations including thermal effects, Diploma Thesis, Universität Hamburg, 2010.

[89] W. Scholz, J. Fidler, T. Schrefl, D. Suess, R. Dittrich, H. Forster, and V. Tsiantos. Scalable parallel micromagnetic solvers for magnetic nanostructures. *Computational Materials Science*, 28(2):366 – 383, 2003.

[90] T. Fischbacher, M. Franchin, G. Bordignon, and H. Fangohr. A systematic approach to multiphysics extensions of finite-element-based micromagnetic simulations: Nmag. *IEEE Transactions on Magnetics*, 2007.

[91] Femme. `http://suessco.com/simulations/`.

[92] A. Kakay, E. Westphal, and R. Hertel. Speedup of FEM micromagnetic simulations with graphical processing units. *IEEE Transactions on Magnetics*, 46(6):2303–2306, 2010.

[93] A. Logg, K.-A. Mardal, G. N. Wells, et al. *Automated Solution of Differential Equations by the Finite Element Method*. Springer, 2012. ISBN 978-3-642-23098-1.

[94] C. Geuzaine and J. Remacle. Gmsh: A 3-D finite element mesh generator with built-in pre-and post-processing facilities. *International Journal for Numerical Methods in Engineering*, 79(11):1309–1331, 2009.

[95] R. C. Kirby and A. Logg. A compiler for variational forms. ACM Trans. Math. Software 32(3), 2006, pp. 417-444, 2011.

[96] M. S. Alnæs. *Automated Solution of Differential Equations by the Finite Element Method*, chapter 17. Springer, 2012. ISBN 978-3-642-23098-1.

[97] M. S. Alnaes, A. Logg, K.-A. Mardal, and O. Skavhaug. Unified framework for finite element assembly. *International Journal of Computational Science and Engineering*, 4(4): 231–244, 2009.

[98] SWIG. `http://www.swig.org/`.

[99] magnum.fe. `http://github.com/c-abird/magnum.fe/`.

[100] R. Wieser, U. Nowak, and K.-D. Usadel. Domain wall mobility in nanowires: Transverse versus vortex walls. *Physical Review B*, 69(6):064401, 2004.